



Universidad de Granada

**Nacre ultrastructure:
amorphous precursors, aggregation
and crystallization**

Elena Macías Sánchez

PhD Thesis

Department of Stratigraphy and Palaeontology

University of Granada



Editor: Universidad de Granada. Tesis Doctorales
Autora: Elena Macías Sánchez
ISBN: 978-84-9163-693-9
URI: <http://hdl.handle.net/10481/48910>

The doctoral candidate **Elena Macías Sánchez**
and the thesis supervisor, **Prof. Antonio G. Checa**

Guarantee, by signing this doctoral thesis, that the work has been done by the doctoral candidate under the direction of the thesis supervisor and, as far as we know, during the development of the research, the rights of the authors to be cited (when their results or publications have been used) have been respected.

Granada, May 2017

Thesis supervisor:
Prof. Antonio G. Checa

Doctoral candidate:
Elena Macías Sánchez

To my mother and my grandfather,
who always encouraged me to do what I loved.

We are what we repeatedly do.
Excellence, then, is not an act, but a habit.

Aristoteles

Contents

Extended Abstract	1
Resumen extendido	5
I Introduction	
1 Introduction	
1.1 Motivation	11
1.2 Objectives	13
2 Biomineralization	
2.1 Introduction	15
2.2 Nucleation and crystal growth	17
2.3 Amorphous phases in biomineralization	18
2.4 Nanogranularity	21
2.5 Transformation mechanisms	22
2.5.1 Solid-state phase transformation	22
2.5.2 Dissolution - reprecipitation mechanism	24
2.5.3 Further discussion about transformation mechanisms	25

3	Role of vesicles in biomineralization	
3.1	Introduction	27
3.2	Ion uptake	29
3.3	Stabilization of the amorphous phase	30
3.4	Deposition of the mineral phase	33
3.5	The gastropod vesicle transport system	34
4	Nacre	
4.1	Introduction	35
4.2	Secretion	36
4.3	Crystallography	38
4.4	Mineral bridges	39

II Materials and methods

5	Materials and methods	
5.1	Material	43
5.2	Treatments	44
5.3	Electron Back Scattered Diffraction (EBSD)	45
5.4	Atomic Force Microscopy (AFM)	46
5.5	Transmission Electron Microscopy (TEM)	49
5.5.1	The transmission electron microscope	50
5.5.2	Sample preparation	55
5.5.2.1	Fixation and embedding	56
i.	Chemical fixation	57
ii.	Freeze drying	57
5.5.2.2	Sectioning	58

5.5.3	High resolution transmission electron microscopy	61
5.5.3.1	Fast Fourier Transform (FFT) analysis	61
5.5.3.2	Indexing	63
5.6	Electron Energy Loss Spectroscopy (EELS)	64
5.7	Energy Dispersive X-ray Spectroscopy (EDS)	68

III Results

6 Results

6.1	Amorphous calcium carbonate in nacre	71
6.1.1	Ultrastructure	71
6.1.2	ACC and crystalline nanodomains	74
6.1.3	Indexing of crystalline nanodomains	76
6.1.4	Nanogranularity	78
6.1.5	Tomography	80
6.1.6	Elemental analysis	81
6.2	Elongation and alignment of nanogranules and their relation with the crystallography	85
6.3	Vesicles and surface membrane in nacreous gastropods	87
6.3.1	Ultrastructure	88
6.3.2	Elemental analysis	90

IV Discussion

7 Discussion

7.1	Amorphous calcium carbonate in nacre	95
7.2	Elongation and alignment of nanogranules	98
7.3	Vesicles and surface membrane in nacreous gastropods	99

V Conclusions	101
Conclusiones	103
References	107
List of abbreviations	119
List of related publications	121
Acknowledgements	123

Appendixes: publications

- Transformation of ACC into aragonite in nacre
 Macías-Sánchez *et al.* 2017. *Scientific Reports*
 DOI 10.1038/s41598-017-12673-0
- Crystallographic control on the substructure of nacre tablets
 Checa *et al.* 2013 *Journal of Structural Biology*
 DOI 10.1016/j.jsb.2013.07.014
- The transport system of nacre components through the surface membrane
 of gastropods
 Macías-Sánchez *et al.* 2015 *Key Engineering Materials*
 DOI 10.4028/www.scientific.net/KEM.672.103

Extended abstract

Biomaterials are organomineral composites synthesized by organisms. A composite is defined as the material that results from the combination of two or more different and structurally complementary materials. A composite has certain structural or functional properties, which are not present in the individual components. These emergent properties appear from the interaction of their individual constituents, which normally involves an organic matrix and a reinforcing material, organized in a hierarchical manner. Vertebrate bone, echinoderm spines and molluscs shells are some examples of composite biomaterials. The field of biomineralization aims to understand the formation, structure and properties of the minerals deposited by biological systems.

Molluscs are excellent biocomposite constructors. Making use of a reduced number of elements (shells are mainly composed of calcium carbonate, in the form of calcite or aragonite, and 1–5.5% of organic material) they can produce more than a dozen microstructures. The

crystallites and the organic matter organize into particular patterns termed microstructures, characterized by recurrent spatial and crystallographic relationships. Frequently, shells are composed by layers with different microstructures, and even different mineralogies. For this to occur, organisms exert an exquisite multi-level control over the transport, aggregation and deposition of the mineral.

The formation processes of the different microstructures are of great interest, in part due to their applicability in the development of biomimetic materials. One of the hot topics today is the formation of crystalline materials through amorphous phases. Its discovery attracted great scientific interest, since the classical mineralization models developed in the last century described the crystal growth through the addition of ions, but not by aggregation of higher-order particles.

The present PhD work addresses the issue of the amorphous precursors in one of the best studied mollusc microstructures, the nacre. The presence of amorphous calcium carbonate (ACC) in the forming tablets has been recently demonstrated. Our approach was to make a high resolution study encompassing two main lines of evidence: imaging and elemental analysis. We have studied three stages of the nacre formation process using a gastropod species as model system. The peculiarity of gastropods is that they present a dense organic membrane (the surface membrane) which covers the mineralization compartment. Within such compartment, the organic membranes (interlamellar membranes) are arranged first and the mineral forms between them. The gastropod nacre tablets stack forming towers.

This PhD study is divided in three sections:

- Determination of the transport mechanism of the ACC (vesicles function and surface membrane dynamics).
- Characterization of the ACC in the forming tablets (distribution and relationships with the crystalline phase).
- Study of the morphology in the mature tablet (nanogranularity).

For the first section we have used transmission electron microscopy (TEM) and electron energy loss spectroscopy (EELS). We have imaged and analysed the vesicles segregated by the mantle cells and the surface membrane. The results show that some of these vesicles transport calcium-rich material attached to their inner surface; the membranes of these vesicles also contain calcium. The surface membrane and the interlamellar membranes show high amount of calcium. The surface membrane undergoes a structure modification process, from a fuzzy aspect looking towards the mantle cells, to a defined porous structure at the mineralization compartment side. When the interlamellar membranes detach from the surface membrane the porous structure is evident.

For the second section, about the transformation and crystallization of ACC, the amorphous phase has been imaged by means of TEM/STEM. The forming tablets are composed by an aggregation of globular particles (20–50 nm) that present a crystalline core (~ 30 nm average size) embedded in amorphous matrix (5–10 nm thickness). This amorphous layer presents a mixture of organic material and ACC, both identified by EELS. The crystalline nanodomains present complex, pseudodendritic forms, which might be connected in the third dimension.

The third section of this PhD study is dedicated to the study of the lineations in the surface of the nacre tablets. It was carried out by scanning electron microscopy (SEM), electron backscattered diffraction (EBSD) and atomic force microscopy (AFM). Images clearly show that lineations are the result of the aggregation of calcium carbonate nanoglobules. EBSD maps show that the lineations are aligned with the a -axis of the tablets. Our model proposes that this morphology results from the differential absorption of macromolecules along the aragonite crystallographic axes.

Finally, it is interesting to note that the results of the two latter sections match well, reinforcing our hypothesis that the nanogranular pattern characteristic of biominerals might not represent the aggregation unit sizes as was implied by some authors, but are the result of the subsequent crystallization process.

Resumen extendido

Los biominerales son materiales compuestos sintetizados por organismos. Un material compuesto se define como el resultante de la combinación de dos o más materiales distintos y estructuralmente complementarios. El material compuesto presenta ciertas propiedades estructurales o funcionales que no se encuentran en los componentes individuales, sino que resultan de su interacción. Estos componentes normalmente involucran una matriz orgánica y un material de refuerzo, organizados de una forma jerárquica. El hueso de vertebrados, las espinas de equinodermos y las conchas de moluscos son ejemplos de biomateriales compuestos. Los estudios de biomineralización tienen como objetivo entender la formación, estructura y propiedades de los minerales depositados por sistemas biológicos.

Los moluscos son excelentes productores de biominerales. Haciendo uso de un reducido número de elementos (las conchas están compuestas principalmente de carbonato cálcico, en forma de calcita o aragonito, y un 1-5.5 % de materia orgánica), pueden producir más de una docena de

microestructuras. Los cristales y la matriz orgánica se organizan en microestructuras, que se caracterizan por presentar relaciones espaciales y cristalográficas recurrentes. Frecuentemente las conchas están compuestas por capas con diferentes microestructuras, e incluso diferentes mineralogías. Para que esto ocurra, los organismos ejercen un exquisito control a varios niveles para regular el transporte, la agregación y la deposición del mineral.

Los procesos de formación de las diferentes microestructuras son de gran interés, en parte debido a su aplicabilidad en el desarrollo de materiales biomiméticos. Uno de los temas candentes a día de hoy es la formación de materiales cristalinos a través de fases amorfas. Su descubrimiento atrajo gran interés científico, ya que los modelos clásicos de crecimiento cristalino desarrollados en el último siglo se basaban en mecanismos de adición de iones, pero no contemplaban el crecimiento mediante la adición de partículas de mayor tamaño.

El presente trabajo aborda el tema de los precursores amorfos en una de las microestructuras de moluscos mejor estudiadas, el nácar. La presencia de carbonato cálcico amorfo (ACC, por sus siglas en inglés) en las tabletas de nácar en formación ha sido demostrada recientemente. Nuestra aproximación ha sido hacer un estudio de alta resolución aunando dos técnicas principales: imagen y análisis elemental. Hemos estudiado tres fases del proceso de formación del nácar usando como sistema modelo una especie de gasterópodo. Los gasterópodos tienen la peculiaridad de presentar una membrana densa (la membrana superficial) que cubre el compartimento de mineralización. Las membranas orgánicas (membranas interlamelares) se disponen en este compartimento y entre ellas crecen las

placas minerales. Las placas de nácar de gasterópodos se apilan formando torres.

Los tres bloques en los que se divide esta tesis doctoral se enumeran a continuación:

- Determinación del mecanismo de transporte del ACC (función de las vesículas y dinámica de la membrana superficial).
- Caracterización del ACC en las tabletas en formación (distribución y relación con la fase cristalina).
- Estudio de la morfología resultante en las tabletas maduras (nanogranularidad).

Para el primer bloque hemos usado microscopía electrónica de transmisión (TEM) y espectroscopía de pérdida de energía de electrones (EELS). Hemos visualizado y analizado las vesículas que segregan las células del manto y la membrana superficial. Los resultados muestran que algunas de estas vesículas transportan material rico en calcio unido a la superficie interna de la vesícula; también hemos encontrado calcio en la doble membrana de las vesículas. La membrana superficial y las membranas interlamelares muestran una buena cantidad de calcio. La membrana superficial sufre un proceso de cambio en su estructura y pasa de un aspecto denso y poco estructurado en el lado del manto, a una estructura porosa bien definida en el lado del compartimento de mineralización. Cuando las membranas interlamelares se separan de la membrana superficial, dicha estructura porosa es evidente.

Para el segundo bloque, sobre el estudio de la transformación y cristalización del ACC, se han tomado imágenes mediante TEM/STEM. Las

tabletas en formación están compuestas por la agregación de partículas globulares (20–50 nm) que presentan un núcleo cristalino (30 nm de tamaño medio) embebido en una matriz amorfa (5–10 nm de espesor). Esta capa amorfa está compuesta de una mezcla de material orgánico y ACC, ambos identificados mediante EELS. Los nanodominios cristalinos presentan formas complejas, pseudo-dendríticas, que podrían conectar en la tercera dimensión.

El tercer bloque de esta tesis lo compone el estudio de las lineaciones en la superficie de las tabletas de nácar. Se ha llevado a cabo mediante microscopía electrónica de barrido, difracción de electrones retrodispersados (EBSD) y microscopía de fuerza atómica (AFM). Las imágenes demuestran claramente que las lineaciones son el resultado de la agregación de nanoglóbulos de carbonato cálcico. Los mapas de EBSD muestran que las lineaciones están orientadas según el eje *a* de las tabletas. Nuestro modelo propone que esta morfología resulta de la absorción diferencial de macromoléculas a lo largo de los ejes cristalográficos del aragonito.

Finalmente, cabe decir que los resultados de las dos últimas secciones encajan bien, reforzando nuestra hipótesis de que el patrón nanogranular característico de los biominerales puede no representar los tamaños de las unidades de agregación como han sugerido ciertos autores, sino que, más bien, es resultado del proceso de cristalización posterior.

Chapter 1

Introduction

1.1 Motivation

It was assumed for a long time that organisms produce mineralized tissues directly from supersaturated solutions by ion-to-ion addition. However in the last decades, several amorphous transient phases have been discovered in biomineralization systems based on completely different mineralogies, such as the chiton teeth (ferrihydrite, an amorphous hydrated iron hydroxide phase) (Towe and Lowenstam, 1967), the sea urchin larval spicule (amorphous calcium carbonate) (Beniash *et al.* 1999) and bone (amorphous calcium phosphate) (Mahamid *et al.* 2010). Currently, the formation of biominerals through amorphous precursors is considered a widespread strategy.

This is a fascinating area of enormous interest and applicability in material sciences and biomedicine. The production of mineralized tissues is often limited by the rigidity and toughness imposed by their crystallographic structure. The synthesis through an amorphous phase, a space-filling material (Yang *et al.* 2011) that may be shaped more easily by the space in which it forms, opens a great range of technological applications.

Particularly, amorphous calcium phosphate (ACP) has proven to have *in vivo* properties, such as osteoconductivity, biodegradability and bioactivity, which make it an ideal material for dentistry, orthopaedics and medicine (Zhao *et al.* 2012). Amorphous calcium carbonate (ACC) nanoparticles are used as novel nanomaterials for the conservation of the cultural heritage such as buildings, murals and sculptures (Rodríguez-Navarro *et al.* 2016).

Nacre is a typical aragonitic microstructure found in molluscs. It is one of the most studied due to its great resistance to fracture and toughness, higher than bone. Its osteocompatibility and adhesion have also been revealed (Camprasse *et al.* 1990, Atlan *et al.* 1997). However, the knowledge about nacre formation through ACC is scarce. The presence of two amorphous phases (hydrated and anhydrous) has been demonstrated by DeVol *et al.* (2015), who mapped their distribution in growing nacre tablets. Nevertheless, a basic understanding about its aggregation and transformation mechanisms is still lacking.

The objective of this PhD study is to gain insight into the transport, aggregation and crystallization processes of amorphous calcium carbonate in nacre.

1.2 Objectives

The aim of the present PhD study is to elucidate the involvement of a transient mineral phase in the formation of nacre. We have focused on three main stages of the process: the transport to the mineralization compartment, the transformation and crystallization into aragonite inside the forming tablet and the formation and distribution of the characteristic morphological features of the crystalline biomineral (i.e. nanogranularity).

The mayor objectives are formulated as follows:

- Localization of calcium in the vesicle layer that the mantle cells produce, and which fuses with the surface membrane that covers the mineralization compartment in gastropods.
- Identification of the amorphous phase and its distribution in the forming tablets.
- Determination of the crystallographic relationships of the crystalline nanodomains embedded in the amorphous matrix.
- Characterization of the lineations present in the surface of the nacre tablets and their relation with the crystallography.

The experimental character of the research, the nanometre resolution needed to solve the questions, and the delicate conditions required to maintain the stability of the amorphous phase, implied a great effort in designing and executing the analytical approach. A great variety of sample preparation, electron microscopy and spectroscopy techniques have been applied. Their learning and adequate performance have become a main additional objective.

Chapter 2

Biom mineralization

2.1 Introduction

Biom mineralization is the process by which organisms synthesize mineralised structures. These structures provide organisms with structural support and defence, and are involved in functions such as motion, feeding and sensing. It is a widespread phenomenon found in a multitude of phyla of the six kingdoms (following Cavalier-Smith 2004 classification).

The first appearances of mineralized skeletal parts in animals correspond to siliceous and calcareous spicules attributed to sponges (*c.* 750 Ma) (Kouchinsky 2000). A great diversification of the mineral skeletons took place during the Early Cambrian radiation, probably driven by an antipredatory selective advantage (Bengtson 1994). An 80% of the modern skeletal designs (spicules, sclerites, exoskeletons, bivalved shells, internal

skeletons, mineral-impregnated cuticles, etc.) were already present in the middle Cambrian (Thomas *et al.* 2000). Although some mineralogies could be lacking (strontium sulphate, i.e. Acantharia), the diversity of minerals employed in the early skeletal evolution is basically the same as today (Knoll 2003).

The chemical compounds and the types of minerals involved in biomineralization range from silicon dioxide (e.g. sponges spicules, diatoms), calcium carbonate in the form of calcite (echinoderms spicules and mollusc shells), aragonite (mollusc nacre) and vaterite (plant cystoliths); calcium phosphate in the form of the mineral hydroxyapatite (vertebrate bone, tooth enamel), and iron oxides (chiton teeth, limpet radula, magnetotactic bacteria).

The physicochemical factors that drive inorganic mineralization, such as solubility product, supersaturation, nucleation and crystal growth, are finely controlled by organisms producing a set of crystallochemical properties that differentiate the biominerals from their inorganic counterparts. Biominerals characterize by having complex morphologies, singular textures and preferential crystallographic orientations and by forming hierarchical structures via high order assembly (Mann 2001).

The presence of an organic matrix, the segregation of soluble additives, such as ions, organic molecules, macromolecules and polymers and the confinement of the forming structures are some of the mechanisms used to control this features.

2.2 Nucleation and crystal growth

The classical nucleation theory (Volmer and Weber 1925) establishes that crystals nucleate from metastable clusters of a critical size and grow by the addition of monomers (atoms, ions or molecules, depending on the crystal) in a supersaturated solution. Supersaturation is essential for the crystallization to occur and can follow two ways: (i) through the formation of a new nucleus (primary nucleation) or (ii) through the growth of pre-existent crystals (secondary nucleation). At the same time, primary nucleation can occur spontaneously in the absence of any foreign particles (homogeneous nucleation) or can take place over the surface of foreign particles (heterogeneous nucleation).

Although the classical nucleation theory has been developed with great success over the past century, there are certain phenomena that cannot be explained by classical models, among which are the habits and microstructures of biominerals (Lowenstam and Weiner 1989). In the recent years, a set of particle-accretion processes have been identified and proposed as the basis of non-classical crystallization pathways (Cölfen and Antonietti 2005). Crystallization can occur by attachment of species more complex than simple ions: ion complexes (Habraken *et al.* 2013), ionic polymers (Demichelis *et al.* 2011) and nanoparticles, both crystalline (Li *et al.* 2012) and amorphous (Beniash *et al.* 2009). The latter (the accretion of amorphous nanoparticles) is currently considered a widespread mechanism in biomineralization.

Particle aggregation mechanisms might produce what has been called a mesocrystalline structure (Cölfen and Mann 2003). A mesocrystal diffracts as a single crystal, but its lattice is not continuous but composed of a myriad of

nanocrystallites, which are highly co-oriented but separated spatially. These nanocrystallites are connected by crystalline bridges which enable the transmission of the crystallographic orientation and confer a highly porous character to the structure (Cölfen and Mann 2003).

This structure has been defined in synthetic crystals such as TiO_2 (Penn and Banfield 1999), FeOOH (Banfield *et al.* 2000) and others (Cölfen and Antonietti 2005). Nevertheless the application of this definition to the biominerals has been controversial. It is the sequence of events (aggregation and transformation) what seems to determine whether the biominerals can be defined as mesocrystals (Bergström *et al.* 2015) or not (Kim *et al.* 2014). Whether amorphous nanoparticles crystallize first and then aggregate by oriented attachment or whether the amorphous precursors aggregate and crystallization propagates subsequently, is an open debate nowadays.

2.3 Amorphous phases in biomineralization

The first studies about the capacity of the organisms to synthesize amorphous minerals date from the nineteenth-early twentieth century (silica, Ehrenberg 1834; amorphous calcium carbonate, Minchin 1909). However their use as transient phases for biomineralization was not described until the second half of the twentieth century. Lowenstam (1962) showed that the mature teeth of chitons (Polyplacophora) were composed by magnetite ($\text{Fe}_2\text{O}_3 \cdot \text{FeO}$). In a later study, Towe and Lowenstam (1967) demonstrated that in the immature teeth the mineral was deposited as ferrihydrite (an amorphous hydrated iron hydroxide phase), which later suffered a phase transformation to magnetite, acquiring the characteristic reddish colour.

Several attempts to detect amorphous phases in bone were carried out during the eighties without success (Glimcher 1984, Grynepas *et al.* 1984). It was not until 1997 that an amorphous transient precursor in biogenic calcium carbonate was identified. The infrared spectra of the sea urchin larval spicules indicated the presence of a mixture of amorphous CaCO_3 and calcite (Beniash *et al.* 1997), consistent with X-ray diffraction patterns of lower intensity than those of geologic calcite (Berman *et al.* 1993). In a subsequent study, electron-dense amorphous granules were detected inside the spiculogenic cells. After beam irradiation the granules crystallized, and the reflections were indexed as calcite (Beniash *et al.* 1999). Successive studies on sea urchin larval spicules revealed the transformation of two disordered phases (an unstable hydrated ACC and a more stable anhydrous form) to crystalline calcite (Politi *et al.* 2008). The mechanism is not restricted to embryonic stages, but the growth through disordered phases was also demonstrated for adult spines (Politi *et al.* 2004).

The first evidence of the presence of ACC in molluscs was found in *Biomphalaria glabrata* (Gastropoda) eggs and embryos (Hasse *et al.* 2000, Marxen *et al.* 2003). The initial mineral phase was identified as ACC with an aragonite short-range order. No other CaCO_3 phases were detected (Hasse *et al.* 2000). Until 72 h the eggs were completely ACC, and the first X-ray reflections appeared at 120 h (Marxen *et al.* 2003). Weiss *et al.* (2002) detected, by Raman, a poorly crystalline phase in addition to aragonite in larval shells of *Mercenaria mercenaria* (Bivalvia). The change in the ratio of the two phases was measured over the 13 days of development, thus implying a transformation into aragonite.

The first indication of ACC in adult shells was provided by Nassif *et al.* (2005) who highlighted the presence of an amorphous layer 3-5 nm thick around mature nacre tablets; after recrystallization under the electron beam the reflections were indexed as aragonite. Subsequently, crystalline nanodomains immersed in amorphous material were imaged (Zhang and Xu 2013), but without a conclusive confirmation of the nature of the amorphous matrix. The unequivocal identification of ACC in adult nacreous shells was carried out by DeVol *et al.* (2015) in *Haliotis rufescens* (Gastropoda) by means of photoemission electron spectromicroscopy (PEEM). These authors showed the distribution of ACC in young tablets mainly at the growth front, but also inside the tablets close to the interlamellar membranes. Only reduced amounts of hydrated ACC were detected in this study, probably due to its fast transformation to anhydrous ACC, which was monitored in experiments under radiation.

The presence of stable ACC is well documented in Crustacea (Chave 1954) but it was not until recently that its transformation to calcite was demonstrated (Dillaman *et al.* 2005). In other groups such as corals (Cnidaria) the presence of high amounts of magnesium in the calcification centres (Meibom *et al.* 2004) and the morphology of the crystals obtained by crystallization experiments in the presence of soluble organic matrix extractions (Goffredo *et al.* 2011) have been taken as indicators of the presence of ACC, but clear evidence is still lacking.

In vertebrates, the first disordered precursor identified was octacalcium phosphate (OCP) in the calvaria mouse bone (Crane *et al.* 2006). Amorphous calcium phosphate (ACP) was identified in the fin-ray bones of the zebrafish (Mahamid *et al.* 2008). ACP nanospheres were deposited within the collagen

matrix and then transformed to carbonated hydroxyapatite, the mineral phase of mature bone (Mahamid *et al.* 2010).

Therefore the crystallization from a transient disordered phase rather than ion-by-ion addition has been demonstrated to be a widespread strategy in biogenic systems, which might present advantages in terms of packing, transport efficiency and mineral deposition (Mahamid *et al.* 2011).

2.4 Nanogranularity

Mutvei (1972) described with SEM that the nacre of *Nautilus* (Cephalopoda) is composed of 50–100 nm wide aragonite granules. This texture was again highlighted by means of atomic force microscopy (AFM) by Dauphin (2001). Subsequent studies revealed that it was not only present in nacre (Rousseau *et al.* 2005, Li *et al.* 2006, Checa *et al.* 2013), but in all molluscan microstructures (Dauphin 2008), corals (Cuif and Dauphin 2005), vertebrates (Tai *et al.* 2006, Dauphin and Dufour 2008) and other taxonomic groups (reviewed by Wolf *et al.* 2016). This nanogranular texture is currently considered an intrinsic characteristic of biominerals.

AFM phase images evidenced that the nanogranular structure is composed of two materials with different mechanical properties: a stiffer material identified as the mineral granules and a softer, more adhesive material in the form of pellicles (5–10 nm thick) that surround the granules. The latter was identified as organic (Dauphin 2001, Rousseau *et al.* 2005) or as a mixture of ACC and organic macromolecules (Seto *et al.* 2012).

This nanogranular texture has been hypothesized to be the result of an ACC accretion particle mechanism (Seto *et al.* 2012, Gal *et al.* 2014). Based on the morphology, some authors argue that the aggregation units have a similar size to the nanoglobules observed in the crystalline structure (Gal *et al.* 2014), although with no conclusive evidence. The organic material would be expelled from the crystal as crystallization takes place and would remain in the form of pellicles surrounding the crystals (Seto *et al.* 2012).

In vitro experiments showed that the nanogranular morphology typical of biominerals (Dauphin 2008) appears only in the presence of organic molecules, likely by the accumulation of such molecules around the nanoparticles. In absence of these molecules, calcite faces grow flat (Rodríguez-Navarro *et al.* 2016).

2.5 Transformation mechanisms

The disordered phases are transported to the mineralization compartments where they undertake transformation to crystalline material. Two main mechanisms have been proposed to explain the transformation from the disordered to the crystalline phase: solid state transformation via secondary nucleation (Politi *et al.* 2008, Killian *et al.* 2009) and dissolution–reprecipitation (Aizenberg *et al.* 2003, Xu *et al.* 2006).

2.5.1 Solid-state phase transformation

A phase transformation occurs when a material changes its composition or structure. If the composition is the same but differs in the structure, local atomic movements can induce the change. Phase transitions in solids can

occur because atoms are not locked in place, but can move, although at infinitively slower rate than gases and liquids (Carter and Norton 2007).

A solid-state epitaxial secondary crystallization mechanism (also referred in the literature as secondary nucleation) has been proposed to explain the crystalline growth based on the aggregation of amorphous nanoparticles. It is defined as a crystal growth process operating through the addition of clusters (or ions) to pre-existent crystals, driven by a reduction of the Gibbs free energy (Burton *et al.* 1951).

In the sea urchin larval spicule, the ACC particles are added to the syncytium compartment under dehydrated conditions (Beniash *et al.* 1999) and transform onto the initial rhombohedral calcite crystal (Beniash *et al.* 1997). Although small amounts of hydrated ACC can exist, most of the ACC is anhydrous (Addadi *et al.* 2003). The integration of the ACC into the forming spicule does not produce a net crystallization front and both phases are found juxtaposed in the surface of the forming spicule (Politi *et al.* 2008). This evidence suggests that ACC crystallize by secondary nucleation, where the transformation is induced by contact (Politi *et al.* 2008).

A similar mechanism has been proposed for the sea urchin tooth (Killian *et al.* 2009). It is composed of plates and fibres, which are single crystals of low-magnesium calcite, surrounded by a polycrystalline high-magnesium calcite matrix (Wang *et al.* 1997) that is secreted afterwards. These three structural elements are highly aligned (Ma *et al.* 2009), and two *c*-axis orientation exist: the one of the plates and the one that the fibres and the matrix share (Killian *et al.* 2009). When some fibres are misaligned, the surrounding matrix acquires the same orientation, suggesting that alignment is transferred by secondary nucleation (Killian *et al.* 2009).

It is interesting to note that these examples argue for a secondary nucleation mechanism for the transformation of the added ACC onto a *seed* (i.e. the rhombohedral calcite crystal in sea urchin larval spicules). For the ACC transformation to a crystalline phase to be triggered it is necessary to surpass an activation energy barrier. In the case of ACC to calcite is extremely high ($\sim 245 \text{ kJ mol}^{-1}$) (Ihly *et al.* 2014); other activation energies of dehydration of crystalline solids are around $\sim 100 \text{ kJ mol}^{-1}$ (Galwey *et al.* 2000). This means that for the reaction to take place at room temperature, another mechanism with low energy activation barrier should operate.

2.5.2 Dissolution–reprecipitation mechanism

A dissolution–reprecipitation mechanism involves the dissolution of the parent phase and the precipitation of a secondary (usually more stable) phase at the surface of the parent phase (Putnis and Putnis 2007). This mechanism operates when a solvent is present and has been proposed as an alternative to a solid-state transformation of ACC in synthetic systems (Aizenberg *et al.* 2003, Xu *et al.* 2006). The former process involves the precipitation of the anhydrous ACC (in solution) at the expenses of the dissolution of the hydrated phase of ACC (Rodríguez-Navarro *et al.* 2015). In air, an increase of the ambient humidity ($\sim 85\%$) would be enough to trigger the transformation (Xu *et al.* 2006) by forming a thin layer of water (2-5 nm) around the ACC particles (Rodríguez-Navarro *et al.* 2015).

The preservation of the morphology of the parent phase and the crystallographic orientation matching between the parent and the product phases have been largely interpreted as a result of a solid-state mechanism. Nevertheless, in a fluid boundary, the epitaxial precipitation of the product

also maintains the crystallographic relationships and the morphology of the parent phase (Putnis and Putnis 2007).

2.5.3 Further discussion about transformation mechanisms

In biogenic systems, the stabilization of ACC to avoid fast transformation is achieved by the addition of soluble macromolecules and ions, such as Mg^{+2} , silica, sulphate and phosphate (Aizenber *et al.* 1996, Gal *et al.* 2013) and by enclosing it in an impermeable organic sheath (Beniash *et al.* 1999, Gal *et al.* 2013).

The sea urchin larval spicule grows in the absence of water surrounded by the syncytial membrane (Beniash *et al.* 1999). The plant cystoliths, the amorphous calcium carbonate concretions formed in the leaves of certain plants, are stable for long periods. This is achieved with a polysaccharide-rich overlay (Gal *et al.* 2012). In molluscs, the silk fibroin gel (a hydrophobic proteinaceous gel that fills the spaces enclosed by the interlamellar membranes where the mineral grows) has been proposed to fulfil the same function, by avoiding the contact with water molecules (Weiner *et al.* 2005). Accordingly, the coating of the ACC nanoparticles seems to be an efficient method to avoid crystallization.

Working with synthetic ACC coated particles, Ihli *et al.* (2014) demonstrated the presence of small amounts of water in the ACC nanoparticles and the need of an initial dehydration to trigger the crystallization of ACC (both in water and in air). This dehydration was delayed by coating of the ACC particles, which provided a barrier to water. The authors proposed a coupled mechanism for the transformation of ACC nanoparticles: the water present on the particle surface could initiate a local

dissolution-precipitation process followed by the crystallization of the bulk material by solid-state transformation.

Although the exact sequence of events is still unknown, and both transformation mechanisms could cooperate for the crystallization of ACC in biogenic systems, what seems to be clear is that the dehydration process is a key step in the transformation of ACC. The changes in the structure and the removal of water are intimately linked, and to make dehydration possible at ambient temperature, the water must be transferred to a state that lowers the free energy of the system or an active transport (with ATP expenditure) must be involved (Navrotsky 2004).

Chapter 3

Role of vesicles in biomineralization

3.1 Introduction

The presence of vesicles has been described in different stages of the most common crystallization pathways with different roles (Weiner and Adaddi 2011). Vesicles are fluid-filled compartments generally enclosed by a double lipidic membrane (4 to 5 nm thick) crossed by transmembrane proteins. The interior of a vesicle constitutes an encapsulated space where the ion content and the permeability can be finely tuned (Mann 2001). The supersaturation is controlled by multi-subunit complex proteins that act as transport channels for specific ions and molecules. The mechanisms involved in the regulation of the vesicle ion content are the same that act in other parts of the organism (ion pumping, ion complexation and enzymatic regulation) with the advantage of containing a reduced volume (Mann 2001).

Ion pumps are transmembrane proteins that transport different ions against gradient with the hydrolysis of adenosine triphosphate (ATP) to adenosine diphosphate (ADP). They normally transport two different ions with the same electrical charge in opposite directions across the membrane. The enzyme Ca^{+2} -ATPase pumps Ca^{+2} against gradient while removing 2H^{+} , which indirectly helps to concentrate carbonate ions by the removal of protons ($\text{HCO}_3^{-} \rightarrow \text{CO}_3^{-2}$). The Ca^{+2} -ATPase is implicated in the transport of Ca^{+2} ions to the mineralization compartment in coccolithophorids (Klaveness 1976, Okazaki *et al.* 1984), corals (Isa *et al.* 1980, Kingsley and Watabe 1985), bird eggs (Coty and McConkey 1982), and bones (Shen *et al.* 1983).

The ion complexation mechanism implies binding of the cations to be transported with ligands as citrate or pyrophosphate to reduce the supersaturation (Mann 2001).

In the enzymatic regulation of the supersaturation, one of the main enzymes that participate in active calcification is carbonic anhydrase (CA). CA is a superfamily of enzymes that catalyse the conversion of carbon dioxide and water into bicarbonate and protons ($\text{CO}_2 + \text{H}_2\text{O} \leftrightarrow \text{HCO}_3^{-} + \text{H}^{+}$). It takes part in the acid-base balance and participates in diverse biological functions (Tashian 1989). CA activity has been identified in calcifying cells responsible for skeleton formation and in the organic matrices of thirty calcifying species (Le Roy *et al.* 2012), probably facilitating the input of inorganic carbon within the calcifying medium. In molluscs, a tissue specific CA was recently discovered in the outer mantle epithelium of *Haliotis tuberculata* (Le Roy *et al.* 2012). The active site of the transmembrane

domain is located in the extracellular medium; accordingly, the enzyme is only active in the extrapallial space. No other CA sequences have been detected in the shell matrix (Marie *et al.* 2010).

3.2 Ion uptake

The calcium concentration in the cytoplasm of eukaryotic cells is maintained rather low (10^{-7} M) in comparison to the free calcium in the extracellular fluids (10^{-3} M) (Mann 2001). Calcium acts as an intracellular signalling molecule and is involved in multiple biological processes (muscle contraction, glycolysis and gluconeogenesis, ion transport, cell division and growth) (Forsen and Kordel 1994). Small concentration changes might trigger multiple chemical reactions inside the cell. Therefore intracellular calcium transport implies specialized mechanisms to maintain the low concentration.

The direct participation of vesicles in the calcium uptake for biomineralization was first described by Bentov *et al.* (2009) in foraminifera. Foraminifera are unicellular organisms that generate an extracellular skeleton of calcium carbonate. The authors identified three different vesicle formation processes that introduced sea water to the cytoplasm: vesicles of less than 1 μm , between 1-5 μm and large vacuoles ($> 5 \mu\text{m}$). By adding a membrane-impermeable fluorescent dye to the water, they could track the transport to the mineralization compartment, demonstrating that the water introduced into the cytoplasm was not transported by transmembrane channels.

By using a pH-dependent dye, they showed that the pH inside most of the vesicles was higher than that of sea water (pH ~ 8.7 vs. ~ 8.2 of sea water).

This is a striking result, since pinocytosis processes generally imply the acidification of the vesicle fluid (Swanson and Watts 1995). The alkalisation mechanism is unknown, but it is likely that it is carried out by ion pumps and/or enzymes in the vesicle membrane. Alkalinisation facilitates the concentration of carbonate ions, which are likely to function as a carbon source for mineralization (Bentov *et al.* 2009).

Recent studies have demonstrated the participation of vesicles in the ion uptake mechanism of the sea urchin embryo (Vidavsky *et al.* 2016). By means of fluorescence confocal microscopy, the authors demonstrated that calcium ions first penetrate into the blastocoel in the form of free ions, which are afterwards introduced into the primary mesenchymal cells (PMCs) by an endocytosis mechanism. Nevertheless, this mechanism is not exclusive, but works together with L-calcium channels. The inhibition of the L-calcium channels does not inhibit the first deposition of the calcite rhombohedral core, but precludes the elongation of the triradiate spicules (Vidavski *et al.* 2016), which demonstrates that both mechanisms are required for the spicule to grow.

3.3 Stabilization of the amorphous phase

Vesicles concentrate ions that might precipitate, forming disordered mineral phases (Beniash *et al.* 1999, Mahamid *et al.* 2010).

In the sea urchin larvae, PMCs are the cells responsible for spicule formation and surround the membrane-delimited spiculogenic compartment. Large amounts of calcium-containing vesicles were detected in the Golgi complex of these cells (Decker *et al.* 1987), which transport calcium

intracellularly and fuse with the spiculogenic compartment (Decker and Lennarz 1988). Beniash *et al.* (1999) detected for the first time the presence of amorphous calcium carbonate (ACC) granules in the cytoplasm of these cells. A subsequent study with cryo-SEM, which allows a better preservation of the cell native state, showed the presence of a multitude of vesicles (0.5 – 1.5 μm in diameter), some apparently empty but others containing solid calcium carbonate aggregates (Vidavsky *et al.* 2014). Although the polymorph nature was not confirmed in this study, the morphology of the nanospheres (20 – 30 nm in diameter) points to an ACC nature.

A similar strategy is followed in bone formation. In mouse calvaria, several types of cells adjacent to the forming bone (pre-osteoblasts, osteoblasts and osteocytes) form intracellular mineral-bearing vesicles (Mahamid *et al.* 2011). These vesicles (1 μm in diameter) enclose membrane-bound amorphous calcium phosphate (ACP) granules (~80 nm) which in turn are composed of smaller globules (~10 nm). Interestingly, the relative concentration of phosphate inside the vesicles is high, which inhibits the crystallization of hydroxyapatite. It is likely that these vesicles extrude their content into the extracellular matrix by direct exocytosis, as was observed in an *in vitro* study of osteoblast (Rohde and Mayer 2007).

These recent studies involving a transient amorphous phase challenge the previous models of bone mineralization. The matrix vesicle (MV) model focuses on the role of extracellular vesicles as mineral transporters to the collagen matrix (Anderson 1995). It establishes that ion concentration inside the vesicles proceeds extracellularly by a complex pool of transmembrane enzymes located in the vesicle membrane (Anderson 2003).

The Ca^{+2} concentration increases inside the vesicles by a combined action of calcium binding proteins such as annexins, which function as transmembrane Ca^{+2} channels, and the calcium binding acidic phospholipids, located in the inner membrane of the vesicles. The PO_4^{-3} concentration is raised principally by enzymes like alkaline phosphatase and a Na^+ -dependent P_i transport system (Montessuit *et al.* 1991). When the concentration of Ca^{+2} and PO_4^{-3} ions exceeds the solubility product, precipitation of CaPO_4 crystals occurs inside the vesicles (Anderson 1995). The first crystals would be stabilized by the transmembrane CA enzyme (Stechschulte *et al.* 1992) by preventing the acidification of the vesicle interior.

The connexion between the two models (intracellular ACC-bearing vesicles *vs.* extracellular matrix vesicles) is unclear, and bone formation might proceed via cooperative/redundant mechanisms. Nevertheless the presence of the amorphous phase in the matrix vesicles might have gone unnoticed, which would question if the hydroxyapatite really crystallizes inside the vesicles or if it does when the content is released. Further investigation is required to clarify the exact sequence of events.

Another interesting example of the stabilization of an amorphous phase inside vesicles exists in prokaryotes. Magnetotactic bacteria are a polyphyletic group of bacteria that use magnetic particles (~30 nm) to orientate through a magnetic field. These iron oxide particles are formed inside a chain of specialized phospholipidic vesicles (the magnetosomes) by precipitation of amorphous iron oxide. The magnetosome vesicles exist before the nucleation of the iron oxide crystals, which takes place simultaneously on the inner surface of the membrane (Komeili *et al.* 2004). The even distribution of the nucleation sites indicates the existence of

polarity in the localization of the membrane proteins that direct nucleation (Komeili *et al.* 2004).

3.4 Deposition of the mineral phase

The deposition of the mineral phase is not clear, and two main hypotheses are considered: (i) a process of direct exocytosis or (ii) a process of dissolution of the transient phase.

In sea urchin larvae, small vesicles and mineral granules have been observed at the interface between the PMCs and the membrane of the spicule compartment (Vidavski *et al.* 2014). This suggests that mineral is exocytosed in solid state to the spicule compartment, where it integrates to the spicule (Beniash *et al.* 1999). If the phospholipid membrane stabilises the ACC, the vesicle fusion and the ACC release might trigger the crystallization process (Weiner and Addadi 2011).

In the limpet tooth radula, no presence of vesicles or preformed spaces has been detected. It seems that mineral is secreted by the adjacent cells and is deposited directly over a preformed chitin matrix. Although cells store iron as ferrihydrite, a metastable phase, it seems that the goethite deposition does not involve this precursor. So it is likely that the deposition is carried out by the dissolution and subsequent transport of the constituent ions (Sone *et al.* 2007).

3.5 The gastropod vesicle transport system

In nacreous gastropods Checa *et al.* (2009) highlighted the existence of a myriad of vesicles over the membrane that encloses the mineralization compartment, the surface membrane (SM). This membrane, of unknown composition, lies between the mantle cells and the growing nacre. Nakahara (1979) imaged it for the first time, and was thereafter recognized in additional nacreous gastropods (Cartwright and Checa 2007).

The double membrane (10-15 nm in thickness) vesicles are presumably secreted by the mantle cells and progressively fuse into the SM; at the nacre side, the interlamellar membranes (ILMs) detached from the SM. This scenario suggests that the SM maintains a dynamic equilibrium whereby the material supplied by the vesicles is added at one side and released at the opposite side in the form of interlamellar membranes (Checa *et al.* 2009).

Chapter 4

Nacre

4.1 Introduction

Nacre is an organomineral composite made of the calcium carbonate mineral aragonite with small amounts of proteins and polysaccharides which is secreted by some molluscs. It could have appeared independently in the Late Cambrian or Ordovician (during the Great Ordovician Biodiversification Event), in monoplacophorans, gastropods, bivalves and cephalopods (Vendrasco *et al.* 2011). Currently it is still present in the same four classes, but with a lesser prevalence.

Nacre is one of the most studied mollusc microstructures, partly due to its mechanical properties, beauty and economic interest. The high resistance of nacre to fracture (around 3000 times more than its inorganic counterpart, Jackson *et al.* 1988) is related with the alternation of organic and inorganic

layers in the structure. The organic layers absorb much of the energy by shearing (Currey 1990) in such a way that it hinders the propagation of cracks.

The main economic interest of nacre is due to the pearl industry. More than 20 tons of marine cultured pearls and 1500 tons of freshwater cultured pearls are yearly produced only in China, the world's larger producer of pearls. The pearl jewellery industry represents a global market of 5 billions of dollars annually (Anon 2006), so methods to improve breeding, harvesting, and quality of pearls are continuously under research (Yu and Chu 2006, Liu *et al.* 2017).

4.2 Secretion

Shell secretion is carried out by the mantle cells, a secretory epithelium which extrudes all the components that constitute the different layers. A highly cross-linked proteinaceous layer (the periostracum) is secreted in the first place. It is assembled in the periostracal groove, between the two outermost mantle folds, and functions as a matrix for the first mineral deposits. Immediately, a prismatic layer either calcitic or aragonitic is formed, and nacre grows internal to it.

The nacre components are secreted by the mantle cells. The surface of the mantle cells are covered by microvilli that project into the extrapallial space in close proximity to the forming nacre (Bevelander and Nakahara 1969). It is not well understood how the nacre components organize for the formation of the organic sheets and their subsequent mineralization. It is thought that an auto-organization process of the macromolecules in the extrapallial space

leads to the formation of the interlamellar membranes (Cartwright and Checa 2007).

Nacre formation starts with the segregation of the so called interlamellar membranes (ILMs). Bevelander and Nakahara (1969) were the first to highlight the importance of these organic sheets. The ILMs form compartments where the crystals grow, and they account for the uniform thickness of the tablets (~500 nm) (Nakahara 1991). ILMs are composed of polysaccharides (β -chitin) and acidic proteins, which adopt antiparallel β -sheet conformation (Weiner and Traub 1980). These membranes contain pores, whose sizes and frequency are different between bivalves and gastropods (Grégoire *et al.* 1955). It is not clear if chitin is present in all species and the amount is rather low (Goffinet and Jeuniaux 1979, Osuna-Mascaró *et al.* 2015).

The formation of nacre differs by groups. In bivalves, nacre grows in a terrace-like manner (Bevelander and Nakahara 1969, Nakahara 1991). The lamellae are formed parallel to the mantle surface, and the new tablets emerge close to the boundaries of the tablets of the previous lamella. Several layers can be formed at the same time, producing a stepped or terraced pattern. In gastropods, nacre tablets are stacked vertically forming columns (Wise and Hay 1968). The mineralization compartment is delimited by a dense organic sheet, the surface membrane (SM) (Nakahara 1979) that is absent in bivalves; under the SM, the ILMs are distributed in parallel.

The tablets first grow vertically, always in contact with the SM; when the core of the tablet reaches the definitive height, the tablet starts to expand sideward (Checa *et al.* 2009). Well before it impinges on the corresponding tablet of the neighbouring tower, another tablet grows on top of it, always

along the tower axis; in this way, each stack adopts a pyramidal shape (Nakahara 1979).

4.3 Crystallography

The first study on the crystallography of nacre was made by Schmidt (1922). In this first paper, he established that the aragonite c -axis was perpendicular to the shell surface. In subsequent papers (1923, 1924) he inferred the orientation of the a - and b -axes based on the outlines of the tablets. Successive studies based on electron microscopy (Grégoire 1962, Wada 1972) corroborated Schmidt's findings.

Nacre tablets show invariably their c -axis nearly perpendicular to the tablet, oriented towards the outer surface of the layer. Nevertheless the orientation of the a - and b -axis varies by groups. The first studies in bivalves showed that the a - and b -axes of tablets were co-aligned. The a -axis was aligned parallel to the growth lines and the b -axis along the local growth direction of the shell (Wada 1958). Subsequent studies with EBSD (Dalbeck *et al.* 2006, England *et al.* 2007) demonstrated some degree of rotation between the a - and b -axes. Frýda *et al.* (2010) showed that the a - and b -axes are distributed randomly in some bivalve species (*Mytilus californianus*, *M. galloprovincialis*, *M. edulis* and *Nucula nucleus*). This was confirmed in *Mytilus edulis* by Griesshaber *et al.* (2013), who, at the same time, showed that crystal co-orientation could extend up to 20 stacked tablets, often obliquely aligned.

Gastropods tablets have their a - and b -axes randomly oriented. Tablets stacked along a single column show great c -axis co-orientation. Sarikaya and

Aksay (1992) described that the c -axis oscillates by $0\text{--}5^\circ$ from one tablet to the next.

Subsequent studies based on electron diffraction (Gries *et al.* 2009), X-ray diffraction (Younis *et al.* 2012), TEM/STEM (Checa *et al.* 2011) and polarization-dependent imaging contrast (PIC) images (Olson *et al.* 2013) gave a c -axis misorientation of 2° or less between tablets stacked along a single column. The changes in the orientation between adjacent columns reach a c -axis spread of $\pm 10^\circ$ (Olson *et al.* 2013).

It is interesting to mention that the first $50\ \mu\text{m}$ of nacre from the prismatic layer underneath present great disordering regarding c -axis orientation (up to 180°), which is reduced gradually within the nacre (Gilbert *et al.* 2008).

4.4 Mineral bridges

The perfect alignment of the crystallographic axes in nacre is difficult to explain if a new nucleation event would be necessary in each tablet. Currently the existence of mineral bridges in nacre, both in gastropods and bivalves, is accepted, although it was largely debated in the past. Schäffer *et al.* (1997) were the first to propose the growth of nacre through mineral bridges rather than by heteroepitaxial nucleation. They presented evidence based on AFM about the presence of pores (5-50 nm in diameter) in the interlamellar membranes that would allow the initiation of a new tablet as an offshoot of the underlying tablet through the pore. This paper fostered new research about the growth of nacre tablets.

A series of papers were published afterwards (Barthelat *et al.* 2006, Lin *et al.* 2008, Gries *et al.* 2009), which bring up the possibility of the existence of mineral bridges. The problem focused on whether the nanoasperities or hillocks, the protrusions of the surface of nacre tablets which intrude the pores of the interlamellar membranes, were continuous between two superimposed tablets. Hillocks and tablets are normally co-oriented, which gives the false impression of being crystallographically continuous (Checa *et al.* 2011).

The unequivocal demonstration of the existence of mineral bridges in nacre was made by Checa and collaborators in two successive papers (2009, 2011). In the first one, the presence of an organic-rich tower axis continuous throughout the superimposed tablets was shown. The core of each new forming tablet (the tip of the column) grows in contact with the surface membrane from where organic molecules are adsorbed. Once the core reaches its full height, a new ILM is secreted and the tablet starts to grow laterally (Checa *et al.* 2009).

In the second paper (Checa *et al.* 2011) by means of HRTEM and tomography, the authors demonstrated the alignment of holes in the ILMs of gastropod nacre, through which the mineral bridge goes through. In bivalves, these holes are not aligned, but close to the boundaries of the tablets. The authors proposed a model that explains the breakage of the ILM by the rise of the osmotic pressure when the tablet underneath is in an advanced stage of growth, due to the concentration of organic molecules in the compartment. The hole enables another tablet to grow on the boundary of the parent tablet, maintaining the crystallographic continuity. The disposition of holes at the

edges of the tablets explains why co-aligned tablets are staggered in bivalves (Checa *et al.* 2011, Griesshaber *et al.* 2013, Olson *et al.* 2013).

Chapter 5

Materials and methods

5.1 Material

Along this PhD study, we have mainly worked with the nacreous gastropod species, *Phorcus turbinatus* (Born 1978), family Trochidae (Rafinesque 1815), Vetigastropoda. It is a middle size (15-45 mm) sea snail, with a more or less elevated conical shell. The genus is characterized by a fibrous prismatic outer shell layer, a nacreous middle shell layer and by an internal platy aragonitic layer with nacreous lustre. All the specimens were caught in La Herradura (36° 43' 44'' N, 3° 43' 35'' W), at the intertidal zone of the coast of the province of Granada (south Spain).

For the study of the lineations of nacre tablets, we selected a representative group of bivalves (7), gastropods (3) and cephalopods (1) nacreous species. They are listed herein:

- Bivalves: *Acila divaricata* (Turtle Island, Taiwan), *Nucula nitidosa* (Málaga coast, Spain), *Perna viridis* (loc. unknown, Indonesia), *Pinctada margaritifera* (French Polynesia), *Anodonta cygnea* (Mira, Portugal), *Pinna nobilis* (coast of Almería, Spain), *Pteria hirundo* (Fuengirola, Spain).
- Gastropods: *Bolma rugosa* (Granada coast, Spain), *Gibbula cineraria* (Quiberon, France), *Gibbula umbilicalis* (São Jacinto, Portugal).
- Cephalopod: *Nautilus pompilius* (loc. unknown).

5.2 Treatments

Etching treatments were widely used in early biomineralization studies (Mutvei 1977, 1978, 1979). The aim is to erode the surface of the material to gain insight into the inner structure. Mutvei (1977) developed a protocol which mixed diluted acetic acid (pH 3–4) and glutaraldehyde solution (12%), with the aim of fixing the partially soluble organic matrix of nacre (Crenshaw 1972) as the dissolution takes place. The protocol was applied in combination with sodium hypochlorite for cleaning the surface of the sample. The steps and times are as follow: sodium hypochlorite 10% (step 1) for 2–30 min → glutaraldehyde 25% + acetic acid 1% in cacodylate buffer (step 2) for 2–10 min → sodium hypochlorite 1% (step 3) for 1–5 days (optional).

To reduce the protein content from the surface of the sample, a proteinase K treatment (0.1 or 0.2 g/ml for 1–2 h at 30°C) was applied to some samples. After deproteinization, samples were washed three times for ten minutes under constant stirring in saline solution (Phosphate Buffered Saline, PBS) and additionally washed for ten minutes in milli-Q water.

5.3 Electron back scattered diffraction (EBSD)

EBSD is a technique based on the analysis of the Kikuchi patterns that arise from the interaction of the electron beam with the surface of a crystalline sample, normally in a scanning electron microscope (SEM), although STEM/EBSD and TEM/EBSD are presently available. The electrons from the incident beam are diffracted by crystalline planes and leave the sample surface as backscattered electrons. Viewed in three dimensions, these electrons form diffraction cones of different intensity and angle which are recorded as lines (the Kikuchi lines) on the detector screen. These lines form patterns (the Kikuchi patterns), which are characteristic of the phase and the orientation of the crystal (Williams and Carter 2009).

For EBSD a very finely polished sample is located at an angle of 20° to the incident beam (70° if we take into account the stage tilt). Accelerating voltages of 10-30 kV and beam currents of 1-50 nA are normally used (Maitland and Sitzman 2007). The spatial resolution of the technique is defined by the electron optics of the SEM, but with a field emission SEM (FESEM) grains as small as 100 nm for carbonates and 20 nm for materials with high atomic number can be resolved (Troost 1993).

With the aim of relating the morphology of the tablet surface with the crystallography, we performed EBSD on unpolished samples. The percentage of indexable patterns dropped drastically compared with polished samples, because this technique is very sensitive to surface irregularities, although relevant information was obtained. We used two sets of equipment. First, we used an Inca Crystal (Oxford Instruments) detector coupled to a Gemini-1530 (Carl Zeiss) FESEM (Scientific Instrumentation Centre (CIC), Universidad de Granada). To avoid excessive charging, samples were coated with a

thickness of 2 nm of carbon in a Baltec MED 020 electron beam evaporator. The second equipment was an Edax detector coupled to FEI Field Emission Gun (FEG) SEM Quanta 3D micro-scope of the Institute of Metallurgy and Materials Science of the Polish Academy of Sciences (IMIM, Krakow, Poland). Operation in low vacuum mode made coating unnecessary.

5.4 Atomic force microscopy (AFM)

AFM is a kind of scanning probe microscopy (SPM) that forms images by scanning a physical probe over the surface of the specimen. In AFM the probe is a sharp metallic tip (15–40 nm wide) located in a cantilever. The interaction of the tip with the sample surface causes the cantilever to deflect laterally and vertically. The vibration of the cantilever is transmitted by a laser to a photo-detector. The laser is focused over the cantilever, and its reflection strikes a position-sensitive photo-detector divided in four segments. The laser deviations allow measuring the surface topography at atomic resolution (Fig. 5.1).

Two main modes are used. In contact mode the tip is static and it is dragged across the surface of the sample; the short range repulsive forces are mostly monitored (i.e. electron-electron Coulomb interactions). In tapping mode the tip oscillates during the displacement; the attractive forces are recorded (van der Waals interactions, electrostatic forces and chemical forces). Tapping mode produces less damage on the sample surface and is therefore more suitable for organic samples.

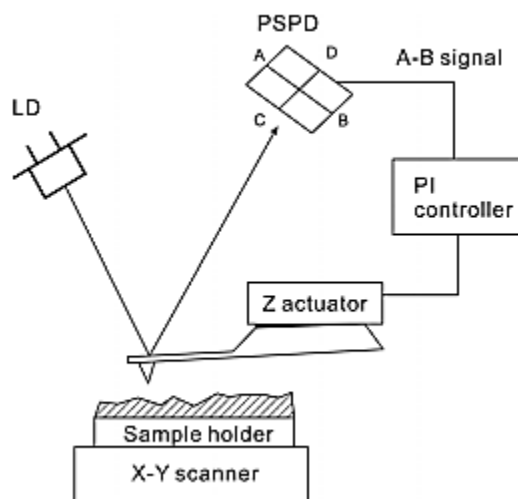


Fig. 5.1. AFM principle. A laser beam from a laser diode (LD) is focused at the end of the cantilever, and a reflected beam is aligned at the centre of the position-sensitive photo diode (PSPD). When the cantilever bends, the A–B signal of the PSPD is changed and transmitted to the proportion-integration (PI) controller to control the height of the cantilever through the Z-actuator (from Seo and Jhe 2008).

For the study of lineations we prepared both, polished and unpolished samples. For polishing, we used Struers water-grinding papers (DP Mol and DP Dur), followed by a thin polishing with Struers diamond pastes (3, 1, and 0.25 μm) and finally with silica gel suspension (~ 3 h). The sample was etched in a 0.1 wt% acetic acid with 3% glutaraldehyde solution for 8 s. It was later repolished, immersed in commercial bleach for ~ 90 s and dried before placing in the AFM sample holder. The bleached or protease-treated samples were scanned without polishing. Observations were made both in air and liquid.

For the study of the nanogranularity and its relation with the amorphous phase, AFM was performed directly on the TEM grids. Areas of interest were previously selected by SEM on uncoated samples (Phenom Pro, University of Granada, Spain) and later manually located under the AFM using the X-Y translator of the optical head. Images were recorded in air at room temperature. Different areas of the sample were scanned using a $\sim 14 \times 14 \mu\text{m}^2$ piezo scanner and tips with a nominal radius of 8 nm supported by rectangular cantilevers with a nominal resonance frequency of 320 kHz, and a maximum spring constant of 80 N/m (Bruker TESP-V2). The scan rate was set to 1 Hz, and 256 to 512 lines per scan were recorded.

All the observations were made using an AFM (Multimode IIIa Veeco Instruments) of the Centro Nacional de Microscopía Electrónica (Universidad Complutense de Madrid, Spain). Recorded AFM images were subsequently analyzed using the Nanoscope 5.30 and Nanotec WSxM 2.1 software's (Horcas *et al.* 2007).

5.5 Transmission electron microscopy (TEM)

Electron microscopy is a family of microscopy techniques that use electrons instead of light as source of illumination. In these microscopes an electron beam is accelerated and projected towards the sample by means of electromagnetic lenses. The interaction of the electrons with the specimen produces multiple signals that are analysed by a combination of imaging and spectroscopic techniques. These signals give insight about the structure, topology, morphology and composition of the materials at nanometre scale.

The employment of electrons overcomes the limitation in resolution typically found in optical microscopes. The resolution limit of optical microscopy and, in general, of any optical system was envisaged by Ernst Abbe in 1873. The *Abbe diffraction limit* states that the propagation of a wave throughout an aperture generates greater interference as the size of the aperture is reduced (resulting in blurred or distorted images). That means that for a fixed small aperture, a shorter wavelength allows a higher resolution (Abbe 1873).

The resolution is defined as the minimum distance at which two proximal features can be distinguished:

$$\text{Resolution (r)} = \lambda / (2\text{NA})$$

where λ is the wavelength of the source (the mid spectrum wavelength of light is $\lambda = 550$ nm) and NA is the numerical aperture of the lens, which varies between 0.95 in air and 1.5 in oil. The maximum resolution of light microscopy at 100x magnification is around 200 nm.

The possibility of using an electron source (with a wavelength 1000 times shorter than that of light) was envisaged by Hans Busch in 1927. He theoretically demonstrated that electrons can be focused when they go through a magnetic field generated by a current applied to a coil. Even more interesting, he stated that it is possible to modify the focal length (the distance at which a parallel beam converges into a single point) by varying the intensity of the current. This implies that a magnetic field affects the electron beam in the same way that a glass lens affects light and it constitutes the basis of electron optics.

Ernst Ruska constructed the first electron-lens in 1931, experimentally demonstrating the Busch's equation. The design (a coil enclosed in an iron chassing with a narrow gap) remains unchanged until today. By placing two lenses one above the other, he demonstrated that the resulting magnification was the product of the magnifications of the two individual lenses (Hawkes 1990), like in an optical system. The first commercial electron microscope was produced by Ruska at Siemens in 1938.

5.5.1 The transmission electron microscope

The transmission electron microscope consists in an electron source (the electron gun) and a series of electromagnetic lenses that focus the beam through the specimen and form the image in a photographic plate or camera.

The electron gun can produce the electrons by heating (thermionic guns) normally a tungsten (W) metal filament or a LaB6 crystal, or by the application of an electric field (Field Electron Guns, FEG). These electrons are accelerated by applying an electric potential difference (accelerating

voltage, V_0), which in commercial TEMs varies between 100–300kV. The higher the accelerating voltage, the faster the electrons travel and the more penetrating power they have.

To avoid the dispersion of the electrons due to collisions with air molecules, high vacuum conditions are needed inside the column. The type of electron gun also determines the vacuum conditions needed (tungsten $\sim 10^{-5}$ Torr, LaB6 $\sim 10^{-7}$ Torr, FEG $\sim 10^{-10}$ Torr).

In a TEM there is a complex set of electromagnetic lenses located along the column that (1) form the beam and focus it (condenser lenses) and (2) form the image and magnify it (objective, diffraction, intermediate and projective lenses).

The condenser lenses (normally two sets) are located at the top of the column. Condenser lens 1 (C1) controls the amount of current that passes to the column and it is traditionally called *spot size*. The condenser lens 2 (C2) controls the *intensity* of the beam (the degree of focusing). The alignment of these two lenses makes the beam symmetrical and centred along the optical axes of the column.

The specimen is located below, and subsequently the objective lens. This is the most important lens of the microscope, since it creates the first image of the object that afterwards will be magnified by the rest of the lenses. If the objective lens is misaligned, it will not be possible to correct the errors introduced.

The objective lens forms a diffraction pattern in the back focal plane from the electrons scattered from the sample that afterwards are combined to form the first intermediate image (Fig. 5.2). Image and diffraction are

simultaneously present at the TEM. Switching from one mode to the other is achieved by changing the focus of the intermediate lens.

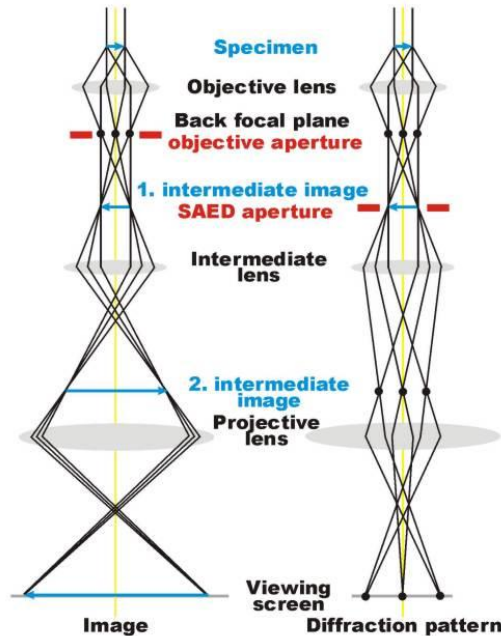


Fig. 5.2. Simplified ray diagram of the image and diffraction modes in the TEM (image from [www.ETH zürich.ch](http://www.ETH.zuerich.ch)).

Two main aberrations affect the electromagnetic lenses, the spherical aberration (C_s) and the chromatic aberration (C_c). The spherical aberration is due to the fact that electrons far from the axis are more strongly deflected than those closer to the centre. The chromatic aberration is caused by electrons with different wavelengths being deflected differently.

Spherical aberration has been the main limitation to achieve increasingly higher resolutions. Since magnetic lenses are far from being perfect, the magnetic field will never be perfectly symmetric, and in practice that means that spherical aberration cannot be eliminated. Nowadays spherical aberration

is corrected with the addition of one or two (TEM and STEM) correctors to the microscope column. This increases the complexity, since an aberration corrected microscope does not behave in the same way as a conventional TEM does.

All TEM characterization made during this PhD has been carried out in the Fritz Haber Institute of the Max Planck Society, in Berlin. There, I first learnt to operate a Philips CM200 fitted with a post-column energy filter (GIF Quantum, Gatan) and an Energy Dispersive X-ray (EDS) system (EDAX Genesis-4000). Afterwards, I got access to a Jeol JEM-ARM200F (Fig. 5.3), an state-of-the-art double Cs corrected microscope, fitted with a cold-field emission gun, an UltraScan 4000 camera (Gatan), a Imaging Filter (GIF Quantum, Gatan), an EDS detector (Jeol), and secondary (SE) and backscattered (BSE) electron detectors (Jeol).

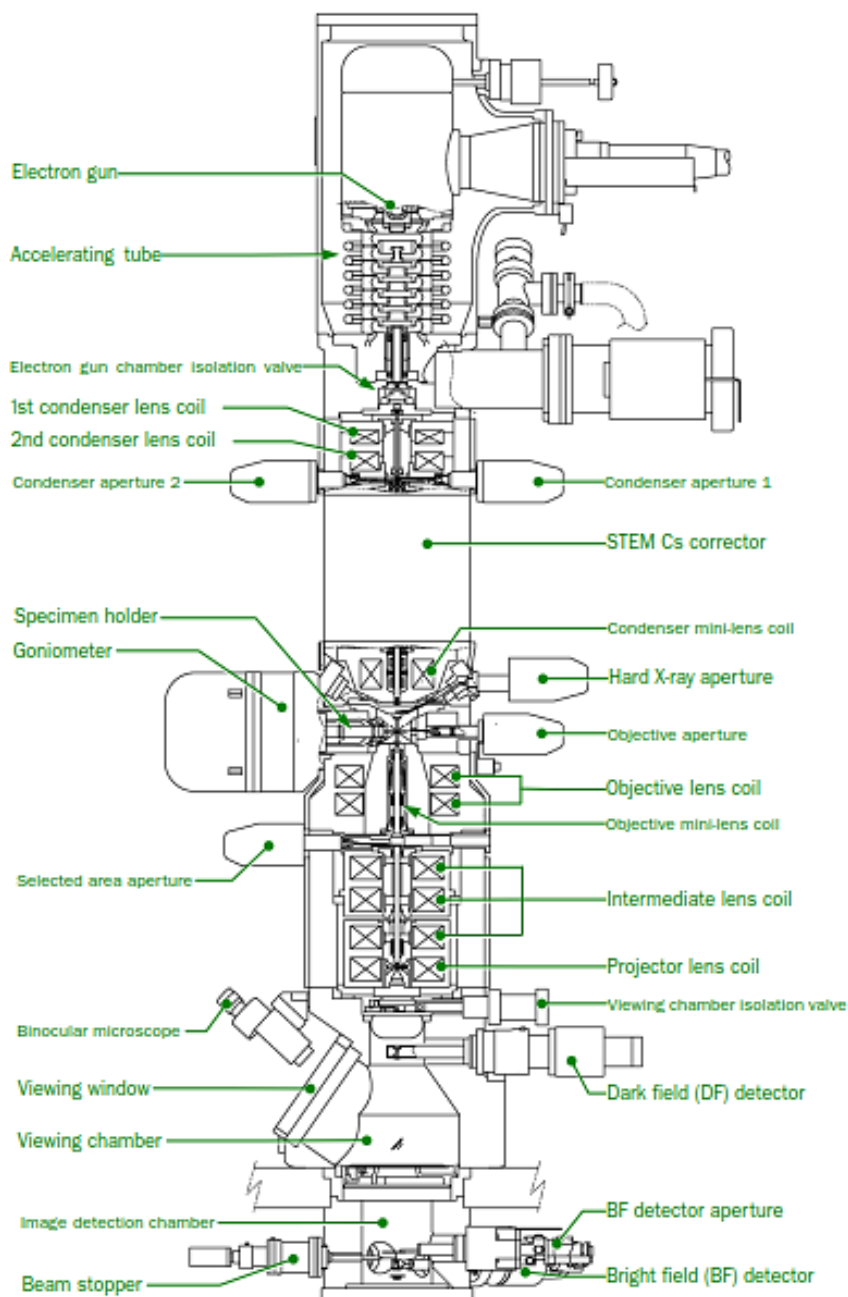


Fig. 5.3. Scheme of the double Cs corrected Jeol JEM-ARM200F used in this study. The location of the electromagnetic lenses, stigmators and deflectors is shown (image from Jeol JEM-ARM200F user manual).

5.5.2 Sample preparation

Due to the low penetration power of the electrons, TEM samples are thinned to 50-100 nm to allow the electrons to go through (in the same way light goes through a photographic slide). This is one of the main drawbacks of TEM, since sample preparation can be limiting and tedious.

Different sample preparation techniques have been used along this PhD study, with the aim of testing its suitability for the material and for achieving the different objectives. We have mainly used ultramicrotomy and a cross-section preparation procedure that combines mechanical thinning and ion milling. Because the main results were achieved with ultramicrotomy, I will only describe this method.

Ultramicrotomy consists in embedding a small piece of sample (0.5 x 0.5 mm) in a polymerizing resin that enables the specimen to maintain its structure during the cutting process. Once polymerized, the block is trimmed manually or with a trimming device.

The block is placed in the mobile arm of the ultramicrotome, which performs ellipsoidal movements over the diamond knife, which remains stationary. This design offers high stability and reduces the compression effects.

The diamond knife has a fluid collecting trough where the thin sections float after cutting. Thin sections are then collected (“fishing”) and located on the grids for staining and/or TEM observation. The ultramicrotome and the diamond knife were invented in 1951, allowing a great development of the TEM studies.

5.5.2.1 Fixation and embedding

Due to the vacuum conditions inside the microscope, samples must be previously dehydrated. Water is sequentially eliminated from the specimen and replaced by resin. Most of the protocols for biological samples entail a fixation pre-step and a final staining step (Hayat 1981). Fixation preserves the structure of the cells (volume, morphology and spatial relationships) by means of cross-linking of proteins (Hayat 2000). This protects the specimen against subsequent treatments (dehydration, staining, vacuum and beam exposure).

The goal of the study will determine the type of fixation method used. Fixation with a mixture of glutaraldehyde and formaldehyde followed by a postfixation with osmium tetroxide (OsO_4) is widely used for ultrastructure studies. Nevertheless, for the study of water-soluble molecules the freeze-drying method gives better results (Hayat 2000). Mobile molecules and ions are washed out in contact with aqueous solutions, so they must be avoided for applying analytical techniques.

We have used both protocols with different purposes: (1) the ultrastructural study of the surface membrane and the associated vesicles, for which we have used the chemical fixation, and (2) the study of the amorphous transient phase in nacre, for which we applied a freeze-drying protocol. Both are described below. The sample preparation, fixation and embedding protocols were carried out in the Sample Preparation Lab (LPMB) of the Scientific Instrumentation Centre (CIC) of the University of Granada by Juan de Dios Bueno Perez and/or in our group's lab in the Andalusian Institute of Earth Sciences (IACT) by the candidate.

i. Chemical fixation

Samples were prefixed in a mixture of 1.5% glutaraldehyde and 1% formaldehyde in cacodylate buffer 0.05 M at pH 7.4 for 15 minutes at 0-4 °C. Samples were cut in 1 mm³ fragments and maintained in the same solution between 45 min and 2 hours at 0-4 °C. Afterwards they were rinsed in cacodylate buffer 0.1 M three times for 10 minutes. The postfixation was carried out with 1% osmium tetroxide in water during 1 hour at 0-4 °C in darkness; pieces were subsequently washed in distilled water three times for 5 minutes. Dehydration was carried out in graded ethanol series (50, 70, 90, and 100%) at room temperature.

The infiltration with Embed 812 (EMS) epoxy resin was completed in three steps of one hour each by varying the relative proportion of ethanol and resin (1:2, 1:1, 2:1). For the final step, the sample was infiltrated with pure resin overnight at 0-4 °C. Polymerization was carried out in an oven at 60 °C during 48 hours.

ii. Freeze drying

Freeze drying involves the dehydration of a frozen sample by sublimation of ice. The fast freezing and the lack of chemical reagents ensure a more native state, although relative movement of the constituents might occur.

The specimens of *Phorcus turbinatus* were frozen in liquid nitrogen after capture and stored in a Dewar flask. Freeze-drying was carried out the day after; the initial temperature (-170 °C) was raised slowly at an average pressure of 75 mTorr (Flexi-Dry MP). At the end of the drying cycle (2 days), when room temperature was reached (20 °C), the specimens were removed and stored at 4 °C. This process implies the removal of unbound

water (sublimation phase or primary drying). Note that the extraction of bound water requires a second phase (secondary drying or desorption) at relatively high temperatures (25° to 40 °C) (Rey and May 2010).

Postfixation with osmium tetroxide was avoided, since heavy metals can interfere in the detection of light elements with analytical techniques by increasing the background. Embedding was accomplished in three steps with different proportions of resin to ethanol, and avoiding contact with water.

5.5.2.2 Sectioning

TEM studies of mineralized tissues are mainly limited by the difficulty of sectioning. Crystals can damage the edge of the diamond knife and the hardness difference between the two materials (the crystals and the resin) produces tension that results in breakage of the slices. Different aspects of the technique can be tuned in order to get slices good enough for TEM investigation. A low density resin (that infiltrates pores of small size), the increase of the amount of hardener in the resin (to reduce the tension between the materials) and a slow cutting speed are advisable to improve the quality of the slices. These and other hints are extensively explained in Hayat's books (Hayat 1981, 1993, 2000) which are recommended.

Thick sections (1 – 2 μm) of the chemically fixed samples were prepared for a preliminary study under the optical microscope. Sections were deposited on a microscope glass slide, stained with 1% toluidine blue and 1% borax in water and dried on a hot plate. Toluidine blue is a metachromatic dye that can produce different colours depending on how it chemically binds to the different cell components (Hayat 2000). The observation of the thick slices allows the location of the area of interest in the embedded sample,

which can be subsequently re-trimmed. The size of the block face should be less than 0.5 mm on a side. The smaller the block face, the less the compression, and the better the sections (Hayat 2000).

The trough of the diamond knife is typically filled with distilled water up to the formation of a meniscus. The water edge should be in any moment in contact with the border of the diamond knife, which allows the sections to float smoothly, ideally forming a ribbon. To avoid dissolution of mineralized samples, it can be useful to add calcium carbonate until saturation. Care should be taken not to exceed the CaCO_3 supersaturation, which would produce precipitates on the surface of the sample. In our case, the time of sample-water contact in the trough was minimized, by collecting the slices as soon as some of them were cut. Sectioning was carried out in the Fritz Haber Institute (Berlin) by the candidate using a PowerTome X Ultramicrotome (RMC Boeckeler) (Fig. 5.4).

To image the organic fraction, some grids were post-stained. Uranyl acetate in alcoholic solution partially dissolves the mineral (see for example, Bevelander and Nakahara 1969), so we used 1% uranyl acetate in aqueous solution during 1 minute followed by lead citrate for 5 minutes in a CO_2 -free atmosphere (Reynolds 1963).

To study the amorphous mineral phase and to apply analytical techniques, we avoided the use of any stain.

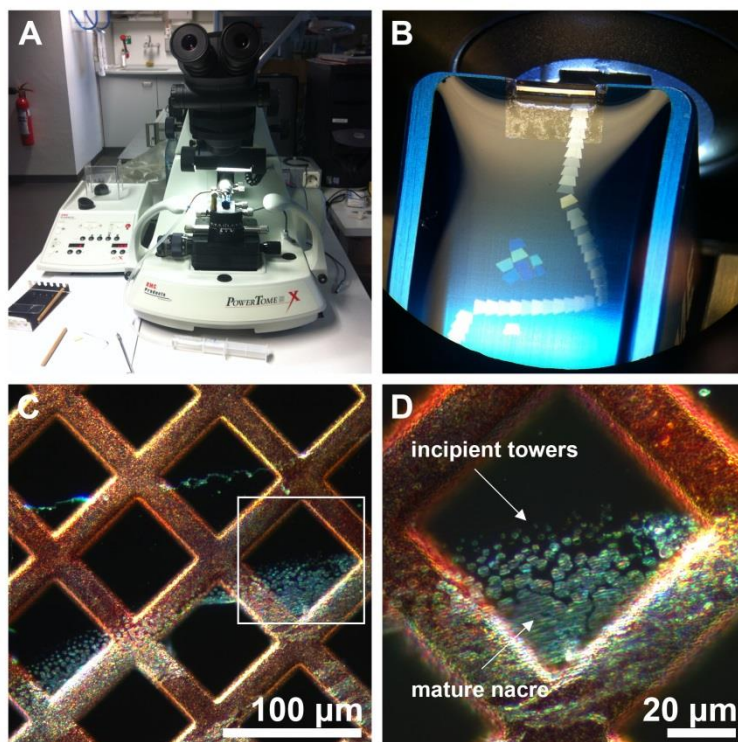


Fig. 5.4. Sectioning. A) The ultramicrotome PowerTome X (RMC Boeckeler) in the Fritz Haber Institute. B) Ribbon of slices floating in the trough. The light grey slices are around 60 nm in thickness whereas the silver ones range between 60-90 nm. C) A slice of *Phorcus turbinatus* nautilus. D) Closer view of the area framed in C) where it is possible to distinguish a strip of incipient towers (appearing as dots in top view) and an area of mature nacre (where the material becomes continuous).

5.5.3 High Resolution Transmission Electron Microscopy (HRTEM)

A HRTEM image results from the differences in the phase of the electron waves scattered through a specimen (i.e. it is an interference pattern). The fringes can appear by different mechanisms (Fresnel fringes, Moiré fringes), but in the case of lattice fringes they appear by a transmitted wave exiting from a crystal and a wave diffracted from one lattice plane of the crystal. The spacing between the fringes corresponds to that of the lattice planes.

The phase-contrast mechanism is very sensitive to orientation, thickness, focus or astigmatism, and sometimes phase-contrast images are difficult to interpret. However, this sensitivity is the reason why phase-contrast can be used to image the atomic structure of the materials.

5.5.3.1 Fast Fourier Transform (FFT) analysis

The Fourier transform (FT) is a mathematical transformation that decomposes any function (waveform) into a sum of simple sinusoids: a sum of sine and cosine functions (Brighan 1974). So any signal can be expressed as the frequencies that make it up. The fast Fourier transform (FFT) is an algorithm to compute the discrete Fourier transform, a simplified form of the FT. Its development facilitated its applicability, since high computational power is needed to perform it (Brigham 1974).

In optics there is a Fourier transform relation between the light amplitude distribution at the front and the back focal planes of a converging lens (Brigham 1974). In the TEM, which behaves similarly to an optical microscope, the objective lens performs (1) a FT that creates a diffraction

pattern in the back focal plane and (2) an inverse FT that combines again the diffracted beams forming an image in the image plane (Fig. 5.5).

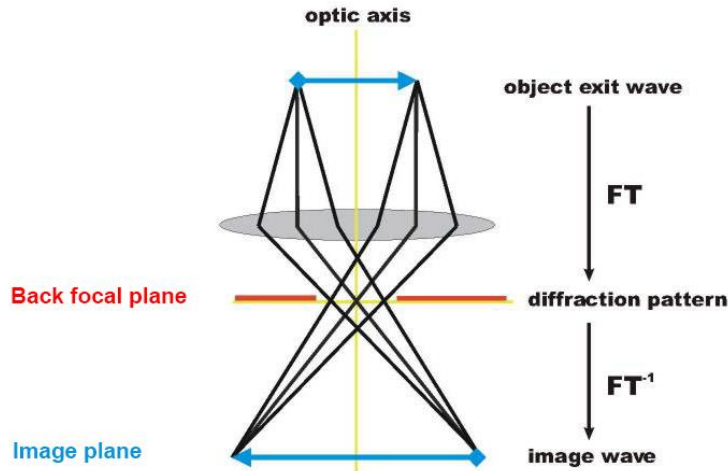


Fig. 5.5. FFT in the TEM. Mathematical interpretation of the ray diagram at the objective lens of a TEM (image modified from [www.ETH zürich.ch](http://www.ETH-zuerich.ch)).

In image processing, the FT works in a similar way. The image is decomposed into its sine and cosine components, giving back a set of points, each one representing a frequency. In HRTEM images, the periodic information that results from a set of lattice fringes is transformed by the FFT in a spot. Each spot is located at a distance $1/d$ (being d the interplanar spacing) from the centre (the transmitted beam). In this way, measuring the distances of each spot from the centre and the angles between them is possible to identify the planes (as we will see below).

The diffractogram that results from a FFT gives similar information as a diffraction pattern. The advantage against selected area electron diffraction (SAED) is that the FFT can be obtained from areas as small as dozens

nanometres in a HRTEM image (such as crystalline nanodomains). Although SAED is site-selective, it samples areas several hundred nanometres in size, which is determined by the diameter of the smallest selected area aperture (10 μm in the JEOL JEM-ARM200F).

5.5.3.2 Indexing

For indexing a diffraction pattern (or a diffractogram derived from a FFT) is necessary that the electron beam is along a low-index zone axis of the crystal. In the TEM this can be achieved by means of a double tilt holder that allows the tilting of the sample in two perpendicular directions.

The identification of the planes (that is given by their Miller indices, hkl) is carried out on the basis of the interplanar spacing (d -spacing) and the angles between them. In the diffractograms, we measured the distances r_1 and r_2 between the spots (reflections) and the centre (the transmitted beam), and the angle α between them (Fig.5.6).

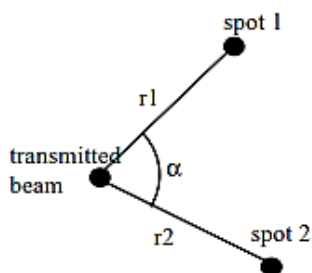


Fig. 5.6. Indexing of the reflections in a diffraction pattern (image from CaRine Crystallography).

The distances r ($r = 1/d$) and the angles between the spots (α) were extracted with the DiffTools script package (Mitchell 2008) for Digital

Micrograph (Gatan Inc.). These parameters were exported subsequently to CaRIne Crystallography 3.1 (Boudias and Monceau 1998), where we used the refined aragonite parameters of Caspi *et al.* (2005) to construct the unit cell model.

The approach for identifying the planes is to consult the tables of distances and angles for the low index reflections for the structure we are studying. That is what CaRIne software does, giving a list of the possible solutions of planes and angles ordered by ascending error (Boudias and Monceau 1998). In our study, the possible solutions (planes) with an error greater than 5% were discarded. For a coherent indexing, all the spots that form the diffraction pattern should share a zone axis.

Indexing allows an accurate identification of the crystal structure, thus enabling the differentiation between polymorphs (i.e. same chemical composition and different crystal structure), unlike other inaccurate approximations, such as measuring single d -spaces.

5.6 Electron Energy Loss Spectroscopy (EELS)

This analytical technique employs the focused electron beam of a TEM as a probe source to analyse the interaction with the specimen. The high-energy electrons of the beam (accelerated through a voltage about 100-300 keV in most commercial TEMs) interact with the atoms of the specimen, and part of its kinetic energy is transmitted to the material. The amount of energy absorbed depends strictly on the composition and the electronic structure of the atoms of the material, in such a way that measuring the loss of energy of

the primary electrons it is possible to identify, not only the elemental composition and distribution, but also the element local coordination, valence electron density for phase identification, anisotropic density of states, etc. (Egerton 2011).

When the electrons interact with the material they scatter, and both the amplitude and the phase of the incident electrons might change. The two main types of scattering are elastic and inelastic. Roughly, elastic scattering involves no change in energy and maintains the phase relationship (i.e. they are coherent) whereas inelastic scattering involves a loss in energy of the incident electrons, which lose the phase relationship between waves (i.e. incoherent) (Brydson 2001). The energy lost by the primary electrons is transferred to the electrons of the specimen, causing the atoms to move to an excited state. To return to their ground state a process of de-excitation occurs, which implies the liberation of the energy in form of X-rays, Auger electrons or photons (that also carry compositional information that can be analysed by other spectroscopic techniques) (Brydson 2001).

Inelastic scattering is the basis of the EEL spectroscopy, and the two main mechanisms of inelastic scattering that are measured are the *plasmon excitations* and the *single electron excitations* (Fig. 5.7A). The plasmon excitations occur when the primary electrons provoke collective excitations of the valence electrons of the atoms of the material, generating collective oscillations (plasmons). The energy loss ranges between 5 and 30 eV, so the plasmon excitations appear in the *low loss region* of the EELS spectrum. This mechanism is quite frequent, and the probability for it to occur increases with the material thickness. With the increase of the sample thickness it may also affect other inelastic signals in other parts of the spectrum (Brydson 2001).

The plasmon peak is used to measure sample thickness and to correct the effects of multiple inelastic scattering.

A single electron excitation occurs when the primary electron transfers part of its energy directly to a single inner shell electron of the material, producing ionization (so-called *ionization edges*) (Fig. 5.7B). The energy losses range from 50 to thousands of eV (the *core loss region* of the spectrum). The binding energy of a particular electron subshell within an atom is unique and characteristic of each element, so that it is possible to determine its nature. For example, to ionize a carbon electron located in the K shell 284 eV are necessary, but much more energy is needed to ionize a silicon electron in the same shell (1839 eV). The intensity of the edge is given by the number of atoms; it hence being possible to quantify them.

A typical spectrum plots the scattered electron intensity as a function of the decrease in kinetic energy (Energy loss, eV). The first and more intense feature in the spectrum is the *zero loss peak* (ZLP), at 0 eV energy loss (Fig. 5.7A). This peak represents the electrons that have no energy loss (elastic scattering). The full width half-maximum (FWHM) of the ZLP (i.e. the difference between the two extremes values of the independent variable, at which the dependent variable is equal to half of its maximum value) gives the overall resolution of the spectrum (Brydson 2001).

The first region after any edge threshold is called ELNES (Energy Loss Near Edge Structure) (30-40 eV), which gives information on the local structure and bonding (geometrical information). Afterwards, a second region known as EXELFS (Extended Energy Loss Fine Structure) informs about bond distances and coordination number (short-range information) (Fig. 5.7B).

For ELNES and ELXEFs studies it is necessary to achieve high energy resolution (measured in the FWHM) and a good signal-to-noise ratio (SNR). These two conditions can be achieved increasing the primary energy, with the drawback that it can induce beam damage. Working with biomaterials makes this a tricky issue, and it is necessary to find a balance between resolution and beam damage.

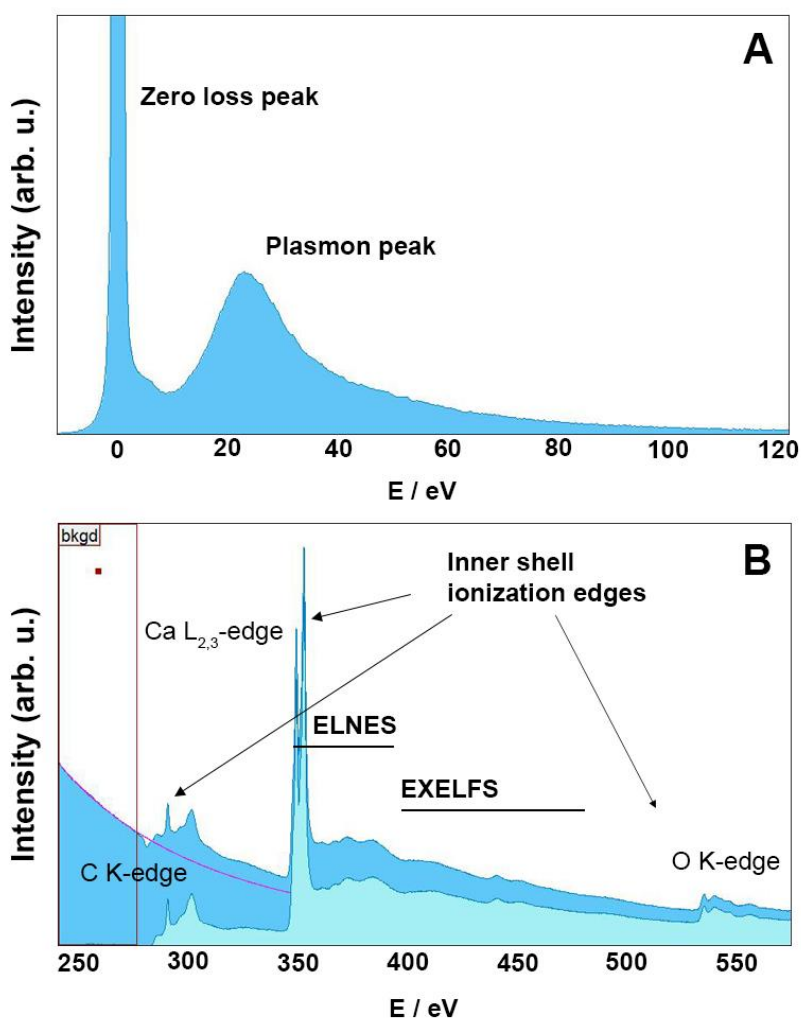


Fig. 5.7. The EEL spectrum. A) Low loss region. B) High loss region. The main areas of interest are indicated.

Through this PhD study, we have surveyed the *high loss region* of the spectra, from 0 to 750 eV (high dispersion), which contains the main ionization edges of the organic molecules (C, N, O, Mg, P and Ca). For the study of the mineral phase, we have focused on the ELNES fine structure of the main edges (carbon, calcium and oxygen).

5.7 Energy Dispersive X-ray Spectroscopy (EDS)

The accelerated electrons of the beam can interact with the electrons of the atoms of the sample causing one electron from an inner shell to be ejected. This creates an energetic *hole* or vacancy in its original shell, which is subsequently occupied by another electron from an outer (higher energy) shell. The energy difference between the shells will be liberated in the form of X-rays (Fig. 5.8A).

The number and energy of each atomic shell and subshells (the atomic structure) are characteristic of each element. Therefore the energy transferences, the amount of energy produced and the wavelength of the X-rays produced, are specific for each element. This constitutes the basis of the elemental determination.

The de-excitation process or relaxation to the ground state occurs in 1 ps approximately. The energy transfer occurs in sequential steps. The atom from the nearest subshell moves to fill the vacancy, leaving in turn a vacant state in its original shell, which will be filled by an electron from any other shell. Only transitions between certain subshells are allowed and produce characteristic X-rays.

But the primary electrons also produce a continuum X-ray spectrum that arises due to the interaction between the incident electrons with the nuclei (Fig. 5.8B). This continuous signal forms the background, and it depends on the beam current, the atomic Z number and the beam energy (Goldstein 2003). Nevertheless, compared with EELS, EDS presents a quite good signal to noise ratio, and although it is essential to subtract the background for quantification, the detection limits of the elements are relatively low. The smallest detectable peak should be at least three times the standard deviation of the background count.

Nevertheless, EDS is not as good as EELS for the detection of low Z elements. For these elements, the difference in energy between the subshells is rather low, which means that the lines of these elements overlap in the spectrum, it being impossible to separate them. With higher Z numbers, the difference in energy between subshells increases, thus making possible this differentiation.

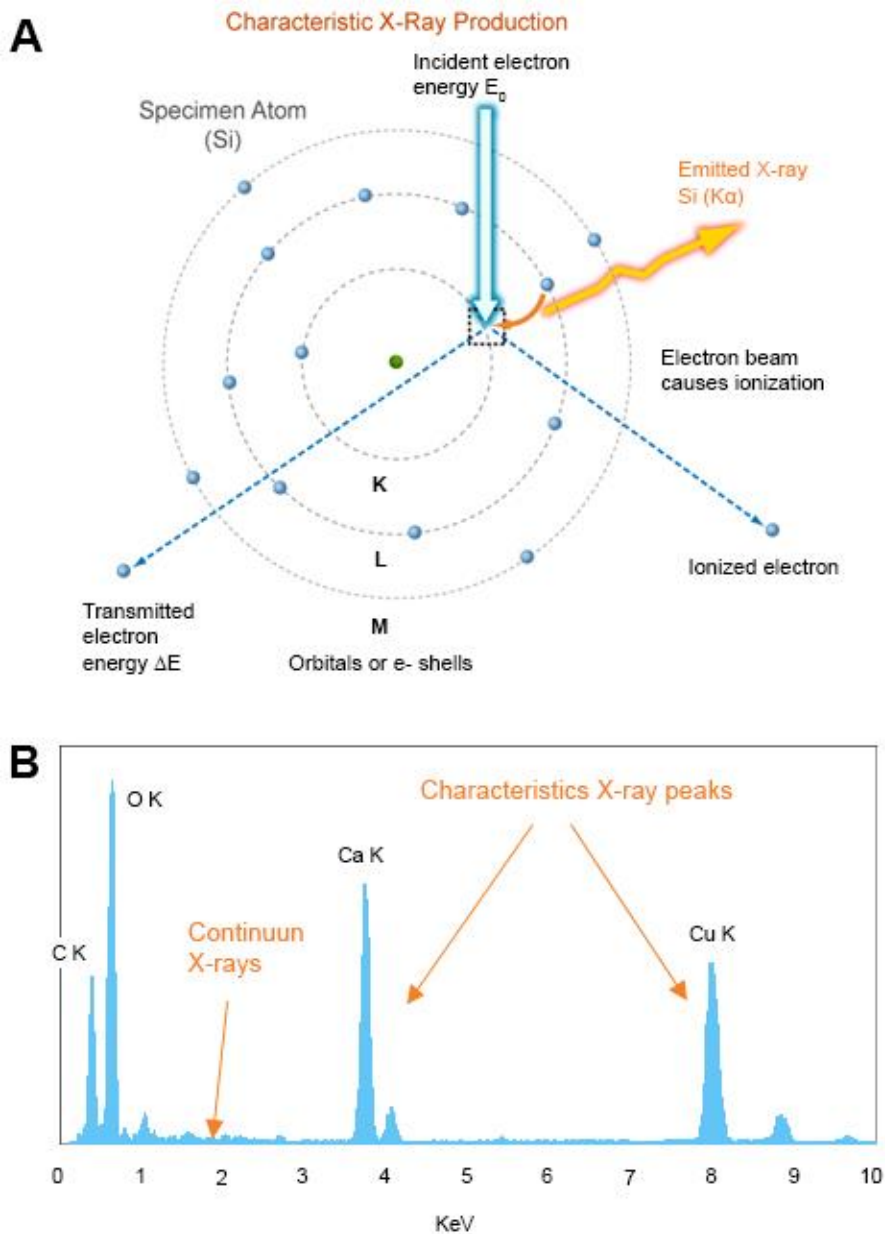


Fig. 5.8. EDS. A) De-excitation of an electron that has undergone a K-shell ionization by the primary electrons (image modified from Brydson *et al.* 2014). B) Characteristic EDS spectrum showing the continuum and the characteristic X-ray peaks.

Chapter 6

Results

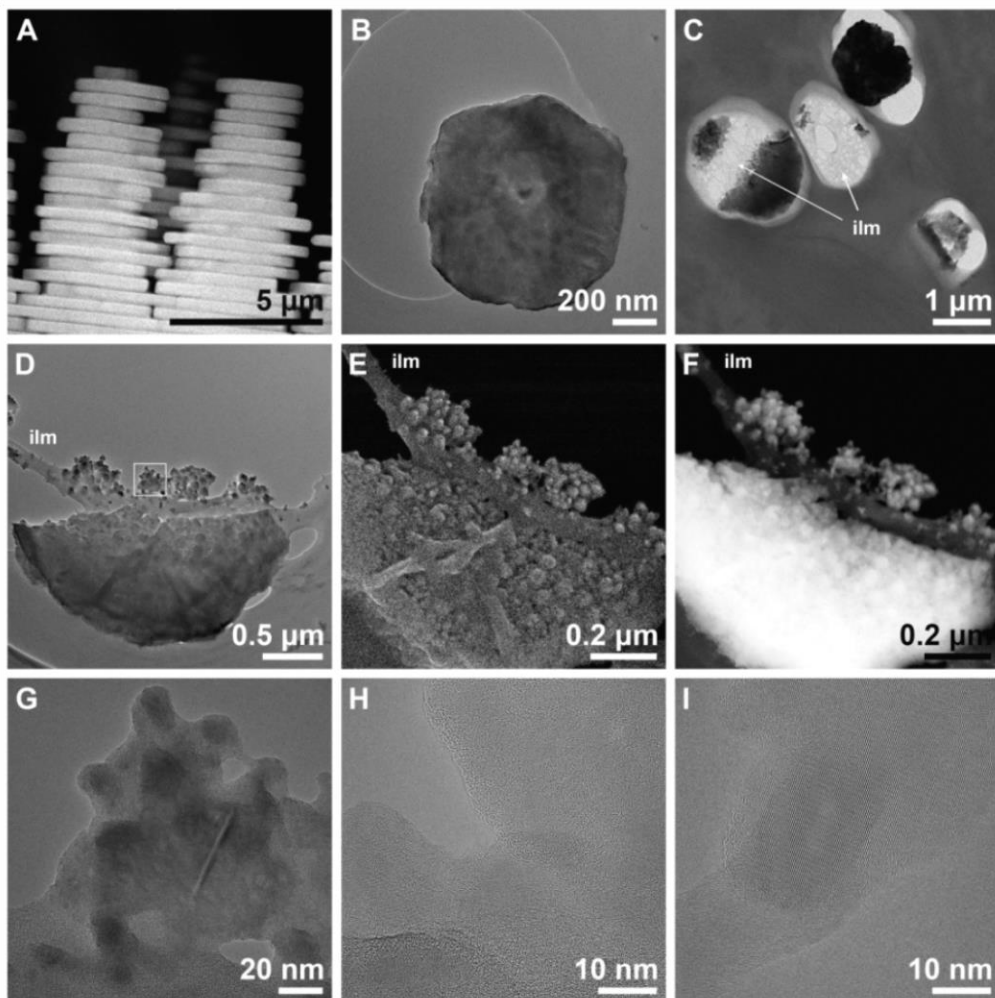
6.1 Amorphous calcium carbonate in nacre

6.1.1 Ultrastructure

Gastropod nacre tablets are stacked in towers (Wise and Hay 1968) (Fig. 6.1A), each tablet having a pseudo-hexagonal contour (Fig. 6.1B). Our oblique sections revealed the characteristic porous structure of the interlamellar membranes (Fig. 6.1C). Tablets consisted of an aggregation of globular particles measuring between 20-50 nm (Fig. 6.1D-F). The irregular topography became particularly evident with secondary electrons (SE) (Fig. 6.1E), whereas it remained masked in TEM (Fig. 6.1B-D). Similar nanoparticles were also found over the interlamellar membranes (ILMs) (Fig. 6.1D-F), and are likely the remains of hillocks cut during sample preparation. Hillocks, i.e. the protrusions (20-100 nm) of the tablet surface across the

pores of the ILM, maintain crystallographic coherence with the rest of the tablet (Checa *et al.* 2011). HRTEM highlights that the cores of these globular particles both from the tablet interior and/or the hillocks were crystalline nanodomains (average size 30 nm) embedded in an amorphous matrix (5-10 nm in thickness; Fig. 6.1G-I). Some forming tablets also presented amorphous edges, which crystallized under the electron beam (as reported by Nassif *et al.* 2005). In other instances, edges were fully crystalline.

► **Fig. 6.1. Gastropod nacre tablets from macro- to nanoscale.** A) Lateral view of nacre towers (HAADF). B) Tablet at the top of a tower cut almost perpendicular to the growth axis of the tower, with its characteristic pseudo-hexagonal shape. C) Slightly oblique section of some tablets. The characteristic porous structure of the interlamellar membranes (ilm) is visible. D, E, F) Image contrast comparison of a single tablet in TEM (D), SE (E) and HAADF (F). The tablet is composed of a myriad of nanogranules. Note the three-dimensional appearance provided by the SE image (E) compared to the other two modes. G) HRTEM of the area framed in (D): the nanogranules are composed by crystalline domains embedded in amorphous material. H) Oval shaped crystalline nanodomains showing lattice fringes, with amorphous rims. I) Detail of one such crystalline domain embedded in amorphous matter.



6.1.2 ACC and crystalline nanodomains

The examination of nanoparticles spread over the ILMs using High Angle Annular Dark Field (HAADF) imaging allowed us to differentiate the amorphous coating from the organic (amorphous) background, which remained concealed in TEM. HAADF enhances the contrast between materials of different composition (different average atomic Z number) (Fig. 6.1F). For the same average Z, variations in contrast are due to density or thickness changes (Williams and Carter 2009). Accordingly, CaCO_3 nanoparticles showed an intense contrast (bright areas) with respect to the organic background (Fig. 6.2A). The highest contrast (Fig. 6.2B) corresponded to the crystalline core identifiable by lattice fringes (Fig. 6.2C). Cores were bordered by non-crystalline areas with intermediate contrast (Fig. 6.2B-D) that faded gradually towards the edges (Fig. 6.2C, D). EELS confirmed the same composition for both the crystalline cores and the amorphous rims (Fig. 6.2D).

Besides the sectioned hillocks, there were two other types of nanoparticles scattered over the organic amorphous material: type one, 2-5 nm in size (Fig. 6.2B, F), and type two, 10-20 nm (Fig. 6.2E). Both of these nanoparticles returned a calcium signal (Fig. 6.2E) and had a non-crystalline structure.

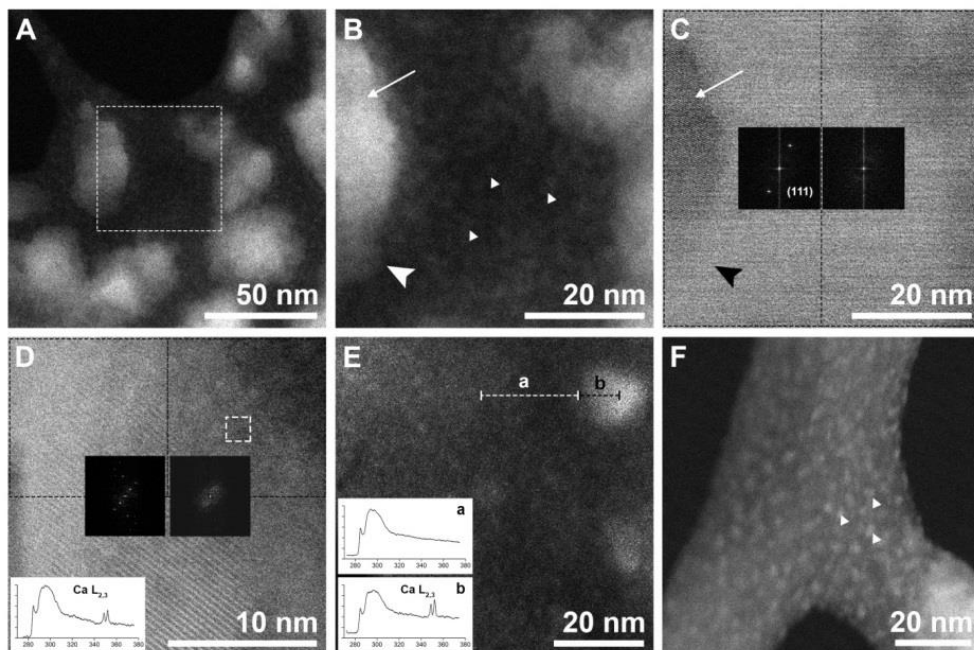


Fig. 6.2. Nanoparticle crystallinity and composition. A) Crystalline nanoparticles (rest of the tablet and/or hillocks) over the interlamellar membrane (organic amorphous material) (HAADF). B) Closer view of the area framed in A. The highest contrast (brightest area) corresponds to the core of the particle (arrow). The contrast fades towards the lower edge of the same particle (large arrowhead). The nanoparticle to the right presents an intermediate contrast. Densely scattered type one nanoparticles (2-5 nm) (small arrowheads) with some contrast cover the organic amorphous material. C) Bright-field (BF) STEM image of B. The particle to the left has a crystalline core (arrow) (indicated by lattice fringes and reflections in the FFT analysis). Its lower part (big arrowhead) does not show lattice fringes. Dashed rectangles indicate the areas where the FFTs come from. D) Nanoparticle showing the crystalline area (lattice fringes and reflections) on the left and the surrounding amorphous material on the right (HAADF). Squares with dashed lines indicate the areas where the FFTs come from. The EELS spectrum on the bottom left comes from the amorphous area (white box). E) Line scan EELS performed across the organic membrane (dashed line a) and a type-two particle (dashed line b). Only the particle with high contrast (12 nm in size) presented an intense calcium signal (b) (background removed, deconvolved and normalized). F) Densely scattered type-one nanoparticles (2-5 nm) (small arrowheads) over the organic membrane.

6.1.3 Indexing of crystalline nanodomains

Indexing of crystalline nanodomains (30-50 nm) surrounded by amorphous matter of the tablet interior corroborated their aragonitic nature (error < 5%). No other polymorph was detected. FFT of the image covering several nanodomains in Fig. 6.3A returned short arcs instead of sharp points, which result from the addition of slightly misaligned reflections (Fig. 6.3B). By selecting the reflections of the misaligned planes from the FFT and inverting the FFT function, we located the source areas of these signals. In this way, it became evident that the reflections came from adjacent, slightly misaligned (1.7° and 1.9°) nanodomains (Fig. 6.3C). Remarkably, the nanodomains were not oval, but had highly irregular contours that connected with and even overlapped one another (Fig. 6.3D).

When the indexing could be made exactly along the [001] zone axis, we appreciated that the crystalline nanodomains (Fig. 6.3E) had their *c*-axes co-aligned, but they were slightly misaligned in the *a-b* plane (Fig. 6.3F). An example of hillocks adhering to ILMs is shown in Fig. 6.3D-F. Some nanodomains presented twin relationships (Fig. 6.3G-I).

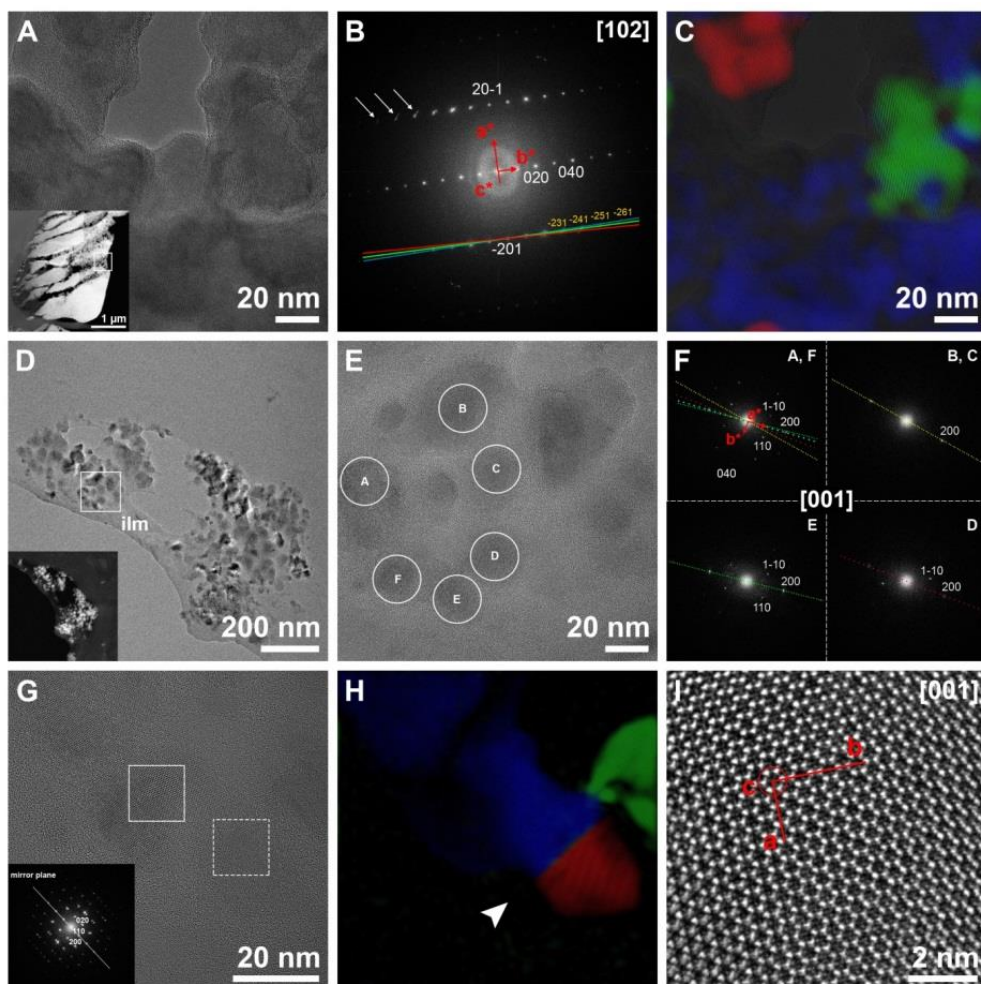


Fig. 6.3. Orientations of crystalline nanodomains. A) TEM image of crystalline nanodomains embedded in amorphous material. Inset: general view of the tablet with the location of the nanodomains. B) FFT analysis of A. The presence of small arcs in the FFT (arrows) indicates slight misalignment between nanodomains. Colours of lines indicate the reflections used for the colour reconstruction in C. C) RGB colour model built using the reflections corresponding to the planes $(\bar{2}31)$, $(\bar{2}41)$, $(\bar{2}51)$ and $(\bar{2}61)$ shown in B. Overlap of the original TEM image shows that crystallographically coherent nanodomains are separated by amorphous material. D) Incipient tablet showing crystalline nanodomains immersed in amorphous material. The position of the interlamellar membrane is indicated (ilm). Inset: HAADF of the same area. E) HRTEM of the area framed in D. Crystalline

nanodomains over the interlamellar membrane. F) FFT analysis of the nanodomains encircled in E (with the same letters). They are all indexed as aragonite along the [001] zone axis. The nanodomains are slightly tilted, which results in the attenuation or even disappearance of some reflections. In each FFT the *a*-axis is marked with a coloured dotted line. The overlap of all lines (upper left FFT) shows the misalignment of *a*-axes between nanodomains. G) HRTEM image of three different nanodomains over an organic membrane. Two of them show a twin relationship. Inset: FFT of the twin domain (area framed with dashed line). H) Colour reconstruction of the three different domains. A (110) twin plane (arrowhead), characteristic of aragonite, separates the blue and red nanodomains. The green nanodomain is in contact with the blue one with a misorientation of 5.8° around the *c*-axis. I) Enlargement of the area framed in G (solid line, blue nanodomain) indicating the crystallographic orientation. The view is from the *c*-axis.

6.1.4 Nanogranularity

We performed both AFM and S/TEM on single tablets (Fig. 6.4), with both revealing the globular texture typical of nacre (Dauphin 2001, Rousseau *et al.* 2005, Checa *et al.* 2013), and other biominerals (Baronnet *et al.* 2008, Dauphin 2008). AFM phase contrast images (which enable the detection of variations in adhesion, friction and viscoelasticity (Magonov *et al.* 1997) revealed two different materials (Fig. 6.4D): one with more adhesive strength (low contrast), previously assumed to be either organic material (Dauphin 2001, Rousseau *et al.* 2005), or a mixture of organics and ACC (Seto *et al.* 2012), and a second, stiffer material, assumed to be the crystalline phase by the same authors. The topographic images showed that the low-contrast layer extended over the stiffer material in the form of discontinuous pellicles (with variable thicknesses, between 2-10 nm, $n = 10$).

Observation of exactly the same areas by S/TEM (Fig. 6.4A-C) provided complementary information. The topographic contrast generated by SE in STEM is basically surface-tilt contrast: SEs created on an inclined surface or close to a surface step have an increased probability of escaping, thus producing a higher brightness/contrast (Reimer 1998). The irregularities observed with SEs (Fig. 6.4E) were less pronounced in the AFM images, but they correlated well with the topographic profiles, that revealed a very irregular surface. The overlap of both the SE and the low-contrast phase of the AFM images (Fig. 6.4F) showed that the distribution of the latter coincided relatively well with the flat (low-contrast, dark grey) areas observed in SE images.

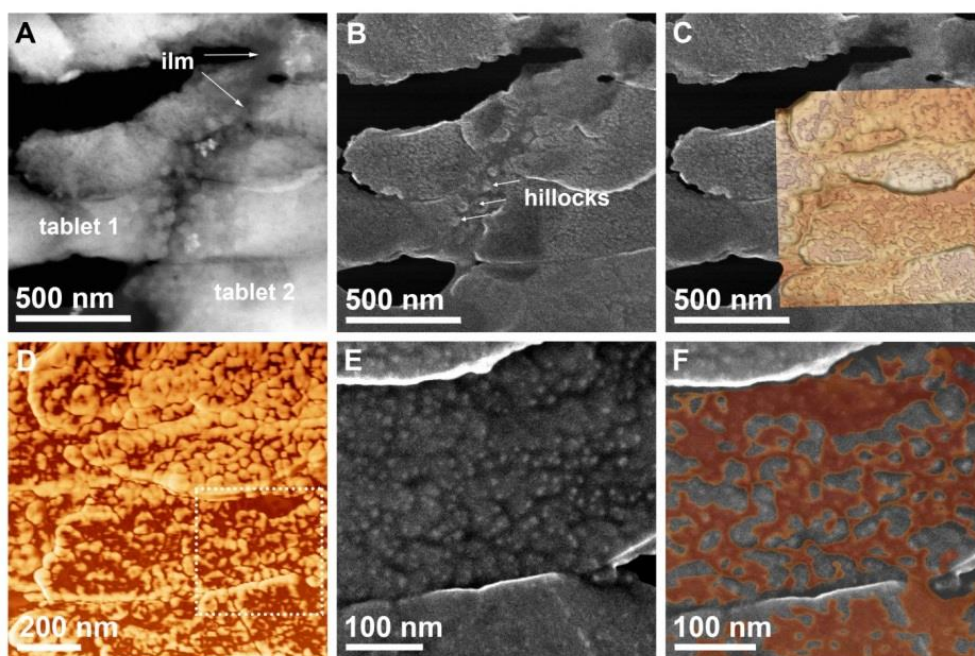


Fig.6.4. SE and AFM analysis of the same area. A) HAADF image of two tablets and the intermediate interlamellar membrane (ilm) (darker material). B) SE image of the same area. The smoothest area corresponds to the interlamellar membrane and some hillocks are visible

at the boundary between the two tablets. C) SE image with partially superposed AFM image (topographic + phase mode). D) AFM phase image emphasizing the globular aspect of the structure. The more adhesive material (dark-brown areas) overlies the crystals (light-brown areas). E) SE image of the area framed in D. The white dots are particularly steep areas, whereas darker areas tend to be horizontal. F) Overlap of the high-contrast areas of the AFM phase (brown) and SE (dark grey) images.

6.1.5 Tomography

The STEM-HAADF tomography revealed the high porosity of the forming tablet (Fig. 6.5, arrows). The three-dimensional reconstruction of the tomograms disclosed intriguing pyramid-like elevated areas. These pyramids were co-oriented and their tips corresponded to higher-contrast areas (more calcium content or denser material).

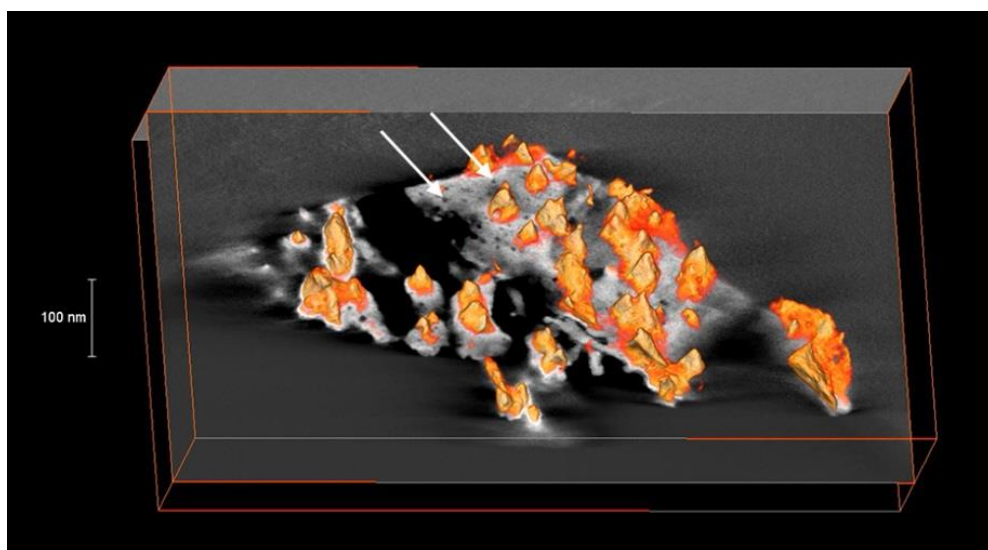


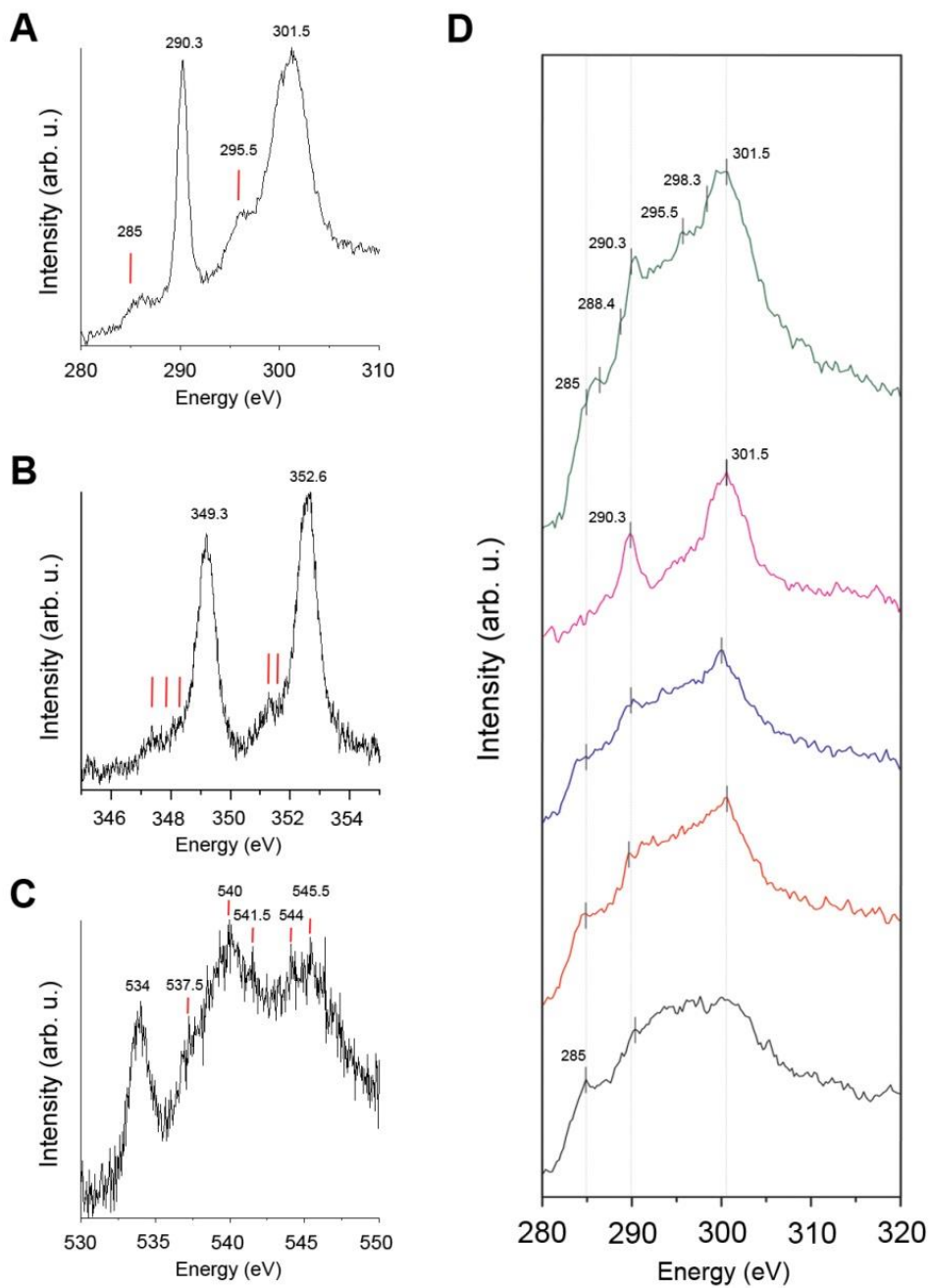
Fig. 6.5. Tomography of incipient nacre tablets. This selected tomographic slice has a multitude of pores (arrows). The colour gradient corresponds with the HAADF contrast, the tips of the pyramids (light orange) being the areas with higher contrast.

6.1.6 Elemental analysis

EELS performed in crystalline and amorphous domains revealed differences in chemical bonding (Fig. 6.6). The C K-edge ELNES structure showed two main peaks at 290.3 eV and 301.5 eV (Fig. 6.6A) that are unambiguously indicative of the carbonate group (Hofer *et al.* 1987, Garvie *et al.* 1994, Brandes *et al.* 2010). The peak at 290.3 eV corresponds to $C1s \rightarrow \pi^*$ transitions, whereas the peak at 301.5 eV arises from $C1s \rightarrow \sigma^*$ transitions of carbon-oxygen bonds of carbonate CO_3^{2-} groups (Garvie *et al.* 1994, Zhou *et al.* 2008). An unambiguous assignment to either $C - O$ or $C = O$ is not possible here (Zhou *et al.* 2008). Minor features related to π^* transitions of carbon-oxygen bonds, 294.2 and 298.3 eV (Zhou *et al.* 2008), were identified in only some spectra, with the former shifted to higher energies (295.5 eV) (Fig. 6.6A, Fig. 6.7A).

Three pre-peaks at 285.0 (± 0.3), 287.5 (± 0.3) and 288.4 (± 0.3) eV (Fig. 6.7A), with different relative intensities depending on the sampled area, were identified. The 285.0 and 287.5 eV peaks arise from $C1s \rightarrow \pi^*$ in $C=C$ and from $C1s \rightarrow \sigma^*$ in $C-H$ in organic molecules, respectively (Kaznachev *et al.* 2002, Metzler *et al.* 2008). The 288.4 eV peak results from $C1s \rightarrow \pi^*$ in $C=O$ of carboxyl groups of organic molecules (Zhou *et al.* 2008, Kaznachev *et al.* 2002, Zubavichus *et al.* 2005).

The calcium $L_{2,3}$ -edge ELNES is characterized by two main peaks at 349.3 and 352.6 eV (Fig. 6.6B), common to all $CaCO_3$ polymorphs. Three minor features present before L_3 and two before L_2 , indicate an aragonite nature (DeVol *et al.* 2015).



The oxygen-K ELNES in the crystalline areas presented a main peak at 534 (Fig. 6.6C) that results from $O1s \rightarrow \pi^*$ transitions from the C=O bonds (Metzler *et al.* 2008, DeVol *et al.* 2014), followed by a shoulder at 537.5 eV. Two double features are defined at 540/541 eV, associated with the $O1s \rightarrow \sigma^*$ transitions of the carbonate CO_3^{2-} group (Metzler *et al.* 2008) and at 544/545.5 eV, corresponding to $O1s \rightarrow \sigma^*$ transitions from the C=O absorptions (DeVol *et al.* 2014).

In the transition to the amorphous areas the three edges presented a progressive reduction in the intensity of the peaks. The peaks from the C K-edge graded to a single broad shoulder (Fig. 6.6D) characteristic of amorphous carbon. The Ca $L_{2,3}$ -edge diminished drastically in intensity, and the O K-edge lost any fine structure and showed only a broad resonance.

◀ **Fig. 6.6. EEL Spectroscopy from incipient nacre.** A) The C K-edge shows two prominent peaks at 290.3 and 301.5 eV, indicating high crystallinity, but a weak hump at 285 eV that reflects the presence of organic material. B) Ca $L_{2,3}$ -edge. C) O K-edge. For A, B and C, background was removed before each edge. The spectra are normalized and the intensity is expressed in arbitrary units (arb. u.) for comparison. No smoothing was applied. D) The line scan shows changes in the C K-edge along a segment of 143.7 nm. A total of 25 spectra were taken (each 5.75 nm, dispersion 0.25 eV) and averaged (5 single spectra added) to reduce the noise. Background was removed before the C K-edge, and the plural scattering was corrected. No smoothing was applied.

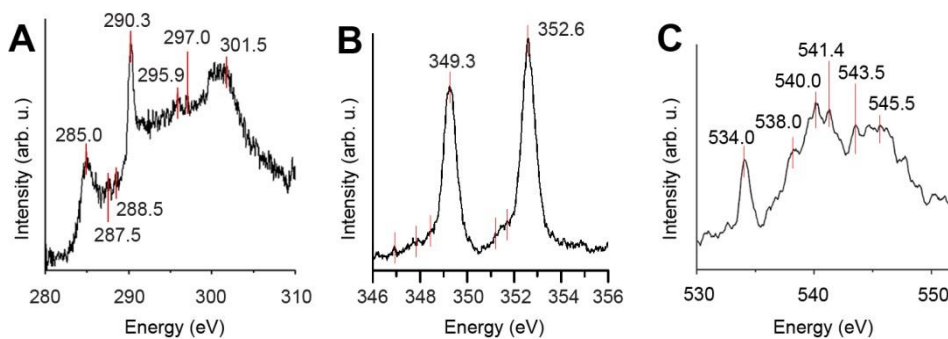


Fig. 6.7. EEL Spectroscopy. A) Carbon K-edge. The three pre-peaks at 285.0, 287.5, and 288.5 eV, characteristic of organic material, are visible. B) Calcium L_{2,3}-edge. The minor features that indicate the aragonite nature are marked with red bars. C) Oxygen K-edge characteristic of aragonite. All the peak positions denoted by vertical lines are commented on Table S1. Emission current 5 μ A, dispersion 0.025 eV. Savitzky-Golay smoothing was applied to the C K-edge (10 pts) and to the O K-edge (50 pts).

6.2 Elongation and alignment of nanogranules and their relation with the crystallography

Mutvei and Dunca (2008, 2010) evidenced the existence of parallel lineations on the surface of nacre tablets. These lineations appeared after etching the surface of the tablets with glutaraldehyde-acetic acid solution (Mutvei's solution) and are the result of differential dissolution of the carbonate. The direction of the lineations was inferred to be parallel to the crystallographic a -axes of the tablet (Mutvei and Dunca 2008).

We applied etching or proteinase treatments to nacreous tablets of different species. All samples (with the exception of *Pinna nobilis*) displayed conspicuous lineations (~40–120 nm thickness) after treatment (Fig. 6.8). Gastropods tablets appeared divided in different sectors (Fig. 6.8A) (Mutvei 1978) with the lineations meeting at angles of $\sim 60^\circ$ or 120° . *Nautilus* and bivalve tablets were mostly undivided. It is clearly shown that the lineations are composed of fused carbonate nanogranules (Fig. 6.8B).

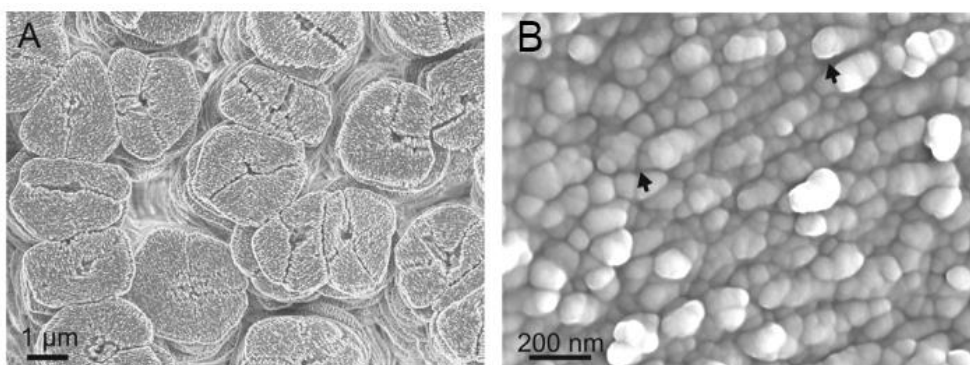


Fig. 6.8. A). *Gibbula cineraria*, treated with Mutvei's protocol (step 1 for 10 min, step 2 for 5 min). Tablets are composed of several sectors with lineations at 120° . B) *Nautilus pompilius*, bleached for 3 min. The two arrows indicate the ends of one such lineation.

To gain insight into the crystallography, we performed EBSD analysis to the etched tablets. In all pole figures, the 001 maxima (c -axis) was centred (perpendicular to the tablet) and the 100 maxima (a -axis) was parallel to the lineations.

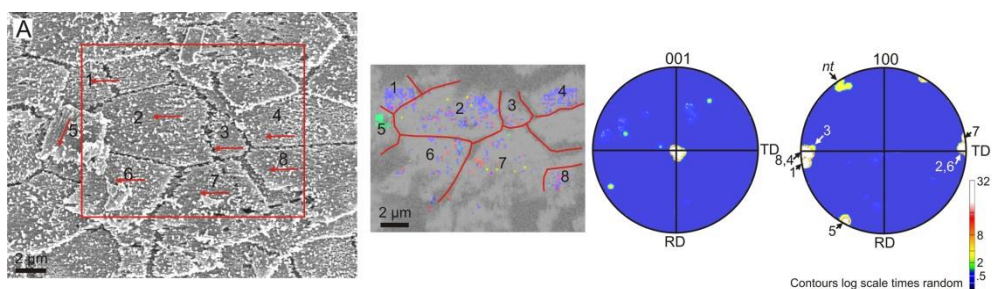


Fig. 6.9. EBSD maps of (A) *Acila divaricata*, treated with Mutvei's protocol (step 1 for 4 min, step 2 for 2 min).

AFM performed on samples either untreated or treated with protease (0.2 g/ml, 1h) showed that tablets were composed of nanogranules of sizes similar to those measured by SEM (~20–120 nm), surrounded by a pellicle of different contrast (Dauphin 2001, 2008). These granules often form lineations (40–120 nm) in a very similar way to the lineations observed by SEM.

6.3 Vesicles and surface membrane in nacreous gastropods

We have studied the surface membrane (SM) and the associated vesicle layer in *Phorcus turbinatus* (Trochidae, Vetigastropoda). The growth of the nacreous layer takes place close to the margin at the shell aperture (Wise 1970, Mutvei 1978). It is preceded by a fibrous prismatic layer and covered internally by an aragonitic structure of nacreous aspect (Fig. 6.10).

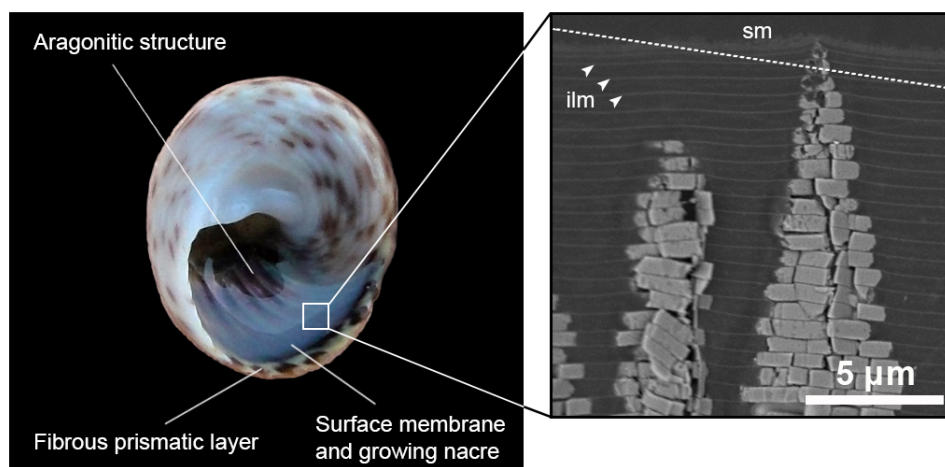


Fig. 6.10. Left, specimen of *Phorcus turbinatus* indicating the location of the surface membrane and the growing nacre (sampled area) in relation to the other microstructures present at the shell aperture. Right, SEM image of an ultramicrotome slice perpendicular to the shell surface, where it is possible to distinguish the surface membrane (sm), the interlamellar membranes (ilm) and two towers of growing nacre. The dotted line indicates the approximate angle of the ultramicrotome cuts carried out in this study.

The SM maintains a constant thickness due to the strict balance between components acquired via vesicle addition and those lost due to the formation of the interlamellar membranes (ILMs) (Checa *et al.* 2009). Therefore, we

can say it is in a *dynamic equilibrium*. At the same time, with the incorporation of material and its concomitant loss, the SM moves in an adaptural direction, by keeping pace with the animal's growth rate.

6.3.1 Ultrastructure

Low magnification TEM images show a general view of the system (Fig. 6.11A, B). A myriad of vesicles adhere to the mantle side. The SM with a fuzzy aspect lies over the tip of the towers. Note that the slides are oblique with respect to the growing axis of the nacre towers (Fig. 6.10), and therefore the thickness of the ILMs is overestimated.

The vesicle layer contains mostly round vesicles, with an average size ~200 nm (from 50 to 400 nm) (Fig. 6.11C). A double membrane (10-15 nm) was easily distinguishable (Fig. 6.11D). Electron-dense material seems to fill the interior of the vesicles, attached to the inner membrane (Fig. 6.11C, Fig. 6.12B, E).

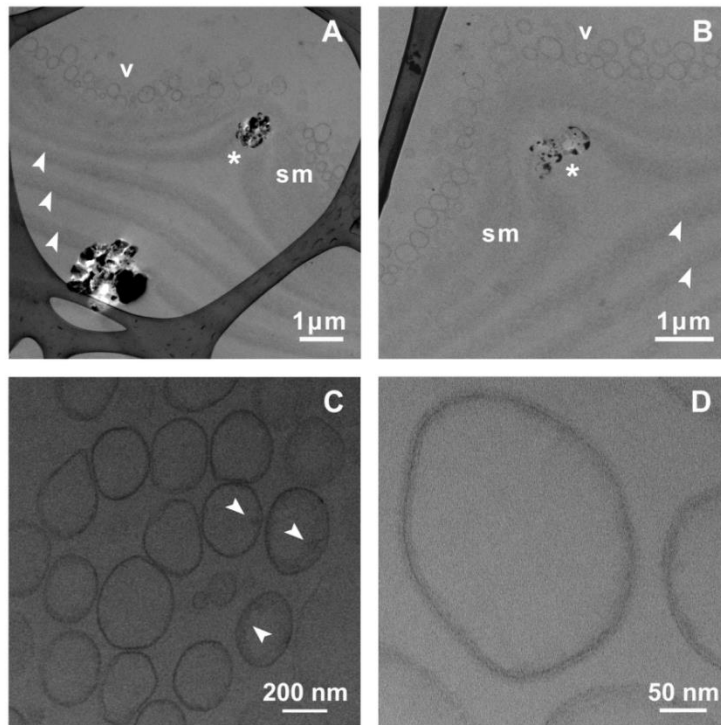


Fig. 6.11. Bright field TEM images of the vesicle layer. A) and B) vesicle layer (v) covering the surface membrane (sm). The tips of the first towers (marked with an asterisk) are partly immersed within the surface membrane. Interlamellar membranes (arrowheads) detach from it. C) Detail of the vesicles showing the material attached to the inner membrane (arrowheads). D) Closer view showing the double membrane. Samples fixed with glutaraldehyde 2.5% and post-fixed with 1% osmium tetroxide.

The SM (~100 nm width) appears as a progressively ordered structure. It has a dense homogeneous structure at the mantle side that organizes progressively into a fibrous arrangement at the nacre side. The most incipient crystals of the towers appear towards the interior, and the ILMs seem to detach from the SM (Fig. 6.12B).

6.3.2 Elemental analysis

The samples prepared by quick-freezing and freeze-drying preserved the cell structures relatively well. It was possible to localize the areas of interest (SM and vesicle layer), although some movements of the sub-cellular components might have occurred. The maintenance of the ion content was expected to be relatively good, since the water contact was minimized. Microanalysis was carried out on ~50-70 nm thickness sections.

Systematic EELS measurements were performed on quick-frozen and freeze-dried samples, either with or without OsO₄ as post-fixative. Signal intensity was higher in samples where osmium tetroxide was used. EDS analysis corroborated the data obtained by EELS. The structures studied in the outer side of the mineralization compartment were: the vesicles (interior (v) and membrane (mv)), the surface membrane (sm) and the epoxy resin (light areas, la). In the inner side of the mineralization compartment, we analysed the interlamellar membranes (ilm), the electrodense material (em) aggregates spread between the ILMs and the epoxy resin (light areas, la). A representative single raw spectrum of each analysed area is presented in Fig. 6.12H and Fig. 6.13B. No smoothness was applied.

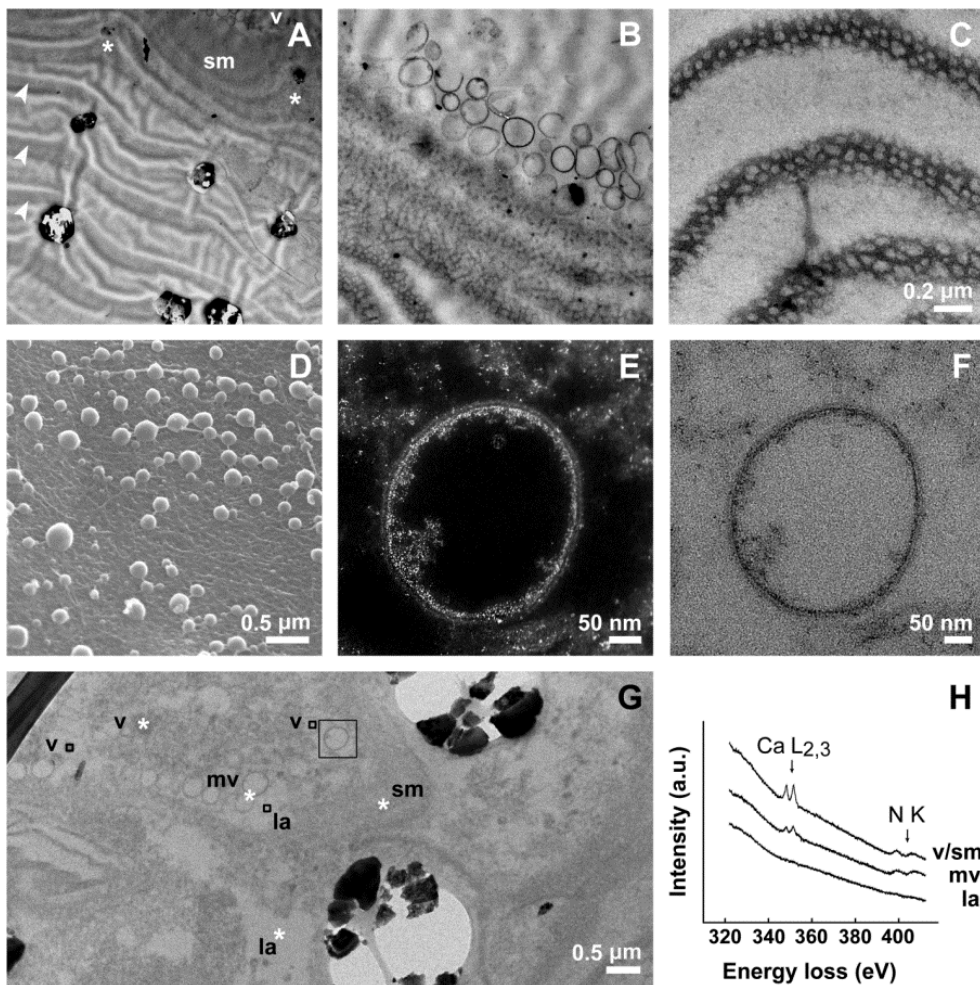


Fig. 6.12. Surface membrane and vesicle layer of *Phorcus turbinatus*. A) General view in STEM mode (inverse HAADF) including the vesicles (v), the surface membrane (sm), the first towers immersed in the surface membrane (asterisks) and the interlamellar membranes (arrowheads). B) Inverse HAADF image of the vesicle layer, the surface membrane and the interlamellar membranes detaching from it. C) Bright field imaging mode of mature interlamellar membranes with the porous aspect typical of gastropods. Section post-stained with uranyl acetate and lead citrate. D) SEM image of the vesicles covering the exterior of the surface membrane. E) HAADF image of a vesicle showing the material attached to its inner membrane. F) Same vesicle as in E) but in bright field mode. G) Bright field image of the vesicle layer and the surface membrane in an area close to the nacre towers, showing the

vesicles (v), the membranes of the vesicles (mv), the surface membrane (sm) and the light areas (la) of the epoxy resin. One spectrum was recorded in each point labelled. The vesicle shown in E) and F) is marked with a square. H) Core-loss spectra from the areas marked with an asterisk in G), showing Ca L_{2,3} and N K-edges. Single raw spectra, no smoothness was applied. Intensity is expressed in arbitrary units (a.u.) for comparison. A) and B) samples fixed with glutaraldehyde 2.5% and postfixed with 1% osmium tetroxide. C), E), F), G) samples quick-frozen and freeze-dried. D) Critical point dried sample.

At the outer side of the mineralization compartment (Fig. 6.12), EELS measurements revealed strong carbon K-edge at 285 eV, indicating poorly ordered carbon, owing to the epoxy resin used. The nitrogen K-edge at 400 eV and the oxygen K-edge at 532 eV were evident in all the measurements. A strong Ca L_{2,3}-edge (~348 eV) was detected in the SM (sm) and in the interior of the vesicles (v). The membrane of the vesicles reported a minor intensity of the Ca L_{2,3}-edge and an undetectable calcium signal was obtained from the epoxy (la) (Fig. 6.12G, H).

At the inner side of the mineralization compartment (Fig. 6.13), EELS spectra from the interlamellar membranes (ilm) revealed the K-edges of carbon (285 eV), nitrogen (400 eV) and oxygen (532 eV), as well as the L_{2,3}-edge of calcium (348 eV). The spectra obtained from the electrodeposited material (em) spread in the spaces between the ILMs showed the same peaks, though less intense. In the lighter areas (la) between ILMs, we observed the K-edges of carbon, nitrogen and oxygen that correspond to the embedding resin, and a negligible signal from the Ca L_{2,3}-edge.

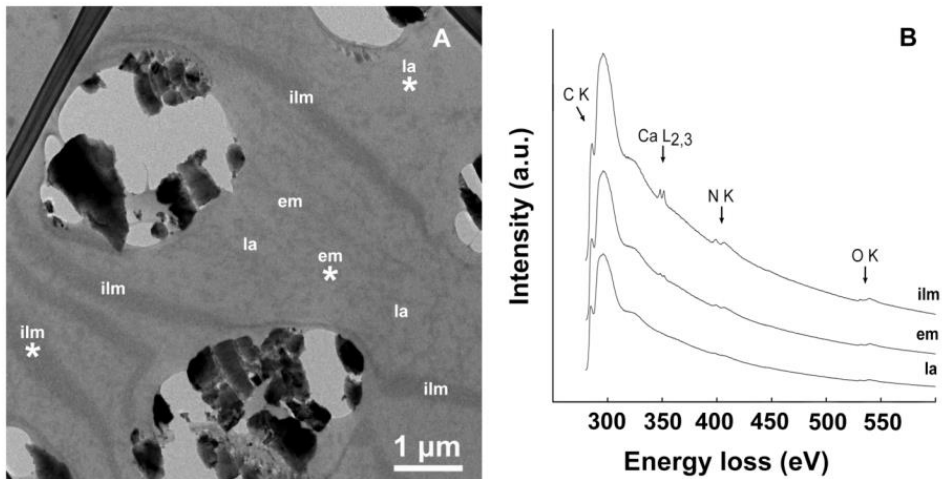


Fig. 6.13. A) TEM image of the mineralization compartment. It is possible to discern the stacked tablets (in diagonal section), the interlamellar membranes (ilm), the electrodense material (em) in between and the light areas (la) in the epoxy. One spectrum was recorded in each point labelled. B) Core loss spectra recorded at 200 keV from the areas marked with an asterisk in A (average pixel area 105 nm²), showing C K, Ca L_{2,3}, N K and O K-edges. Single raw spectra, no smoothness were applied. Intensity is expressed in arbitrary units (a.u.) for comparison. Quick-frozen and freeze-dried sample, postfixed in osmium tetroxide and embedded in EMBED 812.

Chapter 7

Discussion

7.1 Amorphous calcium carbonate in nacre

To gain insight into the formation of the mature nacre through an amorphous transient phase, we selected incipient tablets of subadult gastropods. Our TEM study demonstrated that the tablets are composed by globules with a partially crystalline structure: a crystalline core (~30 nm) and an amorphous contour (~5-10 nm).

Indexing of adjacent crystalline nanodomains connected by amorphous material showed a minor misorientation (in the range of 2°). In particular, the *c*-axes showed the highest degree of co-alignment. The quantification of the misalignment of the *c*-axis in mature nacre tablets of *Mytilus edulis* with low acceleration voltage electron backscatter diffraction (EBSD) gave a mean

angular spread in the order of 2° FWHM inside individual tablets (Griesshaber *et al.* 2013), in agreement with our present results. The colour reconstruction of the nanodomain orientation (Fig. 3C) clearly showed that the sectional outlines of the crystalline nanodomains are not simply spherical or oval, but complex dendritic. The fact that separate digitiform domains were in exactly the same orientation indicates that they must connect in the third dimension.

We also characterized the amorphous rims of nanoparticles by HAADF imaging. The lack of lattice fringes and the recorded calcium content indicate that it is ACC. The lower contrast with respect to the crystalline core is likely to be due to its lower density. The density of ACC ($\rho_{\text{ACC}} = 1.62 \text{ g}\cdot\text{cm}^{-3}$) (Bolze *et al.* 2002) is significantly lower than that of the crystalline phase ($\rho_{\text{aragonite}} = 2.93 \text{ g}\cdot\text{cm}^{-3}$).

The EELS analysis showed three pre-peaks at the C K-edge (285.0, 287.5 and 288.5 eV) that appeared in both crystalline and amorphous material and are undoubtedly related to the presence of organic matter. Chitin and lipids can contribute to these peaks (Lehmann 2009, Leung 2011), but their low content in the organic fraction of nacre ($\sim 7\%$ chitin, Bezares *et al.* 2008; 0.54 % lipids, Rousseau *et al.* 2006) leads us to believe that mostly proteins are responsible for these signals. In the O K-edge, the weak intensity of the 534 eV peak indicate poor crystallinity (DeVol *et al.* 2014).

The phase with more adhesion strength found by AFM, which surrounds and partially covers the crystalline phase, should correspond to the amorphous material (ACC + organic matter) imaged by TEM/STEM. This phase has been suggested to be either organic (Dauphin 2001, Rousseau *et al.* 2005) or a mixture of organic macromolecules and ACC (Seto *et al.* 2012),

but without conclusive evidence. Both our HRTEM and the ELNES analyses of the amorphous phase in incipient nacre tablets indicate that the latter is the case. The presence of biogenic macromolecules occluded within the ACC stabilizes it against dissolution or rapid crystallization (Aizenberg *et al.* 1997, Addadi *et al.* 2003, Gal *et al.* 2014). Different kinds of additives have been identified as stabilizers, with amino acids being among the molecules that permanently stabilize ACC (Addadi *et al.* 2003). Proteins have been demonstrated to inhibit ACC·H₂O dehydration, allowing the persistence of ACC·H₂O-rich nanoparticles (Gong *et al.* 2012).

Our data are consistent with a particle-accretion mechanism in nacre. This mechanism has been intensely studied in the spicule of the sea urchin embryo (Politi *et al.* 2008, Gong *et al.* 2012) and implies that amorphous particles aggregate and subsequently crystallize. The two types of ACC nanoparticles detected on the ILMs (type one, 2-5 nm, and type two, 10-20 nm) are in the size range of the aggregation units described in synthetic systems (Gebauer *et al.* 2008, Pouget *et al.* 2009) and it is likely that they are the first ACC intermediates.

In nacre, the continuity of the mineral bridges from one tablet to next (Checa *et al.* 2009) would allow the propagation of the crystal lattice. A neat crystallization front is absent. Conversely, we have observed complex, dendritic fronts that in 3D should branch off throughout the interior of the material. Transformation from amorphous to crystalline would happen concomitantly along this large-surface crystalline-amorphous interface. Concomitant transformation at different sites was implied by Addadi *et al.* (2003) to occur also in the sea urchin larval spicule.

As the tablets mature and ACC crystallizes, some of the organic macromolecules may be occluded within the crystal lattice, while others would be expelled by the crystallization force. This process might not be isotropic, but the expulsion can be favoured along particular crystallographic directions (see next section). The accumulation might “poison” the crystallization process (Aizenberg *et al.* 1996) and permanently stabilize the residual organic-rich ACC, which would accumulate around crystalline globules (Seto *et al.* 2012). These would remain as pellicles around crystalline globules (commonly observed in low contrast under AFM phase mode).

The dendritic shape that we found indicate that the nanogranular structure observed in crystalline nacre might be the result of the crystallization process. Hence, the sizes of the nanoglobules do not necessarily represent the sizes of the aggregation particles, as some authors have suggested (Gal *et al.* 2014).

7.2 Elongation and alignment of nanogranules

Most of the nacre tablets studied showed fused calcium carbonate granules (lineations) aligned along the *a*-axis of the tablet. The nanogranules presented surrounding pellicules of a few nanometres that show high contrast in AFM phase images.

We propose that these lineations are the result of differential absorption of organic molecules along the crystallographic axes. In the aragonite structure, the strongest bonds are along the *a*-axis, because the distances between the Ca atoms and the CO₃²⁻ groups are the shortest. These strong spatial constraints would cause the expulsion of the organic molecules by the

crystallization force along the *a*-axis, which would accumulate sideways. Along the *b*-axis the distances between the calcium atoms and the carbonate groups are longer, what would enable the incorporation of organic material along this axis. In the *c*-axis, the CO₃²⁻ groups are stacked and bonded by weak Van der Waals forces (Nelyubina and Lyssenko 2012) which would allow the incorporation of organic molecules (producing a horizontal nanolamination of the tablet along this axis).

7.3 Vesicles and surface membrane in nacreous gastropods

By means of transmission electron microscopy we were able to locate and image the layer of vesicles located over the surface membrane (SM) of nacreous gastropods. Vesicles present double-layered membrane (Fig. 6.11D) that resembles a phospholipid bilayer. The thickness in our samples (10-15 nm) is overestimated due to the oblique cut of the ultramicrotome slides (thickness of the lipid bilayer is 4–5 nm). The material contained in the vesicles is often attached to the inner surface of the vesicle membrane (Fig. 6.11C, Fig. 6.12E, F).

The surface membrane seems to undergo maturation and becomes increasingly better defined and organized in depth (Fig. 6.12B). The typical porous aspect of gastropod ILMs (Fig. 6.12C) is fully achieved on the nacre side where ILMs detach from the SM. Proteins, polysaccharides (chitin) and lipids might suffer an assembly and polymerization processes to produce the final structure of the ILMs.

Elemental analysis revealed the presence of calcium in different areas of the system: inside the vesicles, within the SM and ILMs and in the particles scattered between the ILMs. In the SM and ILM it seems obvious that calcium should be bound to organic molecules. Inside the vesicles and in the particles scattered in between ILMs, the signal always come from electrodense material (calcium was never detected in the epoxy). In our samples, the contrast of the organic material is enhanced due to the osmium tetroxide fixation, which binds to double bounds of lipids and some proteins. OsO₄ cross-links and stabilizes proteins, avoiding their loss in subsequent steps of sample preparation (i.e. dehydration) (Hayat 2000). Therefore, it is likely that the detected calcium is bound to proteins and/or lipids.

This result does not preclude the existence of ionic calcium and/or ACC. We expected that at least some of the vesicles transport ACC. The double membrane vesicles and the distribution of the material attached to the inner surface are congruent with what has been found in other systems. In the mouse calvaria, mineral bearing vesicles transport membrane-bound ACP granules (Mahamid *et al.* 2011). In magnetotactic bacteria, the first nucleation proceeds on the inner surface of the membrane (Komeili *et al.* 2004). It seems probable that the phospholipid bilayer has a stabilization function of the disordered phase. In this case, the release of the content could trigger the crystallization process (Weiner and Addadi 2011).

We were not able to detect ACC, likely due to sample preparation. Cryo-techniques are required to preserve the ion content and the mineral phase. Unfortunately we had not access to these techniques during this PhD study, and it will be part of future research.

Conclusions

- The ultrastructure of the forming nacre tablets consists of an aggregation of globular particles measuring between 20–50 nm. The cores of these globular particles are crystalline nanodomains (average size 30 nm) embedded in amorphous matrix (5–10 nm in thickness).
- Crystalline nanodomains are highly co-oriented, with a misorientation of $\sim 2^\circ$. When it was possible to index the nanodomains along the [001] zone axis, the misorientation occurred in the a - b plane.
- Crystalline nanodomains have highly irregular contours that connect and overlap with one another, forming a complex crystallization front.
- The amorphous material that surrounds the crystalline cores is composed by a mixture of organic macromolecules, most likely proteins, and amorphous calcium carbonate. The high concentration of calcium in these areas and the amorphous structure indicates an ACC nature.
- These amorphous areas correspond with the low contrast areas imaged by AFM, which show more adhesive strength (called pellicles or nanomembranes). It was inferred to be organic by some authors and a mixture of macromolecules and ACC by others. Our data indicate that the latter is the case.

-
- Our data are consistent with a particle accretion mechanism for the formation of nacre, and do not support previous models based on the formation of misoriented nanodomains and their subsequent alignment by the so called *oriented attachment* mechanism.
 - The parallel lineations at the surface of the nacre tablets are composed by aggregations of calcium carbonate nanogranules, clearly visible after etching. Lineations invariably align with the *a*-axis of the tablet. We propose that these lineations are the result of differential absorption of organic molecules along the crystallographic axes of aragonite.
 - The nanogranularity observed at the surface of nacre tablets may not reflect the size of the aggregation units, but might be the result of the subsequent crystallization process.
 - The vesicles which fuse and integrate into the surface membrane of gastropods show a double, presumably lipidic, membrane. The vesicle content is attached to the vesicle inner membrane.
 - The surface membrane undergoes a structural modification from the outer to the inner side, showing a characteristic porous structure when the interlamellar membranes detach from it.
 - The presence of calcium was confirmed in the vesicle membrane and within the vesicle, as well as within the surface and interlamellar membranes.

Conclusiones

- La ultraestructura de las tabletas de nácar en formación consiste en una agregación de partículas globulares que miden entre 20–50 nm. Los núcleos de estas partículas globulares son nanodominios cristalinos (tamaño medio 30 nm) embebidos en una matriz amorfa (5–10 nm de espesor).
- Los nanodominios cristalinos están altamente co-orientados, con una misorientación de $\sim 2^\circ$. Cuando ha sido posible indexar los nanodominios a lo largo del eje de zona [001], la misorientación fue identificada dentro del plano $a-b$.
- Los nanodominios cristalinos tienen contornos altamente irregulares, y conectan y se solapan unos con otros, formando un frente de cristalización complejo.
- El material amorfo que rodea los núcleos cristalinos está compuesto por una mezcla de macromoléculas orgánicas, probablemente proteínas, y carbonato cálcico amorfo. La alta concentración de calcio en estas áreas y su estructura amorfa indican una composición de carbonato cálcico amorfo.
- Estas áreas amorfas se corresponden con las áreas de bajo contraste observadas mediante AFM, y que muestran mayores fuerzas adhesivas

(denominadas películas o nanomembranas). Hasta ahora unos autores lo habían identificado como material orgánico y otros como una mezcla de macromoléculas orgánicas y ACC. Nuestros datos son congruentes con el último caso.

- Nuestros datos son consecuentes con un mecanismo de agregación de partículas para la formación del nácar, y difiere de modelos previos basados en la formación de nanodominios misorientados y su alineamiento posterior mediante el mecanismo denominado de unión o agregación orientada (*oriented attachment*).
- Las lineaciones paralelas de la superficie de las tabletas de nácar están compuestas por una agregación de gránulos de carbonato cálcico, claramente visibles tras ataque químico. Las lineaciones están invariablemente alineadas a lo largo de los ejes *a* de las tabletas. Proponemos que estas alineaciones son el resultado de una absorción diferencial de moléculas orgánicas a lo largo de los ejes cristalinos del aragonito.
- La nanogranularidad observada en la superficie de las tabletas de nácar no tiene porqué reflejar el tamaño de las unidades de agregación, sino que podrían resultar del proceso de cristalización posterior.
- Las vesículas que fusionan y se integran en la membrana superficial de gasterópodos muestran una doble membrana, presumiblemente lipídica. El contenido de las vesículas se encuentra unido a la membrana interna de las vesículas.

- La membrana superficial sufre una modificación en su estructura desde su lado externo al interno, en que se hace visible una estructura porosa característica.
- La presencia de calcio ha sido confirmada en el contenido de las vesículas y en la membrana de las mismas, así como en las membranas interlamelares y en la membrana superficial.

References

- Abbe E. 1873. Beitrage zur Theorie des Mikroskops and der mikroskopischen Wahrnehmung *Arch. mikrosk. Anat. Entw. Mech.* **9**, 413. See also: Abbe E. 1904. *Gesamm. Abh.* **1**, 45.
- Addadi L, Raz S, Weiner S. 2003. Taking advantage of disorder: amorphous calcium carbonate and its roles in biomineralization. *Adv. Mater.* **15**, 959 – 970.
- Aizenberg J, Lambert G, Addadi L, Weiner S. 1996. Stabilization of amorphous calcium carbonate by specialized macromolecules in biological and synthetic precipitates. *Adv. Mater.* **8**, 222 – 226.
- Aizenberg J, Hanson J, Koetzle TF, Weiner S, Addadi L. 1997. Control of macromolecule distribution within synthetic and biogenic single calcite crystals. *J. Am. Chem. Soc.* **119**, 881 – 886.
- Aizenberg J, Muller DA, Grazul JL, Hamann DR. 2003. Direct fabrication of large micropatterned single crystals. *Science* **299**, 1205 – 1208.
- Anderson HC. 1995. Molecular biology of matrix vesicles. *Clin. Orthop. Rel. Res.* **314**, 266 – 280.
- Anderson HC. 2003. Matrix vesicles and calcification. *Cur. Rheumatol. Rep.* **5**, 222 – 226.
- Anon P. 2006. Golay's global view. *Pearl World: Int. Pearling J.* **15**, 7 – 8.
- Atlan G, Balmain N, Berland S, Vidal B, Lopez E. 1997. Reconstruction of human maxillary defects with nacre powder: histological evidence for bone regeneration. *C. R. Acad. Sci. Paris, Life. Sci.* **320**, 253 – 258.
- Banfield JF, Welch SA, Zhang H, Thomsen Ebert T, Penn RL. 2000. Aggregation-based crystal growth and microstructure development in natural iron oxyhydroxide biomineralization products. *Science* **289**, 751 – 754.
- Baronnet A, Cuif JP, Dauphin Y, Farre B, Nouet J. 2008. Crystallization of biogenic Ca-carbonate within organo-mineral micro-domains. Structure of the calcite prisms of the Pelecypod *Pinctada margaritifera* (Mollusca) at the submicron to nanometre ranges. *Mineral. Mag.* **72**, 617 – 626.
- Barthelat F, Li C-M, Comi C, Espinosa HD. 2006. Mechanical properties of nacre constituents and their impact on mechanical performance. *J. Mater. Res.* **21**, 1977 – 1986.

- Bengtson S. 1994. The advent of animal skeletons. In: Bengtson S (Ed). Early Life on Earth. Nobel Symposium 84. Columbia University Press, New York, pp 421 – 425.
- Beniash E, Aizenberg J, Addadi L, Weiner S. 1997. Amorphous calcium carbonate transforms into calcite during sea urchin larval spicule growth. *Proc. R. Soc. Lond. B* **264**, 461 – 465.
- Beniash E, Addadi L, Weiner S. 1999. Cellular control over spicule formation in sea urchin embryos: a structural approach. *J. Struct. Biol.* **125**, 50 – 62.
- Beniash E, Metzler RA, Lam RS, Gilbert PUPA. 2009. Transient amorphous calcium phosphate in forming enamel. *J. Struct. Biol.* **166**, 133 – 43.
- Bentov S, Brownlee C, Erez J. 2009. The role of seawater endocytosis in the biomineralization process in calcareous foraminifera. *Proc. Natl. Acad. Sci. USA* **106**, 21500 – 21504.
- Bergström L, Sturm (née Rosseeva) EV, Salazar-Alvarez G, Cölfen H. 2015. Mesocrystals in biominerals and colloidal arrays. *Acc. Chem. Res.* **48**, 1391 – 1402.
- Berman A, Hanson J, Leiserowitz L, Koetzle TF, Weiner S, Addadi L. 1993. Biological control of crystal texture: a widespread strategy for adapting crystal properties to function. *Science* **259**, 776 – 779.
- Bevelander G, Nakahara H. 1969. An electron microscope study of the formation of the nacreous layer in the shell of certain bivalve molluscs. *Calcif. Tissue Res.* **3**, 84 – 92.
- Bezares J, Asaro RJ, Hawley M. 2008. Macromolecular structure of the organic framework of nacre in *Haliotis rufescens*: implications for growth and mechanical behavior. *J. Struct. Biol.* **163**, 61 – 75.
- Bolze J, Peng B, Dingenouts N, Panine P, Narayanan T, Ballauff M. 2002. Formation and growth of amorphous colloidal CaCO₃ precursor particles as detected by time-resolved SAXS. *Langmuir* **18**, 8364 – 8369.
- Boudias C, Monceau D. 1989. CaRIne Crystallography 3.1.
- Brandes JA, Wirrick S, Jacobsen C. 2010. Carbon K-edge spectra of carbonate minerals. *J. Synchrotron Rad.* **17**, 676 – 682.
- Brigham EO. 1974. The Fast Fourier Transform and its applications. Prentice-Hall, New Jersey.
- Brydson R. 1991. Electron Energy Loss Spectroscopy. Taylor and Francis, Oxford.
- Burton WK, Carbrera N, Frank FC. 1951. The growth of crystals and the equilibrium structure of their surfaces. *Phil. Trans. R. Soc. A* **243**, 299 – 358.
- Camprasse S, Camprasse G, Pouzol M, Lopez E. 1990. Artificial dental root made of natural calcium carbonate (bioracine). *Clin. Mater.* **5**, 235 – 250.
- Carter CB, Norton MG. 2007. Ceramic materials. Springer Science-Business Media, New York.
- Cartwright JHE, Checa AG. 2007. The dynamics of nacre self-assembly. *J. R. Soc. Interface* **4**, 491 – 504.
- Caspi EN, Pokroy B, Lee PL, Quintana JP, Zolotoyabko E. 2005. *Acta Cryst. B* **61**, 129 – 132.
- Cavalier-Smith T. 2004. Only six kingdoms of life. *Proc. R. Soc. Lond. B* **271**, 1251 – 1262.

- Chave KE. 1954. Aspects of the biogeochemistry of magnesium I. Calcareous marine organisms. *J. Geology* **62**, 266 – 283.
- Checa AG, Cartwright JHE, Willinger MG. 2009. The key role of the surface membrane in why gastropod nacre grows in towers. *Proc. Natl. Acad. Sci. USA* **106**, 38 – 43.
- Checa AG, Cartwright JHE, Willinger MG. 2011. Mineral bridges in nacre. *J. Struct. Biol.* **176**, 330 – 339.
- Checa AG, Mutvei H, Osuna-Mascaró AJ, Bonarski JT, Faryna M, Berent K, Pina CM, Rousseau M, Macías-Sánchez E. 2013. Crystallographic control on the substructure of nacre tablets. *J. Struct. Biol.* **183**, 368 – 376.
- Cölfen H, Mann S. 2003. Higher-order organization by mesoscale self-assembly and transformation of hybrid nanostructures. *Angew. Chem. Int. Ed. Engl.* **42**, 2350 – 2365.
- Cölfen H, Antonietti M. 2005. Mesocrystals: inorganic superstructures made by highly parallel crystallization and controlled alignment. *Angew. Chem. Int. Ed.* **44**, 5576 – 5591.
- Coty WA, McConkey CL. 1982. A high-affinity calcium-stimulated ATPase activity in the hen oviduct shell gland. *Arch. Biochem. Biophys.* **219**, 444 – 453.
- Crane NJ, Popescu V, Morris MD, Steenhuis P, Ignelzi MA. 2006. Raman spectroscopic evidence for octacalcium phosphate and other mineral species deposited during intramembraneous mineralization. *Bone* **39**, 434 – 442.
- Crenshaw MA. 1972. The inorganic composition of molluscan extrapallial fluid. *Biol. Bull.* **143**, 506 – 512.
- Cuif JP, Dauphin Y. 2005. The two-step mode of growth in the scleractinian coral skeletons from the micrometre to the overall scale. *J. Struct. Biol.* **150**, 319 – 331.
- Currey JD. 1990. Biomechanics of mineralized skeletons. In: Carter JG (Ed). *Skeletal biomineralization: patterns, processes and evolutionary trends*, Vol. 1. Van Nostrand Reinhold, New York, pp 11 – 25.
- Dalbeck P, England J, Cusack M, Lee MR, Fallick AE. 2006. Crystallography and chemistry of the calcium carbonate polymorph switch in *M. edulis* shells. *Eur. J. Mineral.* **18**, 601 – 609.
- Dauphin Y. 2001. Nanostructures de la nacre des tests de céphalopodes actuels. *Paläontologische Zeitschrift* **75**, 113 – 122.
- Dauphin Y. 2008. The nanostructural unity of mollusc shells. *Mineral. Mag.* **72**, 243 – 246.
- Dauphin Y, Dufour E. 2008. Nanostructures of the aragonitic otolith of cod (*Gadus morhua*). *Micron* **39**, 891 – 896.
- Decker GL, Morrill JB, Lennarz WJ. 1987. Characterization of sea urchin primary mesenchyme cells and spicules during biomineralization in vitro. *Development* **101**, 297 – 312.
- Decker GL, Lennarz WJ. 1988. Skeletogenesis in the sea urchin embryo. *Development* **103**, 231 – 247.
- Demichelis R, Raiteri P, Gale JD, Quigley D, Gebauer D. 2011. Stable prenucleation mineral clusters are liquid-like ionic polymers. *N. Comms.* **2**, 590.

- DeVol RT, Metzler RA, Kabalah-Amitai L, Pokroy B, Politi Y, Gal A, Addadi L, Weiner S, Fernández-Martínez A, Demichelis R, Gale JD, Ihli J, Meldrum FC, Blonsky AZ, Killian CE, Salling CB, Young AT, Marcus MA, Scholl A, Doran A, Jenkins C, Bechtel HA, Gilbert PUPA. 2014. Oxygen spectroscopy and polarization-dependent imaging contrast (PIC) - mapping of calcium carbonate minerals and biominerals. *J. Phys. Chem. B* **118**, 8449 – 8457.
- DeVol RT, Sun C-Y, Marcus MA, Coppersmith SN, Myneni SCB, Gilbert PUPA. 2015. Nanoscale transforming mineral phases in fresh nacre. *J. Am. Chem. Soc.* **137**, 13325 – 13333.
- Dillaman R, Hequembourg S, Gay M. 2005. Early pattern of calcification in the dorsal carapace of the blue crab, *Callinectes sapidus*. *J. Morphology* **263**, 356 – 374.
- Egerton RF. 2011. Electron Energy-Loss Spectroscopy in the electron microscope. Springer, New York.
- Ehrenberg CG. 1834. Phosphosaures kalk in den zähnen und kieselerde in dem panzer von infusorein. *Ann. Phys. Lpz.* **32**, 574 – 576.
- England J, Cusack M, Dalbeck P, Pérez-Huerta A. 2007. Comparison of the crystallographic structure of semi nacre and nacre by Electron Backscatter Diffraction. *Cryst. Growth Des.* **7**, 307 – 310.
- Forsen S, Kordel J. 1994. Calcium in biological systems. In: Bertini I, Gray HB, Lippard SJ, Valentine JS (Eds). Bioinorganic chemistry. University Science Books, Mill Valley, California, pp 107 – 166.
- Frýda J, Klicnarová M, Frýdová B, Mergl M. 2010. Variability in the crystallographic texture of bivalve nacre. *Bull. Geosci.* **85**, 645 – 662.
- Gal A, Hirsch A, Siegel S, Li C, Aichmayer B, Politi Y, Fratzl P, Weiner S, Addadi L. 2012. Plant cystoliths: a complex functional biocomposite of four distinct silica and amorphous calcium carbonate phases. *Chem. Eur. J.* **18**, 10262 – 10270.
- Gal A, Habraken W, Gur D, Fratzl P, Weiner S, Addadi L. 2013. Calcite crystal growth by a solid-state transformation of stabilized amorphous calcium carbonate nanospheres in a hydrogel. *Angew. Chem. Int. Ed.* **52**, 4867 – 4870.
- Gal A, Kahil K, Vidavsky N, DeVol RT, Gilbert PUPA, Fratzl P, Weiner S, Addadi L. 2014. Particle accretion mechanism underlies biological crystal growth from an amorphous precursor phase. *Adv. Funct. Mater.* **24**, 5420 – 5426.
- Galwey AK. 2000. Structure and order in thermal dehydrations of crystalline solids. *Thermochim. Acta* **355**, 181 – 238.
- Garvie LAJ, Craven A, Brydson R. 1994. Use of electron-energy loss near-edge fine structure in the study of minerals. *Am. Min.* **79**, 411 – 425.
- Garvie LAJ. 2010. Can electron energy-loss spectroscopy (EELS) be used to quantify hydrogen in minerals from the O K edge? *Am. Miner.* **95**, 92 – 97.
- Gebauer D, Völkel A, Cölfen H. 2008. Stable prenucleation calcium carbonate clusters. *Science* **322**, 1819 – 1822.
- Gilbert PUPA, Metzler RA, Zhou D, Scholl A, Doran A, Young A, Kunz M, Tamura N, Coppersmith SN. 2008. Gradual ordering in red abalone nacre. *J. Am. Chem. Soc.* **130**, 17519 – 17527.

- Glimcher MJ. 1984. Recent studies of the mineral phase in bone and its possible linkage to the organic matrix by protein-bound phosphate bonds. *Phil. Trans. Roy. Soc. B*, **B304**, 479 – 508.
- Goffinet G, Jeuniaux C. 1979. Distribution et importance quantitative de u chitine dans les coquilles de mollusques. *Cah. Biol. Mar.* **20**, 341 – 349.
- Goffredo S, Vergni P, Reggi M, Caroselli E, Sparla F, Levy O, Dubinsky Z, Falini G. 2011. The skeletal organic matrix from Mediterranean coral *Balanophyllia europaea* influences calcium carbonate precipitation. *PLoS ONE* **6**, e22338.
- Goldstein J, Newbury D, Joy D, Lyman C, Echlin P, Lifshin E, Sawyer L, Michael J. 2003. Scanning Electron Microscopy and X-Ray Microanalysis. Kluwer Academic/Plenum Publishers, New York.
- Gong Y, Killian CE, Olson IC, Appathurai NP, Amasino AL, Martin MC, Holt LJ, Wilt FH, Gilbert PUPA. 2012. Phase transitions in biogenic amorphous calcium carbonate. *Proc. Natl. Acad. Sci. USA* **109**, 6088 – 6093.
- Grégoire C, Duchâteau G, Florin M. 1955. La trame protidique des nacres et des perles. *Ann. Inst. Ocean.* **31**, 1 – 36.
- Grégoire C. 1962. On submicroscopic structure of *Nautilus* shell. *Bull. Inst. Roy. Sci. Nat. Belgique* **38**, 1 – 71.
- Gries K, Kröger R, Kübel C, Schowalter M, Fritz M, Rosenauer A. 2009. Correlation of the orientation of stacked aragonite platelets in nacre and their connection via mineral bridges. *Ultramicroscopy* **109**, 230 – 236.
- Griesshaber E, Schmahl WW, Ubhi HS, Huber J, Nindiyasari F, Maier B, Ziegler A. 2013. Homoepitaxial meso- and microscale crystal co-orientation and organic matrix network structure in *Mytilus edulis* nacre and calcite. *Acta Biomater.* **9**, 9492 – 9502.
- Grynopas MD, Bonar LC, Glimcher MJ. 1984. Failure to detect an amorphous calcium-phosphate solid phase in bone mineral: a radial distribution function study. *Calcif. Tiss. Int.* **36**, 291 – 301.
- Habraken WJEM, Tao J, Brylka LJ, Friedrich H, Bertinetti L, Schenk AS, Verch A, Dmitrovic V, Bomans PHH, Frederik PM, Laven J, van der Schoot P, Aichmayer B, de With G, DeYoreo JJ, Sommerdijk NAJM. 2013. Ion-association complexes unite classical and non-classical theories for the biomimetic nucleation of calcium phosphate. *N. Comms.* **4**, 1507.
- Hasse B, Ehrenberg H, Marxen JC, Becker W, Epple M. 2000. Calcium carbonate modifications in the mineralized shell of the freshwater snail *Biomphalaria glabrata*. *Chem. Eur. J.* **6**, 3679 – 3685.
- Hayat MA. 1981. Fixation for electron microscopy. Academic Press, New York.
- Hayat MA. 1993. Stains and cytochemical methods. Plenum Press, New Yoirk.
- Hayat MA. 2000. Principles and techniques of electron microscopy. Biological applications. Cambridge University Press, Cambridge.
- Hawkes PW. 1990. Ernst Ruska. *Physics Today* **43**, 84 – 85.
- Hofer F, Golob P. 1987. New examples for near-edge fine structures in electron energy loss spectroscopy. *Ultramicroscopy* **21**, 379 – 384.

- Horcas I, Fernández R, Gómez-Rodríguez JM, Colchero J, Gómez-Herrero J, Baro AM. 2007. *Rev. Sci. Instrum.* **78**, 013705.
- Ihli J, Wong WC, Noel EH, Kim YY, Kulak AN, Christenson HK, Duer MJ, Meldrum FC. 2014. Dehydration and crystallization of amorphous calcium carbonate in solution and in air *N. Comms.* **5**, 3169.
- Isa Y, Ikehara N, Yamazato K. 1980. Evidence for the occurrence of Ca⁺⁺-dependent adenosine triphosphatase in a hermatypic coral, *Acropora hebes* (Dana). *Sesoko mar. Sci. Lab. Tech. Rep.* **2**, 19 – 25.
- Jackson AP, Vincent JFV, Turner RM. 1988. The mechanical design of nacre. *Proc. R. Soc. B*, **234**, 415 – 440.
- Kaznachev K, Osanna A, Jacobsen C, Plashkevych O, Vahtras O, Ågren H, Carravetta V, Hitchcock AP. 2002. Innershell absorption spectroscopy of amino acids. *J. Phys. Chem. A* **106**, 3153 – 3168.
- Killian CE, Metzler RA, Gong YUT, Olson IC, Aizenberg J, Politi Y, Wilt FH, Scholl A, Young A, Doran A, Kunz M, Tamura N, Coppersmith SN, Gilbert PUPA. 2009. Mechanism of calcite co-orientation in the sea urchin tooth. *J. Am. Chem. Soc.* **131**, 18404 – 18409.
- Kim YY, Schenk AS, Ihli J, Kulak AN, Hetherington NBJ, Tang CC, Schmahl WW, Griesshaber E, Hyett G, Meldrum FC. 2014. A critical analysis of calcium carbonate mesocrystals. *N. Comms.* **5**, 4341.
- Kingsley RJ, Watabe N. 1984. Calcium uptake in the gorgonian *Leptogorgia virgulata*. The effects of ATPase inhibitors. *Comp. Biochem. Physiol.* **79**, 487 – 491.
- Klaveness D. 1976. *Emiliania huxleyi* (Lohmann) Hay and Mohler. III. Mineral deposition and the origin of the matrix during coccolith formation. *Protistologica* **12**, 217 – 224.
- Knoll AH. 2003. Biomineralization and evolutionary history. In: Dove PM, Weiner S, De Yoreo JJ (Eds). *Biomineralization. Reviews in Mineralogy and Geochemistry* 54. Mineralogical Society of America, Virginia, pp 329 – 356.
- Komeili A, Vali H, Beveridge TJ, Newman DK. 2004. Magnetosome vesicles are present before magnetite formation, and MamA is required for their activation *Proc. Natl. Acad. Sci. USA* **101**, 3839 – 3844.
- Kouchinsky A. 2000. Shell microstructures in Early Cambrian molluscs. *Acta Palaeontol. Pol.* **45**, 119 – 150.
- Le Roy N, Mariel B, Gaume E, Guichard N, Delgado S, Zanella-Cleon I, Becchi M, Auzoux-Bordenave E, Sire JY, Marin F. 2012. Identification of two carbonic anhydrases in the mantle of the european abalone *Haliotis tuberculata* (Gastropoda, Haliotidae): phylogenetic implications. *J. Exp. Zool. B (Mol Dev Evol)* **318**, 353 – 367.
- Lehmann J, Solomon D, Brandes J, Fleckenstein H, Jacobsen C, Thieme J. 2009. Synchrotron-based Near-Edge X-ray Spectroscopy of NOM in soils and sediments. In: Senesi N, Xing B, Huang PM (Eds). *Biophysico-chemical processes involving natural nonliving organic matter in environmental systems*. John Wiley and Sons, New Jersey, pp 729 – 782.

- Leung BO, Hitchcock AP, Won A, Ianoul A, Scholl A. 2011. Imaging interactions of cationic antimicrobial peptides with model lipid monolayers using X-ray spectromicroscopy. *Eur. Biophys. J.* **40**, 805 – 810.
- Li D, Nielsen MH, Lee JRI, Frandsen C, Banfield JF, De Yoreo JJ. 2012. Direction-specific interactions control crystal growth by oriented attachment. *Science* **336**, 1014 – 1018.
- Li X, Xu Z-H, Wang R. 2006. In situ observation of nanograin rotation and deformation in nacre. *Nano Lett.* **6**, 2310 – 2304.
- Lin AY-M, Chen P-Y, Meyers MA. 2008. The growth of nacre in the abalone shell. *Acta Biomaterialia* **4**, 131 – 138.
- Liu B, Tan C, Zhang D, Chen M, Niu Z, Huang G, Li Y, Zhang T Yu D. 2017. Genetic parameters of growth and resistance to *Polydora ciliata* in the pearl oyster *Pinctada fucata*. *Aquacult. Res.* **48**, 2039 – 2046.
- Lowenstam HA. 1962. Magnetite in denticle capping in recent chitons (Polyplacophora). *Geol. Soc. Am. Bull.* **73**, 435 – 438.
- Lowenstam HA, Weiner S. 1989. On Biomineralization. Oxford University Press, Oxford.
- Ma Y, Aichmayer B, Paris O, Fratzl P, Meibom A, Metzler RA, Politi Y, Addadi L, Gilbert PUPA, Weiner S. 2009. The grinding tip of the sea urchin tooth exhibits exquisite control over calcite crystal orientation and Mg distribution. *Proc. Natl. Acad. Sci. USA* **106**, 6048 – 6053.
- Magonov SN, Elings V, Whangbo M-H. 1997. Phase imaging and stiffness in tapping-mode atomic force microscopy. *Surf. Sci.* **375**, 385 – 91.
- Mahamid J, Sharir A, Addadi L, Weiner S. 2008. Amorphous calcium phosphate is a major component of the forming fin bones of zebrafish: indications for an amorphous precursor phase. *Proc. Natl. Acad. Sci. USA* **105**, 12748 – 12753.
- Mahamid J, Aichmayer B, Shimoni E, Ziblat R, Li C, Siegel S, Paris O, Fratzl P, Weiner S, Addadi L. 2010. Mapping amorphous calcium phosphate transformation into crystalline mineral from the cell to the bone in zebrafish fin rays. *Proc. Natl. Acad. Sci. USA* **107**, 6316 – 6321.
- Mahamid J, Sharir A, Gur D, Zelzer E, Addadi L, Weiner S. 2011. Bone mineralization proceeds through intracellular calcium phosphate loaded vesicles: a cryo-electron microscopy study. *J. Struct. Biol.* **174**, 527 – 535.
- Maitland T, Sitzman S. 2007. Backscattering detector and EBSD in nanomaterials characterization. In: Zhou W, Wang ZL (Eds). Scanning microscopy for nanotechnology. Springer – Verlag, New York, pp 41 – 75.
- Mann S. 2001. Biomineralization: principles and concepts in bioinorganic materials chemistry. Oxford University Press, New York.
- Marie B, Zanella-Cleon I, Le Roy N, Becchi M, Luquet G, Marin F. 2010. Proteomic analysis of the acid-soluble nacre matrix of the bivalve *Unio pictorum*: detection of novel carbonic anhydrase and putative protease inhibitor proteins. *Chem. Bio. Chem.* **11**, 2138 – 2147.
- Marxen J, Becker W, Finke D, Hasse B, Epple M. 2003. Early mineralization in *Biomphalaria glabrata*: microscopic and structural results. *J. Moll. Stud.* **69**, 113 – 121.

- Meibom A, Cuif JP, Hillion F, Constantz BR, Juillet-Leclerc A, Dauphin Y, Watanabe T, Dunbar RB. 2004. Distribution of magnesium in coral skeleton. *Geophys. Res. Lett.* **31**, L23306 – 23310.
- Metzler RA, Kim W, Delak K, Evans JS, Zhou D, Beniash E, Wilt FH, Abrecht M, Chiou J-W, Guo J, Coppersmith SN, Gilbert PUPA. 2008. Probing the organic-mineral interface at the molecular level in model biominerals. *Langmuir* **24**, 2680 – 2687.
- Minchin EA. 1909. Sponge-spicules. Summary of present knowledge. *Ergebn Fortschr Zoologie*, **2**, 171 – 274.
- Mitchell DRG. 2008. DiffTools: software tools for electron diffraction in Digital Micrograph. *Microsc. Res. Tech.* **71**, 588 – 593.
- Montessuit C, Caverzasio J, Bonjour JP. 1991. Characterization of a P_i transport system in cartilage matrix vesicles: potential role in the calcification process. *J. Biol. Chem.* **266**, 17791 – 17797.
- Mutvei H. 1972. Ultrastructural relationships between the prismatic and nacreous layers in *Nautilus* (Cephalopoda). *Biom mineralization* **4**, 81 – 86.
- Mutvei H. 1977. The nacreous layer in *Mytilus*, *Nucula* and *Unio* (Bivalvia). *Calcif. Tissue Res.* **24**, 11 – 18.
- Mutvei H. 1978. Ultrastructural characteristics of the nacre in some gastropods. *Zool. Scripta* **7**, 287 – 296.
- Mutvei H. 1979. On the internal structure of the nacreous tablets in molluscan shells. *Scanning Electron Microsc.* II 457 – 462.
- Mutvei H, Dunca E. 2008. Structural relationship between interlamellar organic sheets and nacreous tablets in gastropods and cephalopod *Nautilus*. *Paläontol. Z.* **82**, 85 – 94.
- Mutvei H, Dunca E. 2010. Crystalline structure, orientation and nucleation of the nacreous tablets in the cephalopod *Nautilus*. *Paläontol. Z.* **84**, 457 – 465.
- Nakahara H. 1979. An electron microscope study of the growing surface of nacre in two gastropod species, *Turbo cornutus* and *Tegula pfeifferi*. *Venus* **3**, 205 – 211.
- Nakahara H. 1991. Nacre formation in bivalve and gastropod molluscs. In: Suga S, Nakahara H (Eds). Mechanisms and phylogeny of mineralization in biological systems. Springer Verlag, Tokyo, pp 343 – 350.
- Nassif N, Pinna N, Gehrke N, Antonietti M, Jäger C, Cölfen H. 2005. Amorphous layer around aragonite platelets in nacre. *Proc. Natl. Acad. Sci. USA* **102**, 12653 – 12655.
- Navrotsky A. 2004. Energetic clues to pathways to biomineralization: precursors, clusters, and nanoparticles. *Proc. Natl. Acad. Sci. USA* **101**, 12096 – 12101.
- Nelyubina YV, Konstantin AL. 2012. From “loose” to “dense” crystalline phases of calcium carbonate through “repulsive” interactions: an experimental charge-density study. *Eur. Chem. J.* **18**, 12633 – 12636.
- Okazaki M, Fujii M, Usuda Y, Furuya K. 1984. Soluble Ca²⁺-activated ATPase and its possible role in calcification of the coccolithophorid *Cricosphaera roscoffensis* var. *haptonemofera* (Haptophyta). *Bot. Mar.* **27**, 363 – 369.
- Olson IC, Blonsky AZ, Tamura N, Kunz M, Pokroy B, Romao CP, White MA, Gilbert PUPA. 2013. Crystal nucleation and near-epitaxial growth in nacre. *J. Struct. Biol.* **184**, 454 – 463.

- Osuna-Mascaró AJ, Cruz-Bustos T, Marin F, Checa AG. 2015. Ultrastructure of the interlamellar membranes of the nacre of the bivalve *Pteria hirundo*, determined by immunolabelling. *PLoS ONE* **10**, e0122934.
- Penn RL, Banfield JF. 1999. Morphology development and crystal growth in nanocrystalline aggregates under hydrothermal conditions: insights from titania. *Geochim. Cosmochim. Acta* **63**, 1549 – 1557.
- Politi Y, Arad T, Klein E, Weiner S, Addadi L. 2004. Sea urchin spine calcite forms via a transient amorphous calcium carbonate phase. *Science* **306**, 1161 – 1164.
- Politi Y, Metzler RA, Abrecht M, Gilbert B, Wilt FH, Sagi I, Addadi L, Weiner S, Gilbert PUPA. 2008. Transformation mechanism of amorphous calcium carbonate into calcite in the sea urchin larval spicule. *Proc. Natl. Acad. Sci. USA* **105**, 17362 – 17366.
- Pouget EM, Bomans PHH, Goos JACM, Frederik PM, de With G, Sommerdijk NAJM. 2009. The initial stages of template-controlled CaCO₃ formation revealed by Cryo-TEM. *Science* **323**, 1455 – 1458.
- Putnis A, Putnis CV. 2007. The mechanism of reequilibration of solids in the presence of a fluid phase. *J. Solid State Chem.* **180**, 1783 – 1786.
- Reimer L. 1998. Scanning electron microscopy. Physics of image formation and microanalysis. Springer, Berlin.
- Rey L, May JC. 2010. Freeze drying/lyophilization of pharmaceutical and biological products. Informa Healthcare, London.
- Reynolds ES. 1963. The use of lead citrate at high pH as an electron opaque stain in electron microscopy. *J. Cell Biol.* **17**, 208 – 212.
- Rodríguez-Navarro C, Kudłacz K, Cizerc Ö, Ruiz-Agudo E. 2015. Formation of amorphous calcium carbonate and its transformation into mesostructured calcite. *Cryst. Eng. Comm.* **17**, 58 – 72.
- Rodríguez-Navarro C, Elert K, Ševčík R. 2016. Amorphous and crystalline calcium carbonate phases during carbonation of nanolimes: implications in heritage conservation. *Cryst. Eng. Comm.* **18**, 6594 – 6607.
- Rodríguez-Navarro C, Burgos-Cara A, Elert K, Putnis CV, Ruiz-Agudo E. 2016. Direct nanoscale imaging reveals the growth of calcite crystals via amorphous nanoparticles. *Cryst. Growth Des.* **16**, 1850 – 1860.
- Rohde M, Mayer H. 2007. Exocytotic process as a novel model for mineralization by osteoblasts in vitro and in vivo determined by electron microscopic analysis. *Calcif. Tissue Int.* **80**, 323 – 336.
- Rousseau M, Lopez E, Stempfélé P, Brendlé M, Franke L, Guetted A, Naslain R, Bourrat X. 2005. Multiscale structure of sheet nacre. *Biomaterials* **26**, 6254 – 6262.
- Rousseau M, Bédouet L, Lati E, Gasser P, Le Ny K, Lopez E. 2006. Restoration of stratum corneum with nacre lipids. *Comp. Biochem. Physiol. B* **145**, 1 – 9.
- Sarikaya M, Aksay IA. 1992. Nacre of abalone shell: a natural multifunctional nanolaminated ceramic-polymer composite material. In: Case ST (Ed). Structure, cellular synthesis and assembly of biopolymers. Springer-Verlag Berlin Heidelberg.
- Schäffer TE, Ionescu-Zanetti C, Proksch R, Fritz M, Walters DA, Almqvist N, Zaremba CM, Belcher AM, Smith BL, Stucky GD, Morse DE, Hansma PK. 1997. Does abalone

- nacre form by heteroepitaxial nucleation or by growth through mineral bridges? *Chem. Mater.* **9**, 1731 – 1740.
- Schmidt WJ. 1992. Über den Aufbau der Schale von *Nucula*. *Arch. Mikr. Anat.* **96**, 171 – 181.
- Schmidt WJ. 1923. Bau und Bildung der Perlmuttermasse. *Zool. Jahrb.* **45**, 1 – 148.
- Schmidt WJ. 1924. Die Bausteine des Tierkörpers in polarisiertem Lichte. Verlag F, Cohen. Bonn.
- Seo Y, Jhe W. 2008. Atomic force microscopy and spectroscopy. *Rep. Prong. Phys.* **71**, 016101.
- Seto J, Ma Y, Davis SA, Meldrum F, Gourrier A, Kim Y-Y, Schilde U, Sztucki M, Burghammer M, Maltsev S, Jäger C, Cölfen H. 2012. Structure-property relationships of a biological mesocrystal in the adult sea urchin spine. *Proc. Natl. Acad. Sci. USA* **109**, 3699 – 3704.
- Shen V, Kohler G, Peck WA. 1983. A high affinity, calmodulin- responsive (Ca^{2+} - Mg^{2+})-ATPase in isolated bone cells. *Biochim. Biophys. Acta* **727**, 230 – 238.
- Sone ED, Weiner S, Addadi L. 2007. Biomineralization of limpet teeth: a cryo-TEM study of the organic matrix and the onset of mineral deposition. *J. Struct. Biol.* **158**, 428 – 444.
- Stechschulte DJ, Morris DC, Silverton S, Anderson HC, Väänänen K. 1992. Presence and specific concentration of carbonic anhydrase II in matrix vesicles. *Bone and Mineral* **17**, 187 – 191.
- Swanson JA, Watts C. 1995. Macropinocytosis. *Trends Cell. Biol.* **5**, 424 – 428.
- Tai K, Ulm FJ, Ortiz C. 2006. Nanogranular origins of the strength of bone. *Nano Lett.* **6**, 2520 – 2525.
- Tashian RE. 1989. The carbonic anhydrases: widening perspectives on their evolution, expression and function. *BioEssays* **10**, 186 – 192.
- Thomas RDK, Shearman RM, Stewart GW. 2000. Evolutionary exploitation of design options by the first animals with hard skeletons. *Science* **288**, 1239 – 1242.
- Towe KM, Lowenstam HA. 1967. Ultrastructure and development of iron mineralization in the radular teeth of *Cryostochiton stelleri* (Mollusca). *J. Ultrastruct. Res.* **17**, 1 – 13.
- Troost KZ. 1993. Assessment of implantation damage by backscatter Kikuchi diffraction in the scanning electron microscope. *Appl. Phys. Lett.* **63**, 958 – 960.
- Vendrasco MJ, Checa AG, Kouchinsky AV. 2011. Shell microstructure of the early bivalve *Pojetaia* and the independent origin of nacre within the mollusca. *Palaeontology* **54**, 825 – 850.
- Vidavsky N, Addadi S, Mahamid J, Shimoni E, Ben-Ezra D, Shpigel M, Weiner S, Addadi L. 2014. Initial stages of calcium uptake and mineral deposition in sea urchin embryos. *Proc. Natl. Acad. Sci. USA* **111**, 39 – 44.
- Vidavsky N, Addadi S, Schertel A, Ben-Ezra D, Shpigel M, Addadi L, Weiner S. 2016. Calcium transport into the cells of the sea urchin larva in relation to spicule formation. *Proc. Natl. Acad. Sci. USA* **113**, 12637 – 12642.
- Volmer M, Weber A. 1925. Nuclei formation in supersaturated states. *Z. Phys. Chem.* **119**, 277 – 301.

- Wada K. 1958. The crystalline structure on the nacre of pearl oyster shell. *Bull. Japan. Soc. Sci. Fish.* **24**, 422 – 427.
- Wada K. 1972. Nucleation and growth of aragonite crystals in the nacre of some bivalve molluscs. *Biomaterialization* **6**, 141 – 159.
- Wang RZ, Addadi L, Weiner S. 1997. Design strategies of sea-urchin teeth – Structure, composition and micromechanical relations to function. *Phil. Trans. R. Soc. London Ser. B* **352**, 469 – 480.
- Weiner S, Traub W. 1984. Macromolecules in mollusc shells and their functions in biomineralization. *Phil. Trans. R. Soc. B* **304**, 425 – 434.
- Weiner S, Sagi I, Addadi L. 2005. Choosing the crystallization path less traveled. *Science* **309**, 1027 – 1028.
- Weiner S, Addadi L. 2011. Crystallization pathways in biomineralization. *Annu. Rev. Mater. Res.* **41**, 21 – 40.
- Weiss IM, Tuross N, Addadi L, Weiner S. 2002. Mollusc larval shell formation: amorphous calcium carbonate is a precursor phase for aragonite. *J. Exp. Zool.* **293**, 478 – 491.
- Williams DB, Carter CB. 2009. Transmission electron microscopy: a textbook for materials science. Springer, New York.
- Wise Jr S, Hay W. 1968. Scanning electron microscopy of molluscan shell ultrastructures II. Observations of growth surfaces. *Trans. Am. Microsc. Soc.* **86**, 419 – 430.
- Wise Jr S. 1970. Microarchitecture and deposition of gastropod nacre. *Science* **167**, 1486 – 1488.
- Wolf SE, Böhm CF, Harris J, Demmert B, Jacob DE, Mondeshki M, Ruiz-Agudo E, Rodríguez-Navarro C. 2016. Nonclassical crystallization in vivo et in vitro (I): Process-structure-property relationships of nanogranular biominerals. *J. Struct. Biol.* **196**, 244 – 259.
- Xu X, Han JT, Kim DH, Cho K. 2006. Two modes of transformation of amorphous calcium carbonate films in air. *J. Phys. Chem. B* **110**, 2764 – 2770.
- Yang L, Killian CE, Kunz M, Tamurad N, Gilbert PUPA. 2011. Biomineral nanoparticles are space-filling. *Nanoscale* **3**, 603 – 609.
- Younis S, Kauffmann Y, Bloch L, Zolotoyabko E. 2012. Inhomogeneity of nacre lamellae on the nanometer length scale. *Cryst. Growth Des.* **12**, 4574 – 4579.
- Yu DH, Chu KH. 2006. Genetic variation in wild and cultured populations of the pearl oyster *Pinctada fucata* from southern China. *Aquaculture* **258**, 220 – 227.
- Zhang G, Xu J. 2013. From colloidal nanoparticles to a single crystal: new insights into the formation of nacre's aragonite tablets. *J. Struct. Biol.* **182**, 36 – 43.
- Zhao J, Liu Y, Sun W-b, Yang X. 2012. First detection, characterization, and application of amorphous calcium phosphate in dentistry. *J. Dental Sciences* **7**, 316 – 323.
- Zhou D, Metzler RA, Tyliczszak T, Guo J, Abrecht M, Coppersmith SN, Gilbert PUPA. 2008. Assignment of polarization-dependent peaks in carbon K-edge spectra from biogenic and geologic aragonite. *J. Phys. Chem. B* **112**, 13128 – 13135.
- Zubavichus Y, Shaporenko A, Grunze M, Zharnikov M. 2005. Innershell absorption spectroscopy of amino acids at all relevant absorption edges. *J. Phys. Chem. A* **109**, 6998 – 7000.

List of Abbreviations

ACC	Amorphous Calcium Carbonate
ACP	Amorphous Calcium Phosphate
AFM	Atomic Force Microscopy
ADP	Adenosine Diphosphate
ATP	Adenosine Triphosphate
ATPase	Adenosine Triphosphatase
BF	Bright Field
BSE	Backscattered Electrons
CA	Carbonic Anhydrase
Ca ⁺²	Calcium ion
CaCO ₃	Calcium carbonate
Cc	Chromatic aberration
CO ₂	Carbon dioxide
CO ₃ ⁻²	Carbonate ion
Cs	Spherical aberration
EBSD	Electron Backscattered Diffraction
EDS	Energy Dispersive X-ray Spectroscopy
EELS	Electron Energy Loss Spectroscopy
ELNES	Energy Loss Near-Edge Structure
EXELFS	Extended Energy Loss Fine Structure

FEG	Field Emission Gun
FESEM	Field Emission Scanning Electron Microscopy
FFT	Fast Fourier Transform
FT	Fourier Transform
FHWM	Full Width Half-Maximum
HAADF	High Angle Annular Dark Field
HCO ⁻³	Hydrogen carbonate or bicarbonate
HRTEM	High Resolution Transmission Electron Microscopy
ILM	Interlamellar Membrane
M	Molar, moles per litre
Ma	Million years
MV	Matrix Vesicle
Na ⁺	Sodium ion
OCP	Octacalcium Phosphate
OsO ₄	Osmium tetroxide
PBS	Phosphate-Buffered Saline
PEEM	Photoemission Electron Spectromicroscopy
P _i	Inorganic phosphate
PIC	Polarization-dependent Imaging Contrast
PO ₄ ⁻³	Phosphate ion
pH	Potential of Hydrogen
PMC	Primary Mesenchymal Cell
SAED	Selected Area Electron Diffraction
SE	Secondary Electrons
SEM	Scanning Electron Microscopy
SM	Surface Membrane
SNR	Signal to Noise Ratio
SPM	Scanning Probe Microscopy
STEM	Scanning Transmission Electron Microscopy
TEM	Transmission Electron Microscopy

List of related publications *

Checa A, Macías-Sánchez E, Ramírez-Rico J. 2016. Biological strategy for the fabrication of highly ordered aragonite helices: the microstructure of the cavolinioidean gastropods. *Sci. Rep.* **6**, 25989. DOI 10.1038/srep25989

Checa A, Macías-Sánchez E, Harper EM, Cartwright JHE. 2016. Organic membranes determine the pattern of the columnar prismatic layer of mollusc shells. *Proc. R. Soc. B* **283**, 20160032. DOI 10.1098/rspb.2016.0032

Barge LM, Cardoso SSS, Cartwright JHE, Doloboff IJ, Flores E, Macías-Sánchez E, Sainz-Díaz CI, Sobrón P. 2016. Self-assembling iron oxyhydroxide/oxide tubular structures: laboratory-grown and field examples from Rio Tinto. *Proc. R. Soc. A* **472**, 20160466. DOI 10.1098/rspa.2016.0466

*Research undertaken during the period of candidature and not included in this dissertation.

Acknowledgements

I would like to express my deepest and sincere gratitude to my advisor, Professor Antonio Checa for his enlightening guidance and inspiring instruction in the completion of this study. I have certainly benefited and enjoyed the enthusiasm that he devotes for biomineralization and all the aspects related with the production of scientific knowledge, with an endless capacity of work, rectitude and scientific truthfulness. I really appreciate the opportunity that he gave me to accomplish the PhD degree and his respectful and continuous support.

I would like to thank the rest of my group, Dr. Julyan Cartwright and Dr. Ignacio Sainz-Díaz, for our fruitful discussions and especially for promoting my internationalization, encouraging me to visit other research centres as a way to grow as a scientist, and allowing me to discover new methodologies and perspectives.

I am grateful to Dr. Xing Huang (Fritz Haber Institute, Berlin) who answered hundreds of questions and solved more than one problem related with the transmission electron microscope. I am also very thankful to Achim Klein (Fritz Haber Institute, Berlin) who introduced me to different sample preparation techniques for electron microscopy, and who transmitted me the need to work with neatness and delicacy.

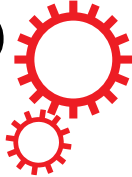
I would like to express a warm thank you to all the Professors and colleagues of the Department of Stratigraphy and Palaeontology of the University of Granada, for enabling such a friendly work environment, and for the good moments and discussions that we have shared. I also want to express my appreciation to my office mates in the department (Paola, Maria José, Jon, Anja, Vedrana, Noel, Ío), with whom we have maintained an atmosphere of efficient work always with good mood.

I am most grateful to my partner Danail for his eternal patience, understanding and support in this long travel that has deprived him of much private life. Without his help, this PhD work would not have been possible. Last but not least, I want to acknowledge to all my family, the Bulgarian and the Spanish, for their encouragement and unconditional support.

Appendixes: publications

- Transformation of ACC into aragonite and the origin of nanogranular structure of nacre
Macías-Sánchez *et al.* 2017. *Scientific Reports* (in press)
DOI 10.1038/s41598-017-12673-0
- Crystallographic control on the substructure of nacre tablets
Checa *et al.* 2013 *Journal of Structural Biology*
DOI 10.1016/j.jsb.2013.07.014
- The transport system of nacre components through the surface membrane of gastropods
Macías-Sánchez *et al.* 2015 *Key Engineering Materials*
DOI 10.4028/www.scientific.net/KEM.672.103

SCIENTIFIC REPORTS



OPEN

Transformation of ACC into aragonite and the origin of the nanogranular structure of nacre

Elena Macías-Sánchez^{1,2}, Marc G. Willinger^{3,4}, Carlos M. Pina⁵ & Antonio G. Checa^{1,2}

Currently a basic tenet in biomineralization is that biominerals grow by accretion of amorphous particles, which are later transformed into the corresponding mineral phase. The globular nanostructure of most biominerals is taken as evidence of this. Nevertheless, little is known as to how the amorphous-to-crystalline transformation takes place. To gain insight into this process, we have made a high-resolution study (by means of transmission electron microscopy and other associated techniques) of immature tablets of nacre of the gastropod *Phorcus turbinatus*, where the proportion of amorphous calcium carbonate is high. Tablets displayed a characteristic nanoglobular structure, with the nanoglobules consisting of an aragonite core surrounded by amorphous calcium carbonate together with organic macromolecules. The changes in composition from the amorphous to the crystalline phase indicate that there was a higher content of organic molecules within the former phase. Within single tablets, the crystalline cores were largely co-oriented. According to their outlines, the internal transformation front of the tablets took on a complex digitiform shape, with the individual fingers constituting the crystalline cores of nanogranules. We propose that the final nanogranular structure observed is produced during the transformation of ACC into aragonite.

The production of amorphous minerals by organisms is a long-known fact, but it was not until the pioneering work of Towe and Lowenstam¹ that evidence for the formation of the biominerals by both vertebrates and invertebrates through the corresponding amorphous transient phases began to accumulate.

Calcium carbonate is, with few exceptions, the most common material used by invertebrates to construct their hard structures (shells, plates, spicules, etc.). These are made basically of calcite, aragonite and, very rarely, of vaterite. The first amorphous phase in calcium carbonate systems was detected in the larval spicule of the sea urchin², as electrodense granules inside spiculogenic cell vesicles, which are subsequently transported to the mineralization site³. Subsequently, amorphous calcium carbonate (ACC) appears in regenerating adult spines and has been shown to transform into calcite⁴.

Transformation of ACC into aragonite was proposed in embryos of a pulmonate snail^{5,6}, in larval bivalves⁷, and in freshwater cultured pearls⁸, based on a large variety of techniques (high-resolution X-ray diffraction, Raman spectroscopy, Scanning and Transmission Electron Microscopy – SEM and TEM)⁹. Although on calcitic materials, the TEM recognition by Baronnet *et al.*¹⁰ of an amorphous cortex (several tens of nm thick) in the prisms of the pearl oyster *Pinctada margaritifera* is interesting, since the cortex was located exactly at the growth fronts of the prisms. Despite being the most intensively studied natural organic-inorganic biocomposite in invertebrates, the evidence of ACC associated to nacre is scant. Besides the previously mentioned report of ACC granules in pearls by Jacob *et al.*⁸, Nassif *et al.*¹¹ found an amorphous rim 3–5 nm thick around mature nacre tablets; they recrystallized the amorphous rim under the electron beam and indexed the recrystallized areas as aragonite. Subsequently, Zhang and Xu¹² provided images of nacre crystalline nanodomains immersed in amorphous material. Recognition of ACC in nacre was made by DeVol *et al.*¹³. Their photoemission electron spectromicroscopy (PEEM) maps clearly showed that ACC is more abundant in younger tablets (towards the top of gastropod nacre towers). This is consistent with the fact that ACC transforms progressively into aragonite as tablets age.

¹Department of Stratigraphy and Palaeontology, University of Granada, Granada, 18071, Spain. ²Andalusian Earth Sciences Institute (IACT), UGR – CSIC, Avd. de las Palmeras 4, Armilla, 18100, Granada, Spain. ³Department of Inorganic Chemistry, Fritz Haber Institute of the Max Planck Society, Berlin, 14195, Germany. ⁴Department of Colloid Chemistry, Max Planck Institute of Colloids and Interfaces, 14476, Potsdam, Germany. ⁵Department of Crystallography and Mineralogy, Complutense University of Madrid, Geosciences Institute (IGEO) (UCM-CSIC), E-28040, Madrid, Spain. Correspondence and requests for materials should be addressed to A.G.C. (email: acheca@ugr.es)

There is presently evidence that the formation of biominerals does not seem to proceed via the aggregation of monomers (as postulated by the classical crystallization theory), but by a nonclassical crystallization via an aggregation-based growth mechanism of precursor nanoparticles. At the same time, the biominerals are characterized by a nanostructure made of tightly-packed nanosized crystalline granules separated by intergranular sheaths of a different nature (usually implied to be organic). This nanotextural imprint is taken as evidence of the particle aggregation mechanism (see the recent comprehensive reviews in^{14,15}). In nacre, the nanogranular substructure was revealed time ago^{16,17}. Hovden *et al.*¹⁸ observed that the onset of nacre in the bivalve *Pinna nobilis* initiates with nanofibrillar aggregations of nanoparticles, which grade into irregular early-nacre lamellae, and then into well-ordered mature nacre. They interpreted this as evidence that the process is driven by aggregation of nanoparticles (50–80 nm).

Until now, a study combining high-resolution imaging with unambiguous recognition of ACC and its distribution within nacre platelets has been lacking. Following DeVol *et al.*¹³, we have selected incipient nacre tablets, where ACC is more abundant. We have used the relatively common littoral gastropod *Phorcus turbinatus*. By combining different high-resolution Scanning/Transmission Electron Microscopy (S/TEM) techniques, Atomic Force Microscopy (AFM), and elemental analysis we have visualized for the first time the distribution of the amorphous and crystalline phases at the nanoscale, which has in turn allowed us to elucidate the progressive crystallization mechanism in nacre and relate it with the nanogranular structure of nacre.

Results

Gastropod nacre tablets are stacked in towers¹⁹ (Fig. 1A), each tablet having a pseudo-hexagonal contour (Fig. 1B). Our oblique sections revealed the characteristic porous structure of the interlamellar membranes (Fig. 1C). Tablets consisted of an aggregation of globular particles measuring between 20–50 nm (Fig. 1D–F). The irregular topography became particularly evident with secondary electrons (SE) (Fig. 1E), whereas it remained masked in TEM (Fig. 1B–D). Similar nanoparticles were also found over the interlamellar membranes (ILMs) (Fig. 1D–F), and are likely the remains of hillocks cut during sample preparation. Hillocks, i.e. the protrusions (20–100 nm) of the tablet surface across the pores of the ILM (Supplementary Fig. 1), maintain crystallographic coherence with the rest of the tablet²⁰. HRTEM highlights that the cores of these globular particles both from the tablet interior and/or the hillocks were crystalline nanodomains (average size 30 nm) embedded in an amorphous matrix (5–10 nm in thickness; Fig. 1G–I). Some forming tablets also presented amorphous edges, which crystallized under the electron beam (in much the same way as reported by Nassif *et al.*¹¹; Supplementary Fig. 2). In other instances, edges were fully crystalline.

The examination of nanoparticles spread over the ILMs using High Annular Dark Field (HAADF) imaging allowed us to differentiate the amorphous coating from the organic (amorphous) background, which remained concealed in TEM (Supplementary Fig. 3). HAADF enhances the contrast between materials of different composition (different average atomic Z number) (Fig. 1F). For the same average Z, variations in contrast are due to density or thickness changes²¹. Accordingly, CaCO₃ nanoparticles showed an intense contrast (bright areas) with respect to the organic background (Fig. 2A). The highest contrast (Fig. 2B) corresponded to the crystalline core identifiable by lattice fringes (Fig. 2C). Cores were bordered by non-crystalline areas with intermediate contrast (Fig. 2B–D) that faded gradually towards the edges (Fig. 2C,D). Electron Energy Loss Spectroscopy (EELS) confirmed the same qualitative composition for both the crystalline cores and the amorphous rims (Fig. 2D), with the intensity of the calcium L-edge being significantly higher in the crystalline cores.

Besides the sectioned hillocks, there were two other types of nanoparticles scattered over the organic amorphous material: type one, 2–5 nm in size (Fig. 2B,F), and type two, 10–20 nm (Fig. 2E). Both of these nanoparticles returned a calcium signal (Fig. 2E) and had a non-crystalline structure (Fig. 2E,F).

Indexing of crystalline nanodomains (30–50 nm) surrounded by amorphous matter of the tablet interior corroborated their aragonite nature (error <5%). No other polymorph was detected. FFT of the image covering several nanodomains in Fig. 3A returned short arcs instead of sharp points, which result from the addition of slightly misaligned reflections (Fig. 3B). By selecting the signals of the misaligned planes from the FFT and inverting the FFT function, we located the source areas of these signals. In this way, it became evident that the signals came from adjacent, slightly misaligned (1.7° and 1.9°) nanodomains (Fig. 3C). Remarkably, the nanodomains were not oval (the case in Fig. 1H is an exception), but had highly irregular contours that connected with and even overlapped one another (Fig. 3D). A case similar to that in Fig. 3A–C is shown in Supplementary Fig. 4.

When indexing could be made exactly along the [001] zone axis, we appreciated that the crystalline nanodomains (Fig. 3E) had their *c*-axes co-aligned, but they were slightly misaligned in the *a*-*b* plane (Fig. 3F). An example of hillocks adhering to ILMs is shown in Fig. 3D–F. Some nanodomains presented twin relationships (Fig. 3G–I).

We performed both AFM and S/TEM on single tablets (Fig. 4), with both revealing the globular texture typical of nacre^{17,22,23} and other biominerals^{10,24}. AFM phase contrast images (which enable the detection of variations in adhesion, friction and viscoelasticity²⁵; see explanation in Supplementary Fig. 5) revealed two different materials (Fig. 4D): one with more adhesive strength (low contrast), previously assumed to be either organic material^{17,22}, or a mixture of organics and ACC²⁶, and a second, stiffer material, assumed to be the crystalline phase by the same authors. The topographic images showed that the low-contrast layer extended over the stiffer material in the form of discontinuous pellicles (with variable thicknesses, between 2–10 nm, *n* = 10).

Observation of exactly the same areas by S/TEM (Fig. 4A–C) provided complementary information. The topographic contrast generated by SE in STEM is basically surface-tilt contrast: SEs created on an inclined surface or close to a surface step have an increased probability of escaping, thus producing a higher brightness/contrast²⁷. The irregularities observed with SEs (Fig. 4E) were less pronounced in the AFM images, but they correlated well with the topographic profiles, that revealed a very irregular surface. The overlap of both the SE and the

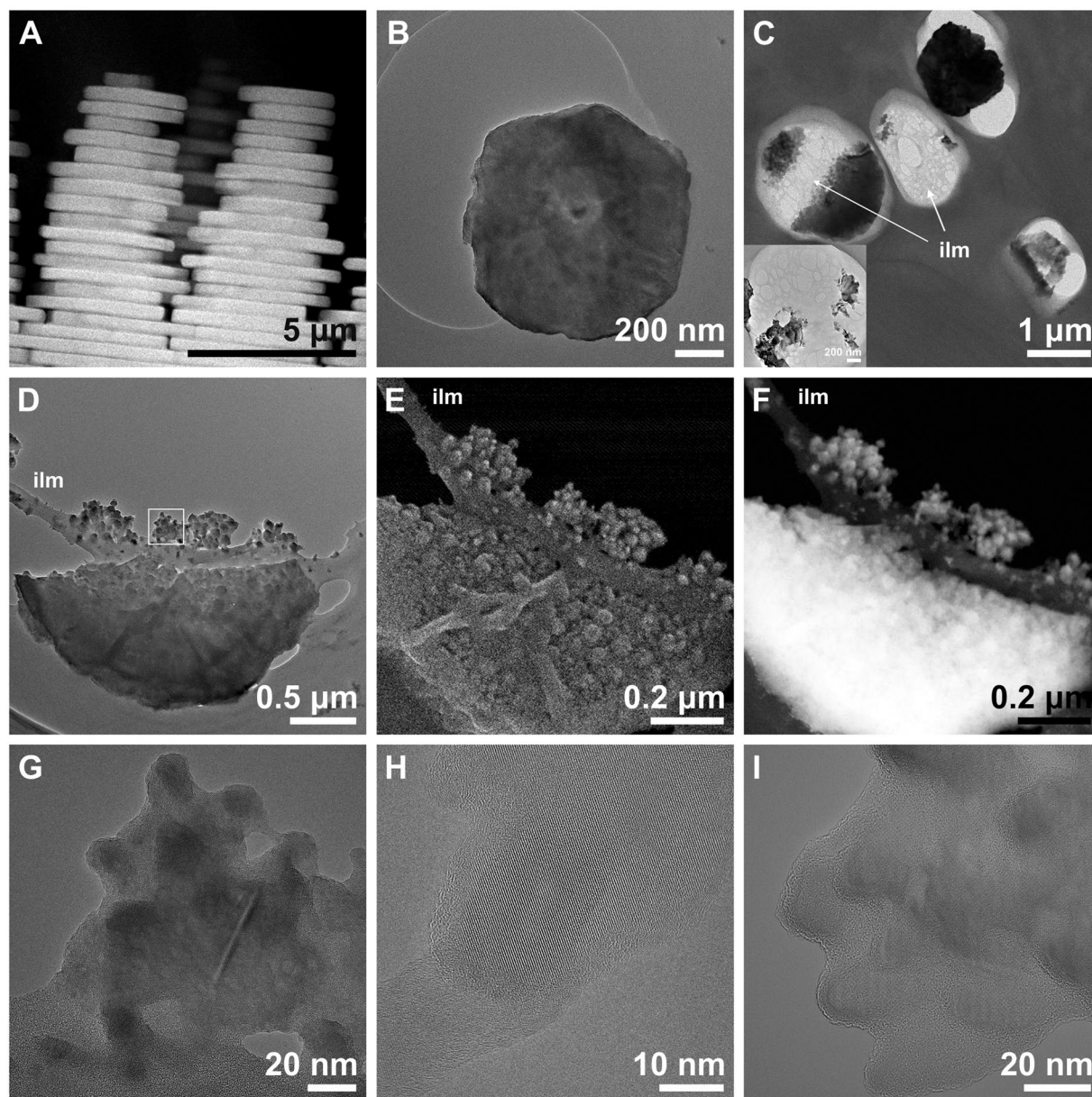


Figure 1. Gastropod nacre tablets from macro- to nanoscale. **(A)** Lateral view of nacre towers (HAADF). **(B)** Tablet at the top of a tower cut almost perpendicular to the growth axis of the tower, with its characteristic pseudo-hexagonal shape. **(C)** Slightly oblique section of some tablets. The characteristic porous structure of the interlamellar membranes (ilm) is visible. Inset, detail of the porous structure. **(D,E,F)** Image contrast comparison of a single tablet in TEM **(D)**, SE **(E)** and HAADF **(F)**. The tablet is composed of a myriad of nanogranules. Note the three-dimensional appearance provided by the SE image **(E)** compared to the other two modes. **(G)** HRTEM of the area framed in **(D)**: the nanogranules are composed by crystalline domains embedded in amorphous material. **(H)** Oval shaped crystalline nanodomain showing lattice fringes, with amorphous rims. **(I)** Detail of several crystalline domains embedded in amorphous matter.

low-contrast phase of the AFM images (Fig. 4F) showed that the distribution of the latter coincided relatively well with the flat (low-contrast, dark grey) areas observed in SE images.

EELS performed in crystalline and amorphous domains revealed differences in chemical bonding (Fig. 5). The C K-edge ELNES (Electron Energy-Loss Near-Edge Structure) spectra of crystalline areas (acquired in vacuum) showed two main peaks at 290.3 eV and 301.5 eV (Fig. 5A) that are unambiguously indicative of the CO_3^{2-} groups^{28–30}. The peak at 290.3 eV corresponds to $\text{C}1s \rightarrow \pi^*$ transitions, whereas the peak at 301.5 eV arises from $\text{C}1s \rightarrow \sigma^*$ transitions of carbon-oxygen bonds of carbonate CO_3^{2-} groups^{29,31}. Minor features related to π^* transitions of carbon-oxygen bonds, 294.2 and 298.3 eV³¹, were identified in only some spectra, with the former shifted to higher energies (295.5 eV) (Fig. 5A, Supplementary Fig. 6). Thus, the C K-edge is typical of carbon in carbonate groups in the crystalline areas.

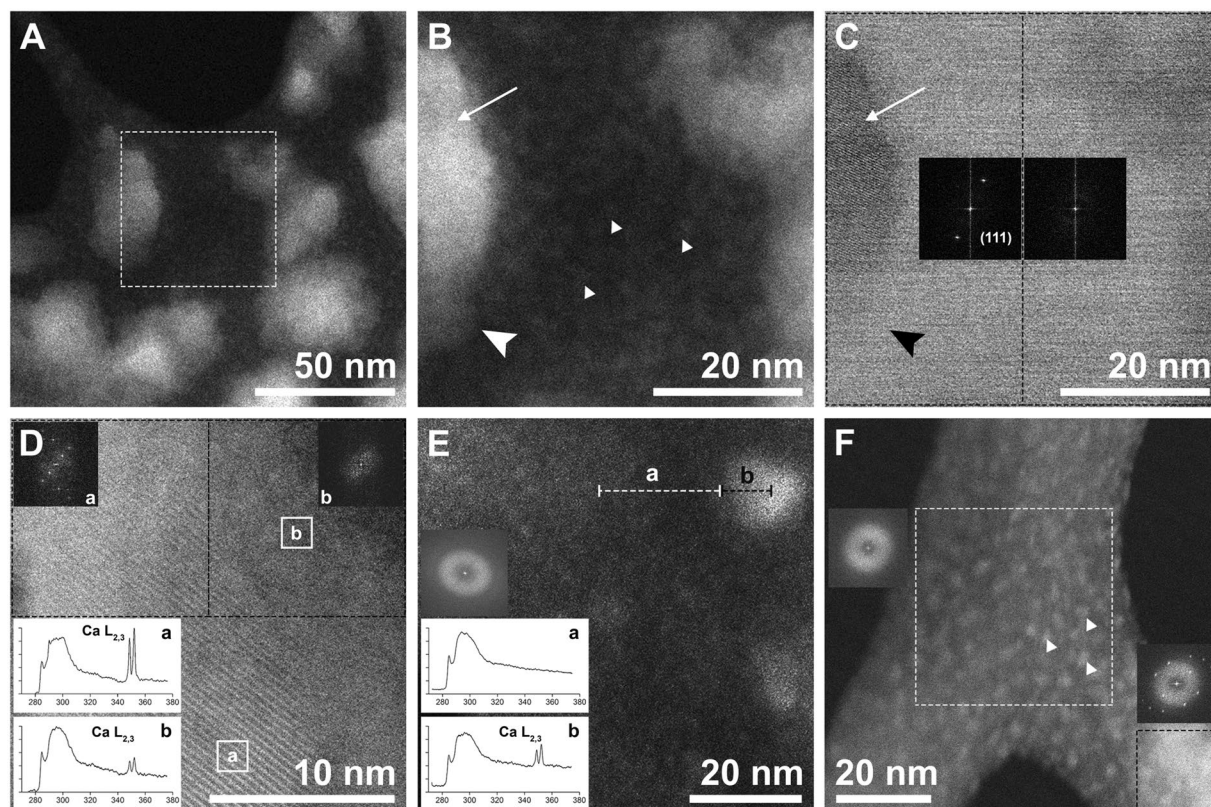


Figure 2. Nanoparticle crystallinity and composition. (A) Crystalline nanoparticles (rest of the tablet and/or hillocks) over the interlamellar membrane (organic amorphous material) (HAADF). (B) Closer view of the area framed in A. The highest contrast (brightest area) corresponds to the core of the particle (arrow). The contrast fades towards the lower edge of the same particle (large arrowhead). The nanoparticle to the right presents an intermediate contrast. Densely scattered type one nanoparticles (2–5 nm) (small arrowheads) with some contrast cover the organic amorphous material. (C) Bright-field (BF) STEM image of B. The particle to the left has a crystalline core (arrow) (indicated by lattice fringes and reflections in the FFT analysis). Its lower part (big arrowhead) does not show lattice fringes. Dashed rectangles indicate the areas where the FFTs come from. (D) Nanoparticle showing the crystalline area (lattice fringes and reflections) on the left and the surrounding amorphous material on the right (HAADF). Squares with dashed lines indicate the areas where the FFTs come from. Two EELS spectra from crystalline (a) and amorphous (b) areas are shown (background removed, deconvolved, normalized and smoothed). The areas where the spectra were obtained are indicated by solid squares. (E) Line scan EELS performed across the organic membrane (dashed line a) and a type-two particle (dashed line b). Only the particle with high contrast (12 nm in size) presented an intense calcium signal (b) (background removed, deconvolved, normalized and smoothed). The FFT from the whole image shows that no crystalline structure exists. (F) Densely scattered type-one nanoparticles (2–5 nm) (small arrowheads) over the organic membrane. FFTs show that nanoparticles have amorphous structure, unlike the bright lower right area, which has crystalline structure.

In amorphous areas, the C K-edge showed an initial peak at 285 eV and a second broad feature at 290 eV, typical of amorphous carbon (Fig. 5D,E). In areas where both crystalline and amorphous materials overlap (Fig. 5D-F), the spectrum was a linear combination of the spectra of amorphous carbon and carbon in carbonate form³².

Three pre-peaks at 285.0 (± 0.3), 287.5 (± 0.3) and 288.4 (± 0.3) eV (Supplementary Fig. 6), with different relative intensities depending on the sampled area, were identified. The 285.0 and 287.5 eV peaks arise from C1s $\rightarrow \pi^*$ in C=C and from C1s $\rightarrow \sigma^*$ in C-H in organic molecules, respectively^{33,34}. The 288.4 eV peak results from C1s $\rightarrow \pi^*$ in C=O of carboxyl groups of organic molecules^{31,33,35}. In crystalline areas only the 285.0 eV peak appears (Fig. 5), whereas in non-crystalline areas we recorded all three peaks (Supplementary Fig. 6). This indicates that although organic material is present in both phases, it is more noticeable in the amorphous phase.

The calcium L_{2,3}-edge ELNES spectrum is characterized by two main peaks at 349.3 and 352.6 eV (Fig. 5B). In the crystalline areas the presence of three and two minor features before the Ca L₃- and the Ca L₂-edges respectively indicates an aragonite nature¹³. Although we were unable to record the typical ACC profile (see methods), the Ca L_{2,3}-edge in the amorphous areas showed significantly less intensity (i.e. less crystallinity) (Fig. 2D).

The oxygen K-edge ELNES spectra in the crystalline areas are characteristic of aragonite, with a main peak at 534 (Fig. 5C) that results from O1s $\rightarrow \pi^*$ transitions from the C=O bonds^{34,36}, followed by a shoulder at 537.5 eV.

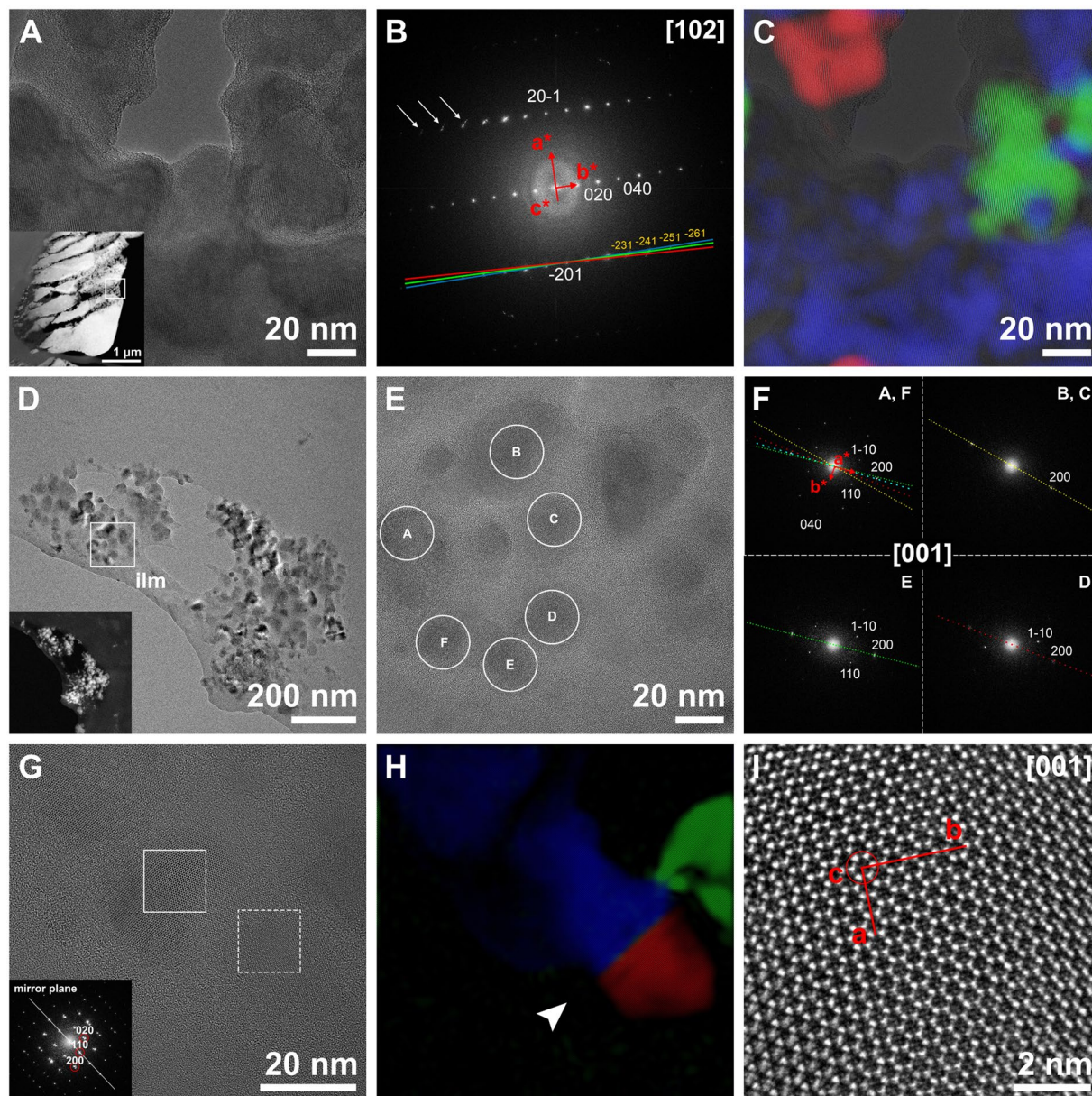


Figure 3. Orientations of crystalline nanodomains. (A) TEM image of crystalline nanodomains embedded in amorphous material. Inset: general view of the tablet with the location of the nanodomains. (B) FFT analysis of A. The presence of small arcs in the FFT (arrows) indicates slight misalignment between nanodomains. Colours of lines indicate the reflections used for the colour reconstruction in C. (C) RGB colour model built using the reflections corresponding to the planes $(\bar{2}31)$, $(\bar{2}41)$, $(\bar{2}51)$ and $(\bar{2}61)$ shown in B. Overlap of the original TEM image shows that crystallographically coherent nanodomains are separated by amorphous material. (D) Incipient tablet showing crystalline nanodomains immersed in amorphous material. The position of the interlamellar membrane is indicated (ilm). Inset: HAADF of the same area. (E) HRTEM of the area framed in D. Crystalline nanodomains over the interlamellar membrane. (F) FFT analysis of the nanodomains encircled in E (with the same letters). They are all indexed as aragonite along the $[001]$ zone axis. The nanodomains are slightly tilted, which results in the attenuation or even disappearance of some reflections. In each FFT the a -axis is marked with a coloured dotted line. The overlap of all lines (upper left FFT) shows the misalignment of a -axes between nanodomains. (G) HRTEM image of three different nanodomains over an organic membrane. Two of them show a twin relationship. Inset: FFT of the twin domain (area framed with dashed line). (H) Colour reconstruction of the three different domains. A (110) twin plane (arrowhead), characteristic of aragonite, separates the blue and red nanodomains. The green nanodomain is in contact with the blue one with a misorientation of 5.8° around the c -axis. (I) Enlargement of the area framed in G (solid line, blue nanodomain) indicating the crystallographic orientation. The view is from the c -axis.

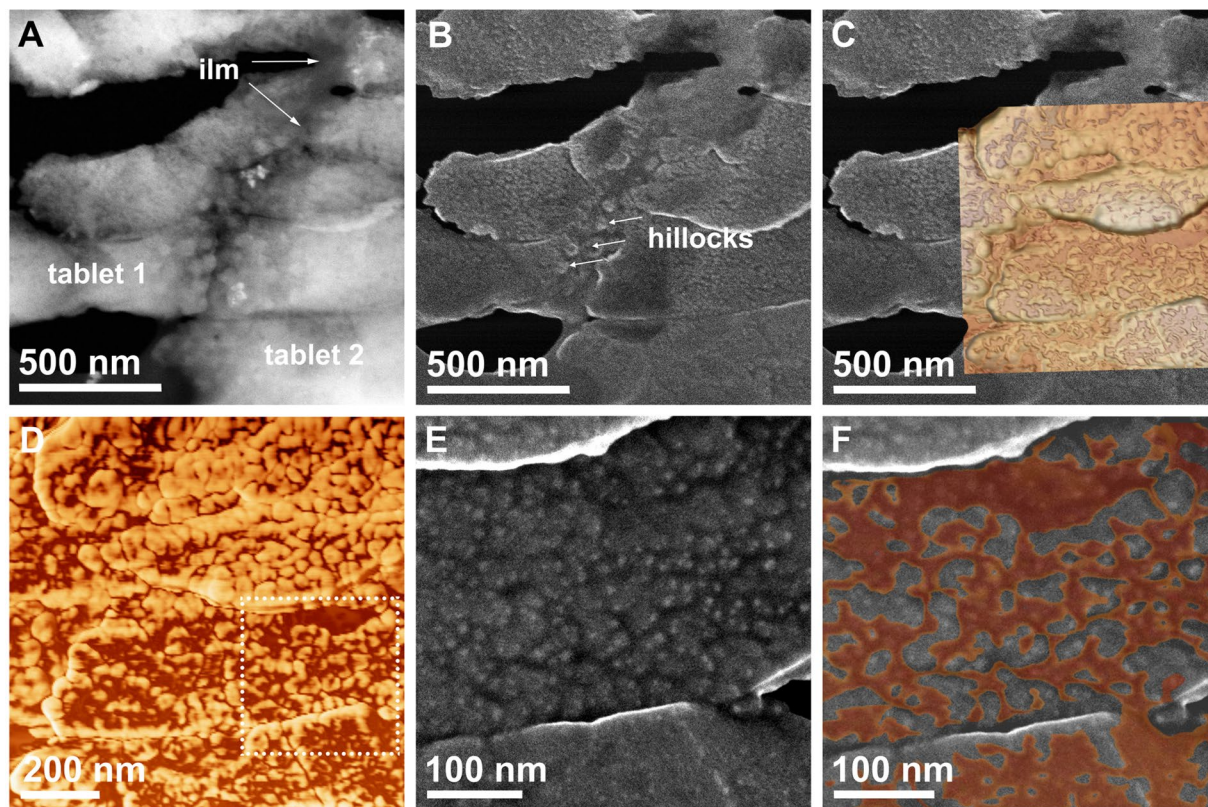


Figure 4. SE and AFM analysis of the same area. (A) HAADF image of two tablets and the intermediate interlamellar membrane (ilm) (darker material). (B) SE image of the same area. The smoothest area corresponds to the interlamellar membrane and some hillocks are visible at the boundary between the two tablets. (C) SE image with partially superposed AFM image (topographic + phase mode). (D) AFM phase image emphasizing the globular aspect of the structure. The more adhesive material (dark-brown areas) overlies the crystals (light-brown areas). (E) SE image of the area framed in D. The white dots are particularly steep areas, whereas darker areas tend to be horizontal. (F) Overlap of the darker areas of the AFM phase (brown) and SE (dark grey) images.

Two double peaks are defined at 540/541 eV, associated with the O1s $\rightarrow \sigma^*$ transitions of the carbonate CO_3^{2-} group³⁴ and at 544/545.5 eV, corresponding to O1s $\rightarrow \sigma^*$ transitions from the C=O absorptions³⁶ (assignments of peaks are summarized in Supplementary Table 1). In the amorphous areas, the O K-edge lost any fine structure and showed only a broad resonance.

In the transition to the amorphous areas the three edges presented a progressive reduction in the intensity of the peaks. The peaks from the C K-edge graded to a single broad shoulder (Fig. 5G), typical of amorphous carbon. The Ca $L_{2,3}$ -edge diminished drastically in intensity, and the O K-edge lost any fine structure and showed only a broad resonance.

Discussion

To test the hypothesis concerning the formation of the mature nacre through an amorphous transient phase, we selected incipient tablets of subadult gastropods. Our TEM study demonstrated that the tablets are composed by globules with a partially crystalline structure: a crystalline core (~ 30 nm) and an amorphous contour (~ 5 – 10 nm). The amount of amorphous material in developing crystals is significantly higher than that found in mature crystals¹⁴, in line with the results of DeVol *et al.*¹³, which suggests that the amount of amorphous material dwindles with the advance of the crystallization and the maturation of the tablet.

Within individual tablets, the indexing of adjacent crystalline nanodomains connected by amorphous material showed a minor misorientation (in the range of 2°). In particular, the *c*-axes showed the highest degree of co-alignment. The quantification of the misalignment of the *c*-axis in mature nacre tablets of *Mytilus edulis* with low acceleration voltage electron backscatter diffraction (EBSD) gave a mean angular spread in the order of 2° FWHM inside individual tablets³⁷, in agreement with our present results. The RGB colour reconstruction of the nanodomain orientation (Fig. 3C) clearly showed that the sectional outlines of the crystalline nanodomains are not simply spherical or oval, but complex, digitiform. The fact that separate digitiform domains were in exactly the same orientation indicates that they must connect in the third dimension. Apparently misoriented nanodomains were also found in our samples. Nevertheless, the impossibility of indexing them as aragonite or any other calcium carbonate polymorph has forced us to disregard them. Their presence might be related to sample preparation or beam damage (i.e. transformation into CaO), to which biogenic calcium carbonate is highly sensitive³⁸.

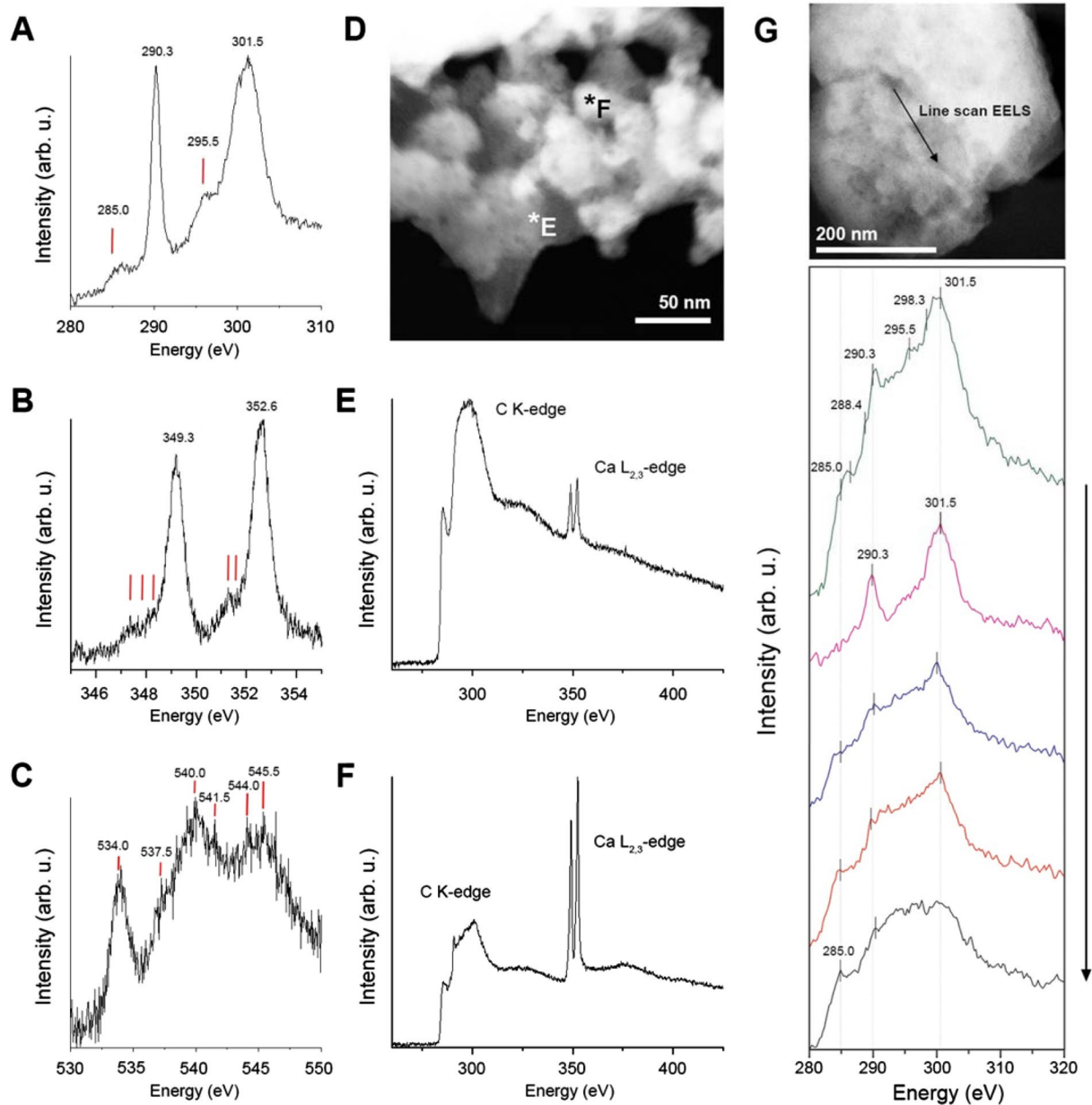


Figure 5. EEL Spectroscopy from incipient nacre. **(A)** The C K-edge shows two prominent peaks at 290.3 and 301.5 eV, indicating high crystallinity, but a weak hump at 285 eV that reflects the presence of organic material. **(B)** Ca $L_{2,3}$ edge. **(C)** O K-edge. For **(A,B)** and **(C)** background was removed before each edge. The spectra are normalized and the intensity is expressed in arbitrary units (arb. u.) for comparison. No smoothing was applied. **(D)** HAADF image showing the points where spectra E and F were taken. **(E)** C K-edge and Ca $L_{2,3}$ -edge from amorphous area. **(F)** Same edges from an area where crystalline and amorphous materials overlap (background removed and normalized). **(G)** STEM-EELS line scan shows progressive changes in the C K-edge from crystalline to amorphous areas. The top image depicts the segment (142.7 nm) where the line scan was performed (arrow indicates the direction of measurements). A total of 25 spectra (C K-edge) were taken (each 5.75 nm, dispersion 0.25 eV) and averaged (5 single spectra added) to reduce the noise. Background was removed before the C K-edge, and plural scattering was corrected. No smoothing was applied. Vertical lines represent locations of peaks described in Table S1. All spectra were acquired in vacuum (with no organic membrane or support underneath).

The finding of similarly misoriented nanodomains in the nacre of the bivalve *Perna viridis* led Zhang and Xu¹² to propose a formation mechanism based on the aggregation of completely misoriented nanodomains that afterwards realign by oriented attachment. Our data do not support this hypothesis. Nevertheless, we might consider the unlikely possibility of differences related to the independent origins of nacre in the four nacre-forming molluscan classes (gastropods, bivalves, cephalopods and monoplacophorans)³⁹.

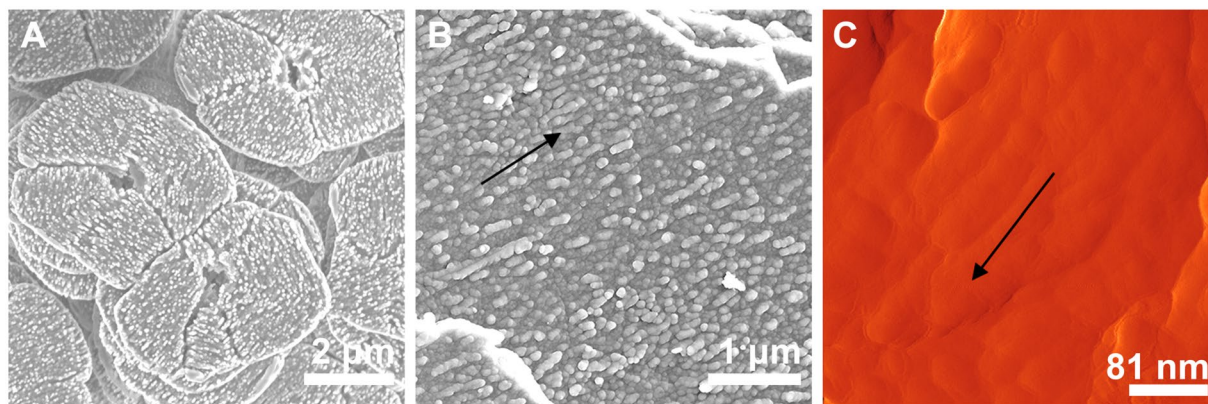


Figure 6. Fused and aligned nanoglobules in nacre. (A) Gastropod *Gibbula cineraria* nacre tablets, etched with Mutvei's solution, SEM view. (B) Cephalopod *Nautilus pompilius* septal nacre, bleached for 3 min, SEM view. (C) *Pteria hirundo*, treated with protease (0.2 g/ml, 1 h), AFM amplitude image.

Both organic matter and ACC have amorphous structures, making it unfeasible to differentiate them under traditional TEM, unless ACC is transformed by irradiation. Accordingly, the amorphous rims of nanoparticles were characterized by HAADF. The lack of lattice fringes and the recorded calcium content indicate that it is ACC. The lower contrast with respect to the crystalline core is likely to be due to its lower density. The density of ACC ($\rho_{\text{ACC}} = 1.62 \text{ g}\cdot\text{cm}^{-3}$)⁴⁰ is significantly lower than that of the crystalline phase ($\rho_{\text{aragonite}} = 2.93 \text{ g}\cdot\text{cm}^{-3}$).

At the transition from crystalline to amorphous areas, the C K-edge changed from multiple sharp peaks to a broad hump (Fig. 5D). Three pre-peaks at the C K-edge (285.0, 287.5 and 288.5 eV) appeared in both crystalline and amorphous material and are undoubtedly related to the presence of organic matter. Chitin and lipids can contribute to these peaks^{41,42}, but their low content in the organic fraction of nacre (~7% chitin⁴³; 0.54% lipids⁴⁴) leads us to believe that mostly proteins are responsible for these signals.

In the O K-edge, the intensity of the 534 eV peak varies with the degree of crystallinity³⁶. The intensity of the 534 eV peak in mature nacre is markedly higher than for the rest of the features⁴⁵. The weak 534 eV peak found in our samples indicates poor crystallinity.

In conclusion, our HRTEM and the ELNES analyses of the amorphous phase in incipient nacre tablets indicate that the phase that surrounds and partially covers the crystalline phase is composed of a mixture of ACC and organic matter (mainly proteins). This phase was previously suggested to be either organic^{17,22} or a mixture of organic macromolecules and ACC²⁶, but without conclusive evidence. We can ascertain that the latter is the case. This same amorphous phase, when observed under AFM, has a higher adhesion strength.

The presence of biogenic macromolecules occluded within the ACC stabilizes it against dissolution or rapid crystallization^{46–48}. Different kinds of additives have been identified as stabilizers, with amino acids being among the molecules that permanently stabilize ACC⁴⁴. Proteins have been demonstrated to inhibit ACC·H₂O dehydration⁴⁹, allowing the persistence of ACC·H₂O-rich nanoparticles.

In nacre, the continuity of the mineral bridges from one tablet to next⁵⁰ would allow the propagation of the crystal lattice. A neat crystallization front is absent. Conversely, we have observed complex, digitiform fronts that in 3D should branch off throughout the interior of the material. Transformation from amorphous to crystalline would happen concomitantly along this large-surface crystalline-amorphous interface. Concomitant transformation at different sites was implied by Addadi *et al.*⁴⁷ to occur also in the sea urchin larval spicule.

As the tablets mature and ACC crystallizes, some of the organic macromolecules may be occluded within the crystal lattice, while others would be expelled by the crystallization force and would tend to concentrate in progressively shrinking ACC areas. Their accumulation might “poison” the crystallization process⁵¹ and permanently stabilize the residual organic-rich ACC, which would accumulate around crystalline globules²⁶. These would remain as pellicles around crystalline globules (commonly observed in low contrast under AFM phase mode).

This model entails a noteworthy conclusion: our observations reveal that the nanoglobules consist of a crystalline core and an amorphous cortex; the crystalline cores can be assimilated to the fingers emitted from the digitiform crystallization front. Accordingly, the observed nanoglobular structure of nacre is due to the presence of precursor ACC and is modulated during the progressive process of transformation of ACC into aragonite. Our results match those of Checa *et al.*⁵², who found that the nanoglobules in nacre elongate and/or align in parallel to the *a*-axis of aragonite (Fig. 6), i.e., they are crystallographically controlled features.

Our data are consistent with a particle-accretion mechanism in nacre. The two types of ACC nanoparticles detected on the ILMs (type one, 2–5 nm, and type two, 10–20 nm) are in the size range of the aggregation units described in synthetic systems^{53,54} and it is likely that they are the first ACC intermediates. Hence, the sizes of the nanoglobules do not necessarily represent the sizes of the initial aggregation particles, contrary to what was implied by some authors⁴⁸.

Two hypotheses have been proposed for the transformation of ACC into the crystalline phase. First, transformation was hypothesised to occur via secondary nucleation^{55,56} (but see¹⁴ for the inadequacy of the term), whereby both phases are in contact and undergo a solid-state transformation⁵⁷. Nevertheless, as described above, the final nanostructure is modulated by the transformation of ACC into aragonite in the presence of organic

molecules, which are mobilised towards the contours of grains. This is only possible through the interface-coupled dissolution-precipitation process^{15,58,59}, which implies the existence of a fluid phase (partly resulting from H₂O released during the transformation of ACC into aragonite). In this way, reshaping of the overall nanogranular structure of grains takes place by regrowth of the crystalline phase (which can proceed via a classic layer-by-layer mechanism), until the nanograins acquire their final shapes, sizes (up to one order of magnitude bigger than the precursor ACC nanoparticles) and arrangements. This mechanism leads to pseudomorphs, thereby preserving the nanogranular structure imprinted during the early stages of nacre (Carlos Rodríguez-Navarro, personal communication, 2017). Regrowth was experimentally demonstrated in calcite⁵⁸. Given the similarity in nanostructure of nacre with most biominerals, it is likely that all of them followed a similar ACC-crystalline transformation route.

Methods

Specimens of the nacreous gastropod *Phorcus turbinatus* were caught alive in La Herradura (36°43′44″N, 3°43′35″W), on the coast of the province of Granada (S Spain), *in vivo* frozen in liquid nitrogen and stored in a dewar flask. They were freeze-dried the day afterwards: the initial temperature (−170 °C) was raised slowly at an average pressure of 75 mTorr (Flexi-Dry MP); at the end of the drying cycle (2 days), when room temperature was reached (20 °C), the specimens were removed and stored at 4 °C. This process implies the removal of unbound water (sublimation phase or primary drying). The extraction of bound water requires a second phase (secondary drying or desorption) at relatively high temperatures (25° to 40 °C)⁶⁰.

Specimens were cut with a diamond saw and pieces from the nacre growth area were selected for embedding with Embed 812 (EMS), increasing the proportion of embedding medium to pure ethanol in three steps (1:2, 1:1 and 2:1). Osmication, *en bloc* uranyl acetate, and post-staining were avoided to prevent water contact and the addition of heavy metals that can interfere with analytical techniques.

Ultramicrotome (PowerTome X, Boeckeler) slices were cut as parallel as possible to the internal shell surface. With the progress of the diamond knife the crystals break into fragments with parallel edges, but the nanostructure remains in its original condition. The slices were laid on copper grids with lacey carbon to stabilize them under the electron beam. For imaging and elemental analysis, we used a double Cs corrected JEOL JEM-ARM200F TEM (Fritz Haber Institute of the Max Planck Society, Berlin) equipped with a cold-field emission gun, an energy dispersive X-ray detector (JEOL), a Gatan Imaging Filter (GIF Quantum), and a Gatan UltraScan 4000 camera.

The nanodomains were indexed by Fast Fourier Transform (FFT) analysis, using the DiffTools script package⁶¹ for Digital Micrograph (Gatan Inc.). The refined aragonite parameters of Caspi *et al.*⁶² were used to construct the unit cell in CaRIne Crystallography 3.1⁶³.

The *c*-axes of nacre towers rarely coincided with the nanodomain zone axis because sectioning was hardly perpendicular to the growth axis of the nacre towers (i.e. the normal to the section plane), the angles ranging between 0° and 24° for 12 nanodomains from different slices (Supplementary Fig. 7). Due to the sensitivity to electron beam irradiation, tilting of crystalline domains in a zone axis could not be performed. Therefore, we studied the relative orientations of adjacent nanodomains instead (Fig. 3 and Supplementary Fig. 4).

Electron Energy Loss Spectroscopy (EELS) spectra from 250 to 550 eV were recorded using a dispersion of 0.25 eV/channel, with a collection semi-angle $\beta = 27.7$ mrad and a 5-mm spectrometer entrance aperture. The energy resolution was ~1.25 eV measured by the full width at the half maximum (FWHM) in the zero-loss peak. For spectra covering two edges (i.e. from 275 to 375 eV), we used a dispersion of 0.05 eV/channel, with a collection semi-angle of $\beta = 20$ mrad and a 5-mm aperture. The energy resolution was ~0.65 eV at FWHM in the zero-loss peak. For one edge, we used a dispersion of 0.025 eV, a collection semi-angle of 14 mrad and a 2.5 mm aperture; energy resolution was ~0.5 eV at FWHM. Emission current was set to 5 μ A and the acquisition time was optimised to acquire sufficient signal intensity and to limit beam damage. The appearance of a prominent peak at 532 eV in the O K-edge is considered to be an indication of beam damage^{64,65}, so the integral dose applied was adjusted to below this threshold.

Only changes in the C k-edge could be tracked, given that the edge is very sensitive to bonding changes even at low-energy resolution. Since differences in the fine structure of the Ca L_{2,3} and O K-edges between ACC and aragonite are subtle^{13,36}, a high signal-to-noise ratio is necessary to unequivocally assign spectra to either of them, which results in compromising with the dose applied. In other instances, larger areas were used for data acquisition in order to reduce beam damage, thus precluding the characterization of the fine structure of the nanometric amorphous domains.

Background was subtracted before each edge using power-law fitting and plural scattering was removed when necessary using a Fourier-ratio deconvolution, both available in Digital Micrograph 2.30 software (Gatan Inc.). Plotting of the data and normalization were carried out with OriginPro 8.5 software.

Atomic force microscopy (AFM) was performed directly on the TEM grids. Areas of interest were previously selected by SEM on uncoated samples (Phenom Pro, University of Granada, Spain) and later manually located under the AFM using the X-Y translator of the optical head. Images were recorded in air at room temperature using an AFM (Multimode IIIa Veeco Instruments) of the Centro Nacional de Microscopía Electrónica (Universidad Complutense de Madrid, Spain). AFM was operated in tapping mode while displaying cantilever height, phase, and amplitude signals. Different areas of the sample were scanned using a ~14 × 14 μ m² piezo scanner and tips with a nominal radius of 8 nm supported by rectangular cantilevers with a nominal resonance frequency of 320 kHz, and a maximum spring constant of 80 N/m (Bruker TESP-V2). The scan rate was set to 1 Hz, and 256 to 512 lines per scan were recorded. All AFM images were subsequently analysed using NanoScope Analysis 1.50 (Bruker) and Nanotec WSxM. 4.0⁶⁶.

References

1. Towe, K. M. & Lowenstam, H. A. Ultrastructure and development of iron mineralization in the radular teeth of *Crystochiton stelleri* (Mollusca). *J. Ultrastruct. Res.* **17**, 1–13 (1967).
2. Beniash, E., Aizenberg, J., Addadi, L. & Weiner, S. Amorphous calcium carbonate transforms into calcite during sea urchin larval spicule growth. *Proc. R. Soc. Lond. B* **264**, 461–465 (1997).
3. Beniash, E., Addadi, L. & Weiner, S. Cellular control over spicule formation in sea urchin embryos: a structural approach. *J. Struct. Biol.* **125**, 50–62 (1999).
4. Politi, Y., Arad, T., Klein, E., Weiner, S. & Addadi, L. Sea urchin spine calcite forms via a transient amorphous calcium carbonate phase. *Science* **306**, 1161–1164 (2004).
5. Hasse, B., Ehrenberg, H., Marxen, J. C., Becker, W. & Epple, M. Calcium carbonate modifications in the mineralized shell of the freshwater snail *Biomphalaria glabrata*. *Chem. Eur. J.* **6**, 3679–3685 (2000).
6. Marxen, J., Becker, W., Finke, D., Hasse, B. & Epple, M. Early mineralization in *Biomphalaria glabrata*: microscopic and structural results. *J. Moll. Stud.* **69**, 113–121 (2003).
7. Weiss, I. M., Tuross, N., Addadi, L. & Weiner, S. Mollusc larval shell formation: amorphous calcium carbonate is a precursor phase for aragonite. *J. Exp. Zool.* **293**, 478–491 (2002).
8. Jacob, D. E., Wirth, R., Soldati, A. L., Wehrmeister, U. & Schreiber, A. Amorphous calcium carbonate in the shells of adult *Unionoida*. *J. Struct. Biol.* **173**, 241–249 (2011).
9. Cartwright, J. H. E., Checa, A. G., Gale, J. D., Gebauer, D. & Sainz-Díaz, C. I. Calcium carbonate polyamorphism and its role in biomineralization: how many amorphous calcium carbonates are there? *Angew. Chem. Int. Ed.* **51**, 11960–11970 (2012).
10. Baronnet, A., Cuif, J. P., Dauphin, Y., Farre, B. & Nouet, J. Crystallization of biogenic Ca-carbonate within organo-mineral microdomains. Structure of the calcite prisms of the Pelecypod *Pinctada margaritifera* (Mollusca) at the submicron to nanometre ranges. *Mineral. Mag.* **72**, 617–626 (2008).
11. Nassif, N. *et al.* Amorphous layer around aragonite platelets in nacre. *Proc. Natl. Acad. Sci. USA* **102**, 12653–12655 (2005).
12. Zhang, G. & Xu, J. From colloidal nanoparticles to a single crystal: new insights into the formation of nacre's aragonite tablets. *J. Struct. Biol.* **182**, 36–43 (2013).
13. DeVol, R. T. *et al.* Nanoscale transforming mineral phases in fresh nacre. *J. Am. Chem. Soc.* **137**, 13325–13333 (2015).
14. Wolf, S. E. *et al.* Nonclassical crystallization *in vivo et in vitro* (I): Process-structure-property relationships of nanogranular biominerals. *J. Struct. Biol.* **196**, 244–259 (2016).
15. Rodriguez-Navarro, C., Ruiz-Agudo, E., Harris, J. & Wolf, S. E. Nonclassical crystallization *in vivo et in vitro* (II): Nanogranular features in biomimetic minerals disclose a general colloid-mediated crystal growth mechanism. *J. Struct. Biol.* **196**, 260–287 (2016).
16. Mutvei, H. Ultrastructural studies on cephalopod shells. Part I: The septa and siphonal tube in *Nautilus*. *Bull. Geol. Institutions Univ. Uppsala* **3**, 237–261 (1972).
17. Dauphin, Y. Nanostructures de la nacre des tests de céphalopodes actuels. *Paläontologische Zeitschrift* **75**, 113–122 (2001).
18. Hovden, R. *et al.* Nanoscale assembly processes revealed in the macroprismatic transition zone of *Pinna nobilis* mollusc shells. *Nat. Commun.* **6**, 10097 (2015).
19. Wise, S. Jr. & Hay, W. Scanning electron microscopy of molluscan shell ultrastructures II. Observations of growth surfaces. *Trans. Am. Microsc. Soc.* **86**, 419–430 (1968).
20. Checa, A. G., Cartwright, J. H. E. & Willinger, M. G. Mineral bridges in nacre. *J. Struct. Biol.* **176**, 330–339 (2011).
21. Williams, D. B. & Carter, C. B. *Transmission electron microscopy: a textbook for materials science* (Springer, New York, 2009).
22. Rousseau, M. *et al.* Multiscale structure of sheet nacre. *Biomaterials* **26**, 6254–6262 (2005).
23. Checa, A. G. *et al.* Crystallographic control on the substructure of nacre tablets. *J. Struct. Biol.* **183**, 368–376 (2013).
24. Dauphin, Y. The nanostructural unity of mollusc shells. *Mineral. Mag.* **72**, 243–246 (2008).
25. Magonov, S. N., Elings, V. & Whangbo, M.-H. Phase imaging and stiffness in tapping-mode atomic force microscopy. *Surf. Sci.* **375**, 385–391 (1997).
26. Seto, J. *et al.* Structure-property relationships of a biological mesocrystal in the adult sea urchin spine. *Proc. Natl. Acad. Sci. USA* **109**, 3699–3704 (2012).
27. Reimer, L. *Scanning electron microscopy. Physics of image formation and microanalysis* (Springer, Berlin, 1998).
28. Hofer, F. & Golob, P. New examples for near-edge fine structures in electron energy loss spectroscopy. *Ultramicroscopy* **21**, 379–384 (1987).
29. Garvie, L. A. J., Craven, A. J. & Brydson, R. Use of electron-energy loss near-edge fine structure in the study of minerals. *Am. Min.* **79**, 411–425 (1994).
30. Brandes, J. A., Wirick, S. & Jacobsen, C. Carbon K-edge spectra of carbonate minerals. *J. Synchrotron Rad.* **17**, 676–682 (2010).
31. Zhou, D. *et al.* Assignment of polarization-dependent peaks in carbon k-edge spectra from biogenic and geologic aragonite. *J. Phys. Chem. B* **112**, 13128–13135 (2008).
32. Martin, J. M., Mansot, J. L. & Hallouis, M. Energy filtered electron microscopy (EFTEM) of overbased reverse micelles. *Ultramicroscopy* **30**, 321–328 (1989).
33. Kaznatcheyev, K. *et al.* Innershell absorption spectroscopy of amino acids. *J. Phys. Chem. A* **106**, 3153–3168 (2002).
34. Metzler, R. A. *et al.* Probing the organic-mineral interface at the molecular level in model biominerals. *Langmuir* **24**, 2680–2687 (2008).
35. Zubavichus, Y., Shaporenko, A., Grunze, M. & Zharnikov, M. Innershell absorption spectroscopy of amino acids at all relevant absorption edges. *J. Phys. Chem. A* **109**, 6998–7000 (2005).
36. DeVol, R. T. *et al.* Oxygen spectroscopy and polarization-dependent imaging contrast (PIC) - mapping of calcium carbonate minerals and biominerals. *J. Phys. Chem. B* **118**, 8449–8457 (2014).
37. Griesshaber, E. *et al.* Homoepitaxial meso- and microscale crystal co-orientation and organic matrix network structure in *Mytilus edulis* nacre and calcite. *Acta Biomater.* **9**, 9492–9502 (2013).
38. Golla-Schindler, U., Benner, G., Orchowski, A. & Kaiser, U. *In situ* observation of electron beam-induced phase transformation of CaCO₃ to CaO via ELNES at low electron beam energies. *Microsc. Microanal.* **20**, 715–722 (2014).
39. Vendrasco, M. J., Checa, A. G. & Kouchinsky, A. W. Shell microstructure of the early bivalve *Pojetaia* and the independent origin of nacre within the Mollusca. *Palaeontology* **54**, 825–850 (2011).
40. Bolze, J. *et al.* Formation and growth of amorphous colloidal CaCO₃ precursor particles as detected by time-resolved SAXS. *Langmuir* **18**, 8364–8369 (2002).
41. Lehmann, J. *et al.* *Biophysico-chemical processes involving natural nonliving organic matter in environmental systems* Ch. 17 (John Wiley & Sons, New Jersey, 2009).
42. Leung, B. O., Hitchcock, A. P., Won, A., Ianoul, A. & Scholl, A. Imaging interactions of cationic antimicrobial peptides with model lipid monolayers using X-ray spectromicroscopy. *Eur. Biophys. J.* **40**, 805–810 (2011).
43. Bezares, J., Asaro, R. J. & Hawley, M. Macromolecular structure of the organic framework of nacre in *Haliotis rufescens*: implications for growth and mechanical behavior. *J. Struct. Biol.* **163**, 61–75 (2008).
44. Rousseau, M. *et al.* Restoration of stratum corneum with nacre lipids. *Comp. Biochem. Physiol. B* **145**, 1–9 (2006).
45. Srot, V. *et al.* Microstructure, chemistry, and electronic structure of natural hybrid composites in abalone shell. *Micron* **48**, 54–64 (2013).

46. Aizenberg, J., Hanson, J., Koetzle, T. F., Weiner, S. & Addadi, L. Control of macromolecule distribution within synthetic and biogenic single calcite crystals. *J. Am. Chem. Soc.* **119**, 881–886 (1997).
47. Addadi, L., Raz, S. & Weiner, S. Taking advantage of disorder: amorphous calcium carbonate and its roles in biomineralization. *Adv. Mater.* **15**, 959–970 (2003).
48. Gal, A. *et al.* Particle accretion mechanism underlies biological crystal growth from an amorphous precursor phase. *Adv. Funct. Mater.* **24**, 5420–5426 (2014).
49. Gong, Y. *et al.* Phase transitions in biogenic amorphous calcium carbonate. *Proc. Natl. Acad. Sci. USA* **109**, 6088–6093 (2012).
50. Checa, A. G., Cartwright, J. H. E. & Willinger, M. G. The key role of the surface membrane in why gastropod nacre grows in towers. *Proc. Natl. Acad. Sci. USA* **106**, 38–43 (2009).
51. Aizenberg, J., Lambert, G., Addadi, L. & Weiner, S. Stabilization of amorphous calcium carbonate by specialized macromolecules in biological and synthetic precipitates. *Adv. Mater.* **8**, 222–226 (1996).
52. Checa, A. G. *et al.* Crystallographic control on the substructure of nacre tablets. *J. Struct. Biol.* **183**, 368–376 (2013).
53. Gebauer, D., Völkel, A. & Cölfen, H. Stable prenucleation calcium carbonate clusters. *Science* **322**, 1819–1822 (2008).
54. Pouget, E. M. *et al.* The initial stages of template-controlled CaCO₃ formation revealed by Cryo-TEM. *Science* **323**, 1455–1458 (2009).
55. Politi, Y. *et al.* Transformation mechanism of amorphous calcium carbonate into calcite in the sea urchin larval spicule. *Proc. Natl. Acad. Sci. USA* **105**, 17362–17366 (2008).
56. Killian, C. E. *et al.* Mechanism of calcite co-orientation in the sea urchin tooth. *J. Am. Chem. Soc.* **131**, 18404–18409 (2009).
57. Weiner, S. & Addadi, L. Crystallization pathways in biomineralization. *Annu. Rev. Mater. Res.* **41**, 21–40 (2011).
58. Rodríguez-Navarro, C., Burgos-Cara, A., Elert, K., Putnis, C. V. & Ruiz-Agudo, E. Direct nanoscale imaging reveals the growth of calcite crystals via amorphous nanoparticles. *Cryst. Growth. Des.* **16**, 1850–1860 (2016).
59. Rodríguez-Navarro, C., Elert, K. & Ševčík, R. Amorphous and crystalline calcium carbonate phases during carbonation of nanolimes: implications in heritage conservation. *CrystEngComm* **18**, 6594–6607 (2016).
60. Rey, L. & May, J. C. Freeze Drying/Lyophilization of Pharmaceutical and Biological Products. *Informa Healthcare, London* (2010).
61. Mitchell, D. R. G. DiffTools: software tools for electron diffraction in Digital Micrograph. *Microsc. Res. Tech.* **71**, 588–593 (2008).
62. Caspi, E. N., Pokroy, B., Lee, P. L., Quintana, J. P. & Zolotoyabko, E. *Acta Cryst.* **B61**, 129–132 (2005).
63. Boudias, C. & Monceau, D. CaRIne Crystallography 3.1 (1989–1998).
64. Garvie, L. A. J. Can electron energy-loss spectroscopy (EELS) be used to quantify hydrogen in minerals from the O K edge? *Am. Miner.* **95**, 92–97 (2010).
65. Nitriputri, K. *et al.* Nanoanalytical electron microscopy reveals a sequential mineralization process involving carbonate-containing amorphous precursors. *ACS Nano* **10**, 6826–6835 (2016).
66. Horcas, I. *et al.* *Rev. Sci. Instrum.* **78**, 013705 (2007).

Acknowledgements

We warmly thank Dr. Carlos Rodríguez-Navarro (University of Granada) for his unconditional advise on the details of the transformation of ACC into crystalline phases. Funding was provided by Research Projects CGL2013-48247-P of the Spanish Ministerio de Economía y Competitividad (MINECO) and Fondo Europeo de Desarrollo Regional (FEDER) (to all authors), and P10-RNM6433 of the Andalusian Consejería de Economía, Investigación, Ciencia y Empleo of the Junta de Andalucía, and by the Research Group RNM363 (latter Institution) (to E.M.-S and A.G.C.) E.M.-S. was funded by a PhD grant associated to Project P10-RNM643. A.C. also received support from the Unidad Científica de Excelencia UCE-PP2016-05, of the University of Granada. We acknowledge Dr. Robert Imlau (FEI Nanoport, The Netherlands) for tomographic acquisition and reconstruction.

Author Contributions

E.M.-S., conception, design, acquisition of data, and interpretation of data, drafting of the manuscript. C.M.P., acquisition and interpretation of data. M.G.W. and C.M.P. checked the draft manuscript and gave final approval. A.C.G., conception, design, interpretation of data, and revision of the manuscript.

Additional Information

Supplementary information accompanies this paper at <https://doi.org/10.1038/s41598-017-12673-0>.

Competing Interests: The authors declare that they have no competing interests.

Publisher's note: Springer Nature remains neutral with regard to jurisdictional claims in published maps and institutional affiliations.



Open Access This article is licensed under a Creative Commons Attribution 4.0 International License, which permits use, sharing, adaptation, distribution and reproduction in any medium or format, as long as you give appropriate credit to the original author(s) and the source, provide a link to the Creative Commons license, and indicate if changes were made. The images or other third party material in this article are included in the article's Creative Commons license, unless indicated otherwise in a credit line to the material. If material is not included in the article's Creative Commons license and your intended use is not permitted by statutory regulation or exceeds the permitted use, you will need to obtain permission directly from the copyright holder. To view a copy of this license, visit <http://creativecommons.org/licenses/by/4.0/>.

© The Author(s)

Transformation of ACC into aragonite and the origin of the nanogranular structure of nacre

Elena Macías-Sánchez^{1,2}, Marc G. Willinger^{3,4}, Carlos M. Pina⁵ and Antonio G. Checa^{1,2*}

¹ Department of Stratigraphy and Palaeontology, University of Granada, Granada 18071, Spain.

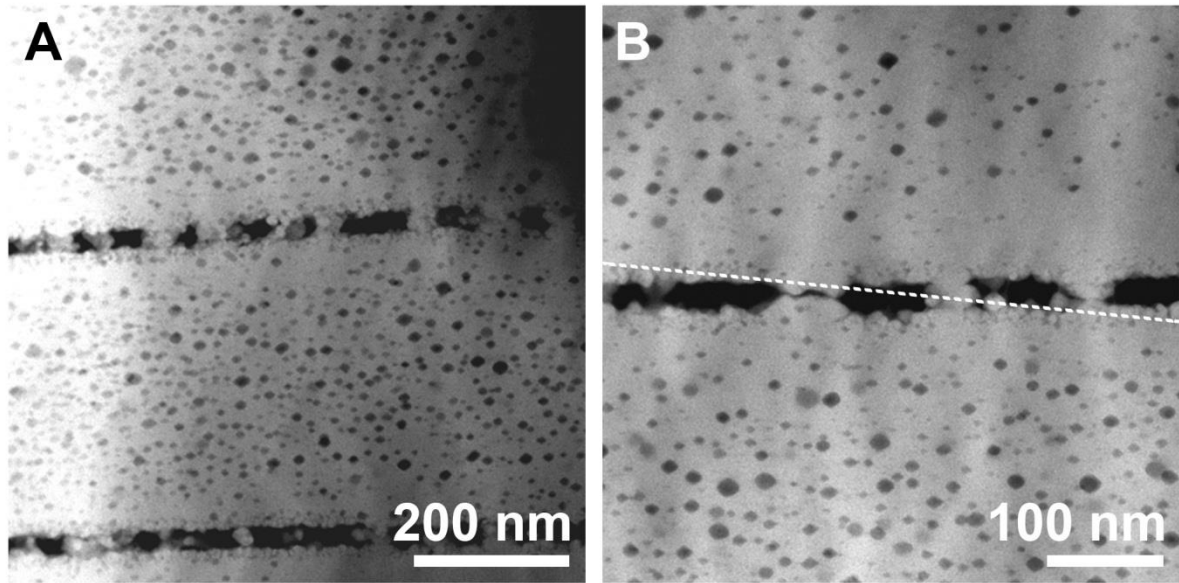
² Andalusian Earth Sciences Institute (IACT), UGR – CSIC, Avd. de las Palmeras 4, Armilla 18100 Granada, Spain.

³ Department of Inorganic Chemistry, Fritz Haber Institute of the Max Planck Society, Berlin 14195, Germany.

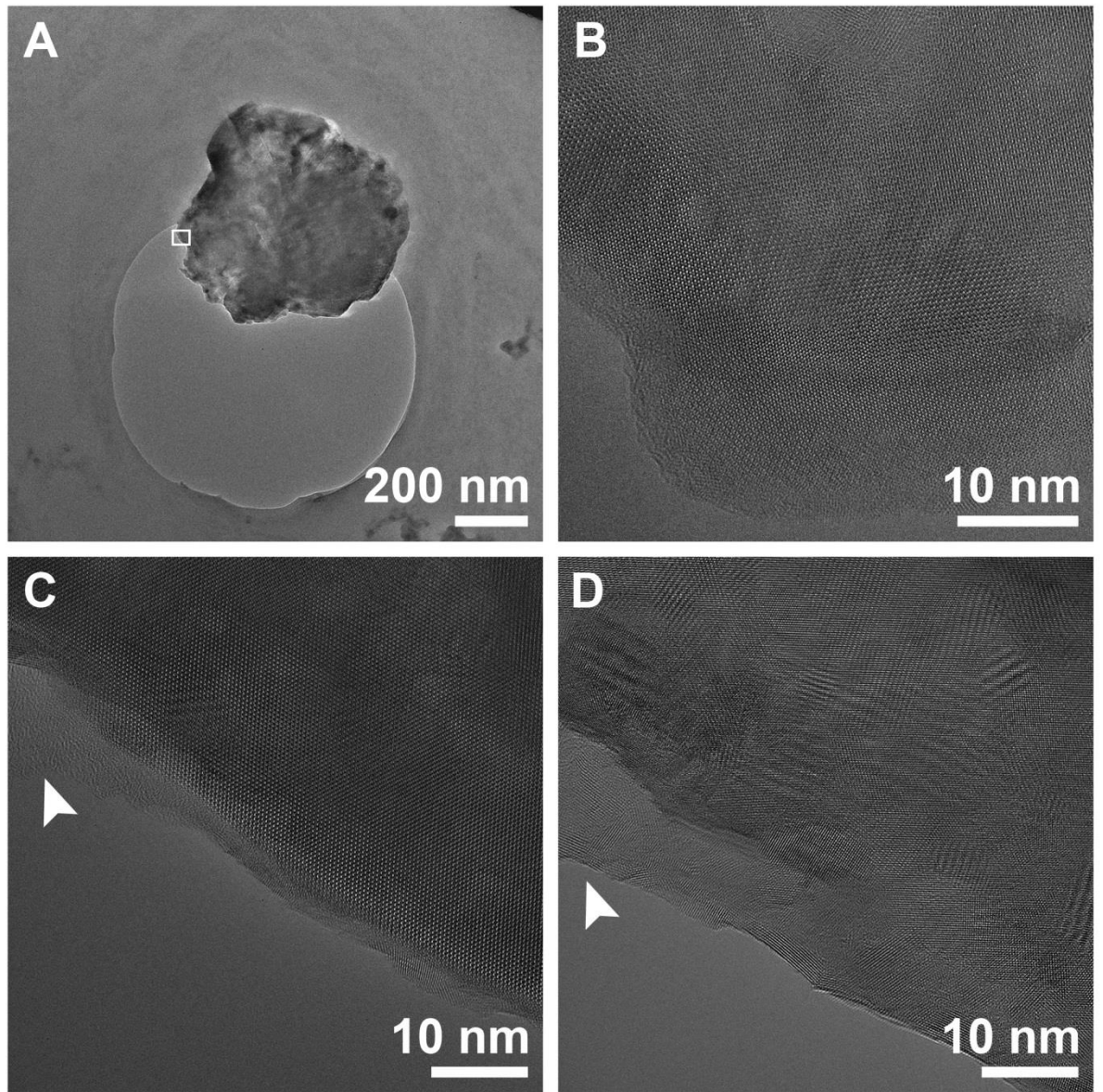
⁴ Department of Colloid Chemistry, Max Planck Institute of Colloids and Interfaces, 14476 Potsdam, Germany.

⁵ Department of Crystallography and Mineralogy, Complutense University of Madrid, Geosciences Institute (IGEO) (UCM-CSIC), E-28040 Madrid, Spain

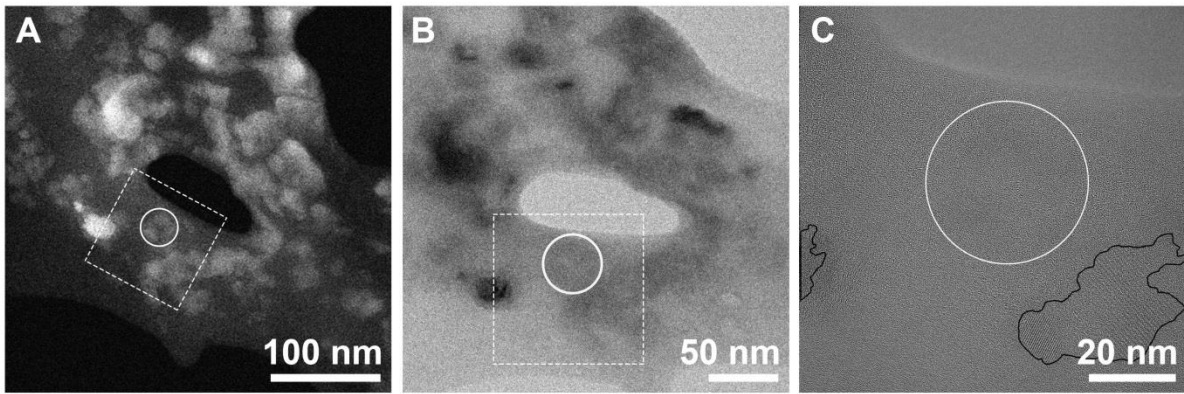
Supplementary Figures 1 to 7 and Supplementary Table 1



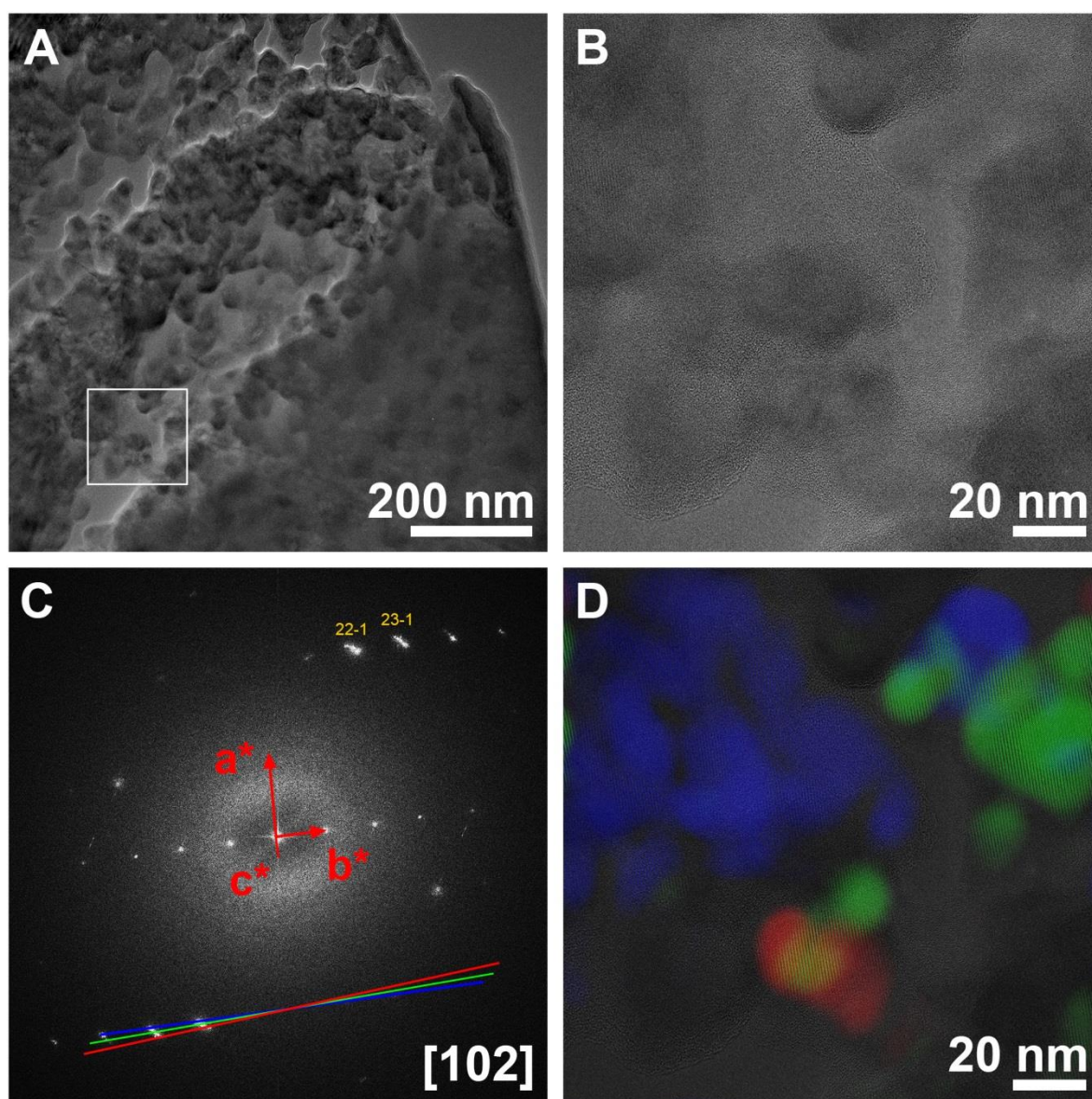
Supplementary Fig. 1. Position and aspect of hillocks. A) Three adjacent tablets of the same column showing the intervening hillocks and the typical porous structure of nacre tablets (HAADF). B) Hillocks protrude from both tablets through pores of the interlamellar membranes until they impinge on each other. Although there is physical separation between the two tablets, the crystalline lattice has the same orientation. The dotted line indicates a hypothetical cutting plane through the interlamellar membrane and the hillocks.



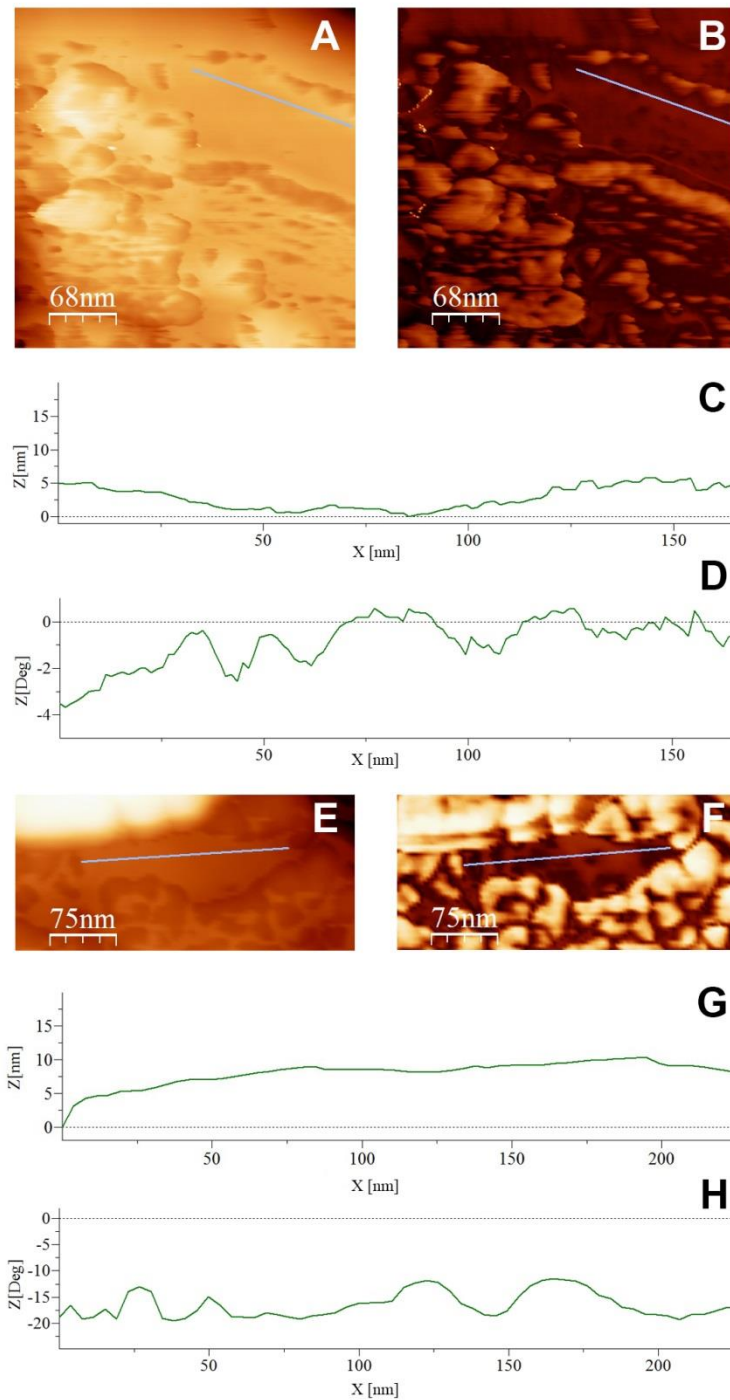
Supplementary Fig. 2. Amorphous border in an incipient nacre tablet. A) Overview of the tablet. B) Magnification of the area framed in A, showing the amorphous edge (2-5 nm) that surround the crystalline area. C, D) Amorphous edge before and after electron beam irradiation. After irradiation, the amorphous border becomes crystallized (acceleration voltage 200 kV, emission current 10 μ A).



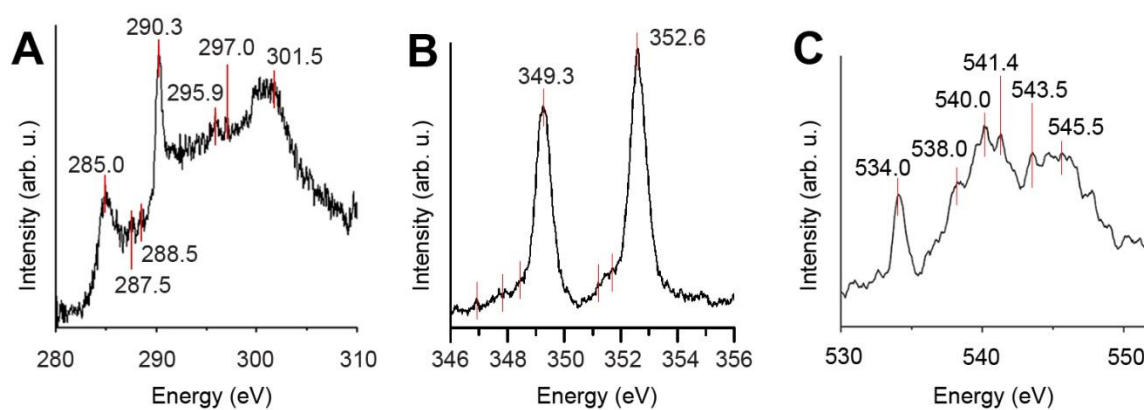
Supplementary Fig. 3. Image contrast comparison of ACC over an interlamellar membrane. A) Interlamellar membrane with calcium carbonate particles on its surface (HAADF). The highest contrast areas (white) have crystalline structure, whereas the lowest contrast areas do not. The circle encloses a low-contrast area. B) TEM image (using an objective aperture to enhance the contrast) of the same area. The crystalline areas are recognizable due to their high contrast (black). The low-contrast areas (light grey) have a non-crystalline structure, which is not discernible at this magnification. C) HRTEM from the area framed in A and B. Crystalline areas, recognizable by lattice fringes, are outlined in black. They are embedded in non-crystalline material (including the encircled area). ACC cannot be distinguished from the organic background in HRTEM because of their amorphous structures.



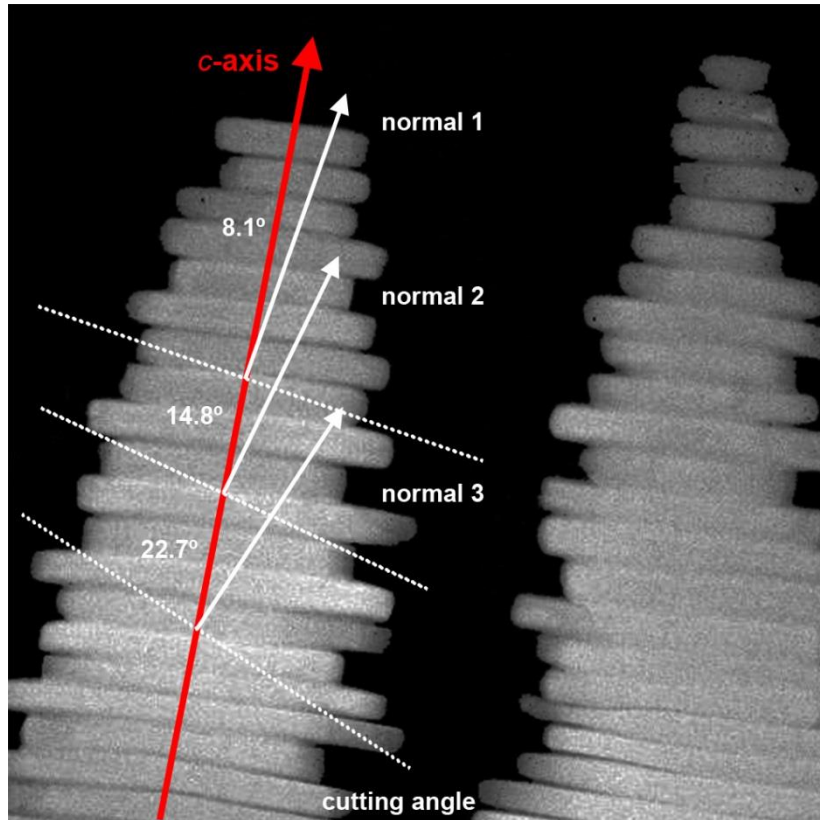
Supplementary Fig. 4. Orientation of crystalline nanodomains. A) General view of an incipient tablet where it is possible to see the agglomeration of globular nanoparticles. B) Enlargement of the area framed in A. Crystalline nanodomains are surrounded by amorphous material. C) FFT from the complete area in B. The particles are oriented along the $[102]$ zone axis, but the sample is slightly tilted, giving an incomplete diffraction pattern. The small arcs indicate a slight misalignment. D) The RGB reconstruction using the reflections of the $(22\bar{1})$ and $(23\bar{1})$ planes defines adjacent nanodomains misaligned by 1.2° from each other.



Supplementary Fig. 5. Differential information provided by tapping mode height and phase AFM images of nacre tablets. Two examples (A, B and E, F) of relatively flat areas where the topographic and phase contrasts do not coincide are provided. Height (A, E) and phase contrast (B, F) images are shown separately, together with identical profiles for height (C, G) and phase (D, H). Comparison between height and phase profiles (C-D, and G-H) demonstrates that phase changes are not due to the topography.



Supplementary Fig. 6. EEL Spectroscopy. A) Carbon k-edge. The three pre-peaks at 285.0, 287.5, and 288.5 eV, characteristic of organic material, are visible. B) Calcium $L_{2,3}$ -edge. The minor features that indicate the aragonite nature are marked with red bars. C) Oxygen K-edge characteristic of aragonite. All the peak positions denoted by vertical lines are commented on Table S1. Emission current 5 μ A, dispersion 0.025 eV. Savitzky-Golay smoothing was applied to both the C K- (10 pts) and the O K-edges (50 pts).



Supplementary Fig. 7. Diagram indicating how the cutting angle affects the orientation of the particles. When working without tilting the sample, the cutting angle largely determines the closest zone axis to index the particles. The normal to the cutting plane aligns in parallel to the optical axis of the microscope column, but does not necessarily coincide with a zone axis. Thus, the angle formed by the *c*-axis and the closest zone axis differs depending on the cutting angle. Only when the cut is exactly perpendicular to the nacre column growth axis, are we able to index the particles along the [001] zone axis. In our samples, the angles between the *c*-axis of the nacre column and the zone axis of the indexed particles varied from 0° to 24° ($n = 12$ slices). With a double tilt holder it is possible to tilt the sample so as to orient the particle along a particular zone axis, but this is a time-consuming procedure and therefore difficult to achieve in small crystalline domains without inducing beam damage.

Supplementary Table 1. Approximate transitions in carbon K-edge, calcium L_{2,3} edge and oxygen K-edge fine structure and assignment of peaks. Peaks in bold are the most characteristic for each edge.

Approximate Energy Loss (eV)	Peak assignment
Carbon	
285.0	C1s → π* in C=C
287.5	C1s → σ* in C-H
288.4	C1s → π* in C=O of carboxyl groups
290.3	C1s → π* transitions of carbon-oxygen bonds
295.5	C1s → π* transitions of carbon-oxygen bonds
298.3	C1s → π* transitions of carbon-oxygen bonds
301.5	C1s → σ* transitions of carbon-oxygen bonds
Calcium	
349.3	Ca L ₃ edge
352.6	Ca L ₂ edge
Oxygen	
534	O1s → π* transitions from C=O bonds
540	O1s → σ* transitions of the CO ₃ ⁻² group
541	O1s → σ* transitions of the CO ₃ ⁻² group
544	O1s → σ* transitions from the C=O
545.5	O1s → σ* transitions from the C=O



Crystallographic control on the substructure of nacre tablets



Antonio G. Checa^{a,*}, Harry Mutvei^b, Antonio J. Osuna-Mascaró^a, Jan T. Bonarski^c, Marek Faryna^c, Katarzyna Berent^c, Carlos M. Pina^d, Marthe Rousseau^e, Elena Macías-Sánchez^a

^a Departamento de Estratigrafía y Paleontología, Facultad de Ciencias, Universidad de Granada, Avenida Fuentenueva s/n, 18071 Granada, Spain

^b Department of Paleozoology, Swedish Museum of Natural History, Frescativägen 40, 11-418 Stockholm, Sweden

^c Institute of Metallurgy and Materials Science of the Polish Academy of Sciences, Reymonta. 25, 30-059 Kraków, Poland

^d Departamento de Cristalografía y Mineralogía, Facultad de Ciencias Geológicas, Universidad Complutense de Madrid, José Antonio Novais s/n, 28040 Madrid, Spain

^e CNRS, UMR7365, Ingénierie Moléculaire et Physiopathologie Articulaire (IMoPA), Faculté de Médecine, Université de Lorraine, 9 Avenue de la Forêt de Haye, 54505 Vandoeuvre-lès-Nancy, France

ARTICLE INFO

Article history:

Received 26 April 2013

Received in revised form 17 July 2013

Accepted 28 July 2013

Available online 6 August 2013

Keywords:

Nacre
Molluscs
Aragonite
Crystallography
Organic molecules

ABSTRACT

Nacre tablets of mollusks develop two kinds of features when either the calcium carbonate or the organic portions are removed: (1) parallel lineations (vermiculations) formed by elongated carbonate rods, and (2) hourglass patterns, which appear in high relief when etched or in low relief if bleached. In untreated tablets, SEM and AFM data show that vermiculations correspond to aligned and fused aragonite nanoglobules, which are partly surrounded by thin organic pellicles. EBSD mapping of the surfaces of tablets indicates that the vermiculations are invariably parallel to the crystallographic *a*-axis of aragonite and that the triangles are aligned with the *b*-axis and correspond to the advance of the {010} faces during the growth of the tablet. According to our interpretation, the vermiculations appear because organic molecules during growth are expelled from the *a*-axis, where the Ca–CO₃ bonds are the shortest. In this way, the subunits forming nacre merge uninterruptedly, forming chains parallel to the *a*-axis, whereas the organic molecules are expelled to the sides of these chains. Hourglass patterns would be produced by preferential adsorption of organic molecules along the {010}, as compared to the {100} faces. A model is presented for the nanostructure of nacre tablets. SEM and EBSD data also show the existence within the tablets of nanocrystalline units, which are twinned on {110} with the rest of the tablet. Our study shows that the growth dynamics of nacre tablets (and bioaragonite in general) results from the interaction at two different and mutually related levels: tablets and nanogranelles.

© 2013 Elsevier Inc. All rights reserved.

1. Introduction

The first crystallographic data on the nacre tablets were reported by Schmidt (1922), who concluded with optical microscopy that the *c*-axes of aragonite were perpendicular to tablets. In his subsequent papers, Schmidt (1923, 1924) used the outlines of tablets to infer the positions of {110}, {100} and {010} faces and, hence, the orientations of the *a*- and *b*-axes of the tablets. With the advent of the scanning electron microscopy, later authors e.g., (Grégoire, 1962; Wada, 1972; Mutvei, 1969, 1970, 1972a,b) refined that knowledge, but the basic schemes provided by Schmidt remained essentially unaltered.

X-ray diffraction techniques are useful for determining crystal orientation, but its application is hindered by the fact that they can only determine the orientation of groups of tablets in relatively wide areas (at least 250 μm in diameter). An additional handicap is that, due to the deep penetration of X-rays, the results combine data from dozens of superposed lamellae. Nevertheless, some insight can be gained. The distributions of maxima of pole figures indicate that in nacre tablets the *c*-axes are perpendicular to the main surfaces. Polarization-dependent imaging contrast (PIC), which is based on X-ray linear dichroism, has also been extensively applied to bivalve and gastropod nacres (Metzler et al., 2008; see review in Gilbert (2012)). It is a high resolution method (~20 nm), but can only detect changes in the *c*-axis, and not in the *a*- or *b*-axis. Additionally, the tablets of bivalves are known to be co-oriented, with the *b*-axis pointing in the local growth direction of the shell (Wada, 1961, 1972; Wise, 1970; Checa and Rodríguez Navarro, 2005; Rousseau et al., 2005). Tablet faces can sometimes be indexed by checking the shapes of the tablets against the overall orientation deduced from X-ray pole figures. Transmission electron microscopy (TEM) as well as electron

* Corresponding author. Fax: +34 958248528.

E-mail addresses: acheca@ugr.es (A.G. Checa), Harry.Mutvei@nrm.se (H. Mutvei), tay@ugr.es (A.J. Osuna-Mascaró), j.bonarski@imim.pl (J.T. Bonarski), marekfaryna@gmail.com (M. Faryna), marekfaryna@gmail.com (K. Berent), marekfaryna@gmail.com (C.M. Pina), rousseam@gmx.net (M. Rousseau), emacias@ugr.es (E. Macías-Sánchez).

back-scattered diffraction (EBSD) coupled to scanning electron microscopy (SEM) offer much higher resolution, but application is limited because the material has to be either sliced and thinned to tens of nm, in order to make the sample transparent to ions for TEM, or sectioned and finely polished, to eliminate differences in relief, to which the EBSD technique is very sensitive. Since, the 3D aspect is lost in this way, it is difficult to relate the shape of the tablets to the orientations found. Therefore, electron diffraction techniques have been routinely used to determine crystallographic orientations only of sectioned nacre tablets (e.g., Gries et al., 2009; Dalbeck et al., 2006), but not in plain view.

In view of the above explanation, the main information currently available on the crystallography of individual nacre tablets is not always reliable, particularly taking into account their high variety of shapes (Wise, 1970; Wada, 1972; Checa and Rodríguez-Navarro, 2005).

In a number of informative papers, (Mutvei, 1970, 1977, 1978, 1979, 1980, 1991; Mutvei and Dunca, 2008, 2010), using special etching protocols, revealed the existence of two kinds of etching features. First, in the tablets of bivalves, gastropods and *Nautilus*, a series of parallel lineations that appear, are inferred to be parallel to the *a*-axis of aragonite. The same patterns have been found in other examples of biogenic aragonite which were naturally or artificially etched: foliated and prismatic aragonite (Checa et al., 2009). Second, in some bivalves (*Mytilus*, *Nucula*, and *Unio*), Mutvei (1977) found two triangular sectors on each tablet joined by a vertex at the center of the tablet (hourglass-like), which were more resistant to etching than the rest of the tablet. According to the interpretation of Mutvei (1977, 1978, 1979, 1980, 1984), this pattern arose because each pseudo-hexagonal tablet was in fact composed by four twinned crystals, although this model (Mutvei, 1977, Fig. 1) was found to be incorrect by Akai and Kobayashi (1993).

The patterns revealed by Mutvei clearly have some bearing on the ultrastructure of nacre tablets and therefore are worth investigating. First, we needed to compile reliable data on the crystallography of individual nacre tablets in order to unequivocally relate the etching lineations and triangles to particular crystallographic directions. This was achieved by high-resolution diffraction techniques, particularly SEM-EBSD on the surfaces of the tablets. Additional information was gained from AFM and FESEM techniques. A model for the formation of the observed features was finally proposed.

2. Materials and methods

2.1. Treatments

Etching. Specimens were etched as originally described by Mutvei (1977, 1978, 1979), the protocol consisting of (1) cleaning the tablets with sodium hydroxide, followed by (2) etching the tablets and fixing the organic matrix at the same time with a mixture of glutaraldehyde and acetic acid. Specimens were treated at the University of Granada with the following protocol: Sodium hypochlorite 10% (step 1) for 2–30 min → glutaraldehyde 25% + acetic acid 1% in cacodylate buffer (step 2) for 2–10 min → sodium hypochlorite 1% (step 3) for 1–5 days (optional). In all cases, samples were washed repeatedly and oven dried. Bivalves: *Acila divaricata* (Turtle Island, Taiwan), *Nucula nitidosa* (Málaga coast, Spain), *Perna viridis* (loc. unknown, Indonesia), *Pinctada margaritifera* (French Polynesia), *Anodonta cygnea* (Mira, Portugal); Gastropods: *Bolma rugosa* (Granada coast, Spain), *Gibbula cineraria* (Quiberon, France), *Gibbula umbilicalis* (São Jacinto, Portugal); cephalopod: *Nautilus pompilius* (loc. unknown).

The shells had been preserved dry and clean and we studied nacre areas which were not marginal. Etching intensity was proportional to treatment time (compare Fig. 1A and E), but it also

varied between species undergoing the same treatment. No particular combination of times was found ideal for all species.

Additional observations were made at the Swedish Museum of Natural History on the nacre of the bivalve *Mytilus edulis* (coast of Sweden) and on the septal nacre of *N. pompilius* (Salomon Islands). These were treated with sodium hypochlorite (25 wt.%) followed by immersion in Mutvei's solution (1:1 mixture of glutaraldehyde and 1% acetic acid to which alcian blue is added; see Schöne et al., 2005) under constant stirring at 35–40 °C and then dehydrated in graded alcohol concentrations.

In all cases, the exact treatment times are provided in the corresponding figure captions.

Protease. Samples of the bivalves *A. divaricata* (Turtle Island, Taiwan), *Pinna nobilis* (coast of Almería, Spain) and *Pteria hirundo* (Fuengirola, Spain) were incubated in a solution of proteinase-K (US Biological) 0.1 or 0.2 g/ml for one to 2 h at 30 °C. After deproteination, samples were washed three times for ten min under constant stirring in saline solution (PBS) and additionally washed for ten min in milli-Q water. The samples were oven dried at 45 °C and stored for later SEM examination.

Untreated and bleached samples. The nacles of the above-mentioned species, as well as those of the bivalves *Atrina pectinata* (Fuengirola, Spain), *Anodonta anatina* (River Thames, UK), *Potomida littoralis* (loc. unknown, Spain), *Isognomon radiatus* (Olango Island, Philippines) and *Neotrigonia margaritacea* (Anxious Bay, Australia) were also investigated intact, although in some cases the tablets were cleaned of organic matter with commercial bleach (4% active Cl) from 2 to 10 min.

2.2. Scanning electron microscopy (SEM)

Samples were coated with carbon (Hitachi UHS evaporator) for FESEM observation (Zeiss Leo Gemini 1530 and Zeiss Auriga Cross-Beam Station) at the Centro de Instrumentación Científica (CIC) of the Universidad de Granada (Spain). Specimens in Figs. 1B and 2E were gold-coated and photographed with a SEM Hitachi S-4300, at the Natural History Museum, Stockholm (Sweden).

2.3. Electron back scattered diffraction (EBSD)

To relate the crystallographic data with the features detected on the surfaces of the tablets, samples were analyzed unpolished with the surfaces of the tablets placed as parallel as possible to the detector screen; only the organic matter was removed with 5% NaOCl from the samples prior to analysis. Since this technique is very sensitive to surface irregularities, the percentage of indexable patterns dropped drastically compared to polished samples, although the number of available data provided relevant information. We used two sets of equipment. First, we used an Inca Crystal (Oxford Instruments) detector coupled to a Gemini-1530 (Carl Zeiss) FESEM (CIC, Universidad de Granada). To avoid excessive charging, samples were coated with a thickness of 2 nm of carbon in a Baltec MED 020 electron beam evaporator. Samples of the nacre from the gastropod *G. cineraria* and from the bivalves *A. divaricata* and *P. margaritifera* were examined in this way. Also, samples of the nacre of the bivalves *Neotrigonia gemma* (off Cronulla, Australia) and *A. divaricata* were analyzed after sectioning and polishing. The second set of equipment was a TSL OIM detector coupled to FEI Field Emission Gun (FEG) SEM Quanta 3D microscope of the Institute of Metallurgy and Materials Science of the Polish Academy of Sciences (IMIM, Krakow, Poland). Operation in low vacuum mode made coating unnecessary. A special cone was attached to the SEM pole piece to minimize the so-called “skirt effect” of the primary electron beam and reduce the gas-path length. Analysis software (TSL OIM version 5.3) was used to post-process the EBSD measurements. All data with a confidence index (CI)

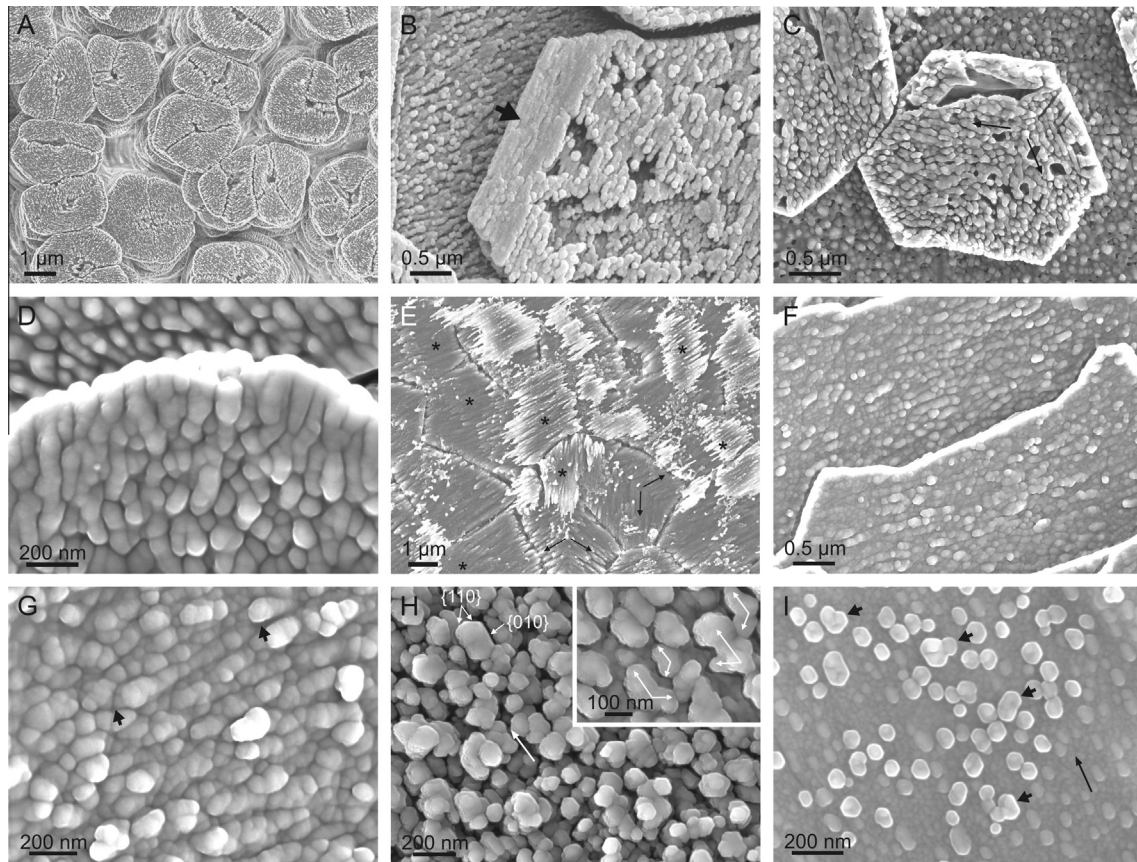


Fig. 1. (A). *Gibbula cineraria*, treated with Mutvei's protocol (step 1 for 10 min, step 2 for 5 min). Tablets are composed of several sectors with vermiculations at $\sim 120^\circ$. (B). *Nautilus pompilius* septal nacre, treated with 60 min with sodium hypochlorite and 120 min with Mutvei's solution. Note horizontal microlamination of the tablet, visible on the oblique edge (arrow). (C). *Pteria hirundo*, treated with protease (0.1 g/ml, 1 h). Note vermiculations diverging at 120° (arrows), indicative of twinning. (D). *Pteria hirundo*, treated with Protease (0.2 g/ml, 1 h). Close-up of the marginal area of a tablet showing vermiculations. (E). *Pinctada margaritifera*, treated with Mutvei's protocol (step 1 for 30 min, step 2 for 10 min, step 3 for five days). Vermiculations are arranged within planes, which in some instances (asterisks) are at an angle to the tablet surface. Some tablets display vermiculations at $\sim 120^\circ$ (double arrows). (F, G). *Nautilus pompilius*, bleached for 3 min. Note general arrangement of vermiculations. The close-up (G) clearly shows that the vermiculations are composed of fused carbonate nanogranules. The two arrows indicate the ends of one such vermiculation. (H). *Nautilus pompilius*, bleached for 2 min. The nanogranules on the surface of the tablet have pseudo-hexagonal shapes. The indexation is tentative. The inset shows several fused pseudo-hexagons which seem to diverge at $\sim 60^\circ$ or 120° (arrows), thus suggesting nanotwinning. The long arrows indicate the main orientation of the vermiculations. (I). *Pinctada margaritifera*, bleached for 10 min. Many nanocrystals, some of which are clearly composite or twinned (arrows), appear on the surface. The long arrow indicates the orientation of the *a*-axis (same specimen as in Fig. 3C).

below 0.1 were removed. For visualization purposes the following cleanup procedure was applied: (1) grain CI standardization, (2) neighbor orientation correlation, (3) neighbor CI correlation. The surfaces of nacre tablets of the bivalves *A. divaricata*, *Pt. hirundo*, and *P. nobilis* were examined with this second equipment.

2.4. Atomic force microscopy (AFM)

For AFM observations, a sample of the shell of *P. margaritifera* was polished, through a protocol adapted from Nouet et al. (2012). We used Struers water-grinding papers (DP Mol and DP Dur), followed by a thin polishing with Struers diamond pastes (3, 1, and 0.25 μm) and finally silica gel suspension (~ 3 h). The sample was etched in a 0.1 wt.% acetic acid with 3% glutaraldehyde solution for 8 s. It was later repolished, immersed in commercial bleach for ~ 90 s and dried before placing in the AFM sample holder. In addition, the surfaces of nacre tablets (bleached or protease-treated) of the following taxa were examined: the bivalves *P. margaritifera*, *P. nobilis*, *A. pectinata*, *A. divaricata*, *A. anatina*, *P. littoralis*, *I. radiatus*, *N. margaritacea*, and *Pt. hirundo*, the gastropod *B. rugosa*, and the cephalopod *N. pompilius*. Observations were made both in air and liquid using an AFM (Multimode Veeco) of the Centro Nacional de Microscopía Electrónica (Universidad Complutense

de Madrid, Spain). AFM images were recorded in both contact and tapping modes while displaying cantilever height, phase and amplitude signals. Recorded AFM images were subsequently analyzed using the Nanoscope 5.30r3sr3 and Nanotec WSxM. 2.1 software's (Horcas et al., 2009).

3. Results

3.1. SEM

All etched and protease-treated samples (with the exception of *P. nobilis*) displayed more or less conspicuous lineations, similar to those found by Mutvei (1977, 1978, 1979, 1980) and Mutvei and Dunca (2008, 2010) (Fig. 1A–D). Lineations ran mutually parallel across the entire tablet diameter. There appeared to be some direct relationship between etching time and lineation development, but some species proved more susceptible to the treatment than others. In non-etched samples, where the boundaries between lineations could be established with some precision, they range in width between ~ 40 and 120 nm. Lineations sometimes fused or divided, finally displaying a sinuous path. For this feature, we will call them vermiculations hereafter (Fig. 1A–G; one vermiculation is marked with arrows in Fig. 1G). Gastropod tablets are sometimes

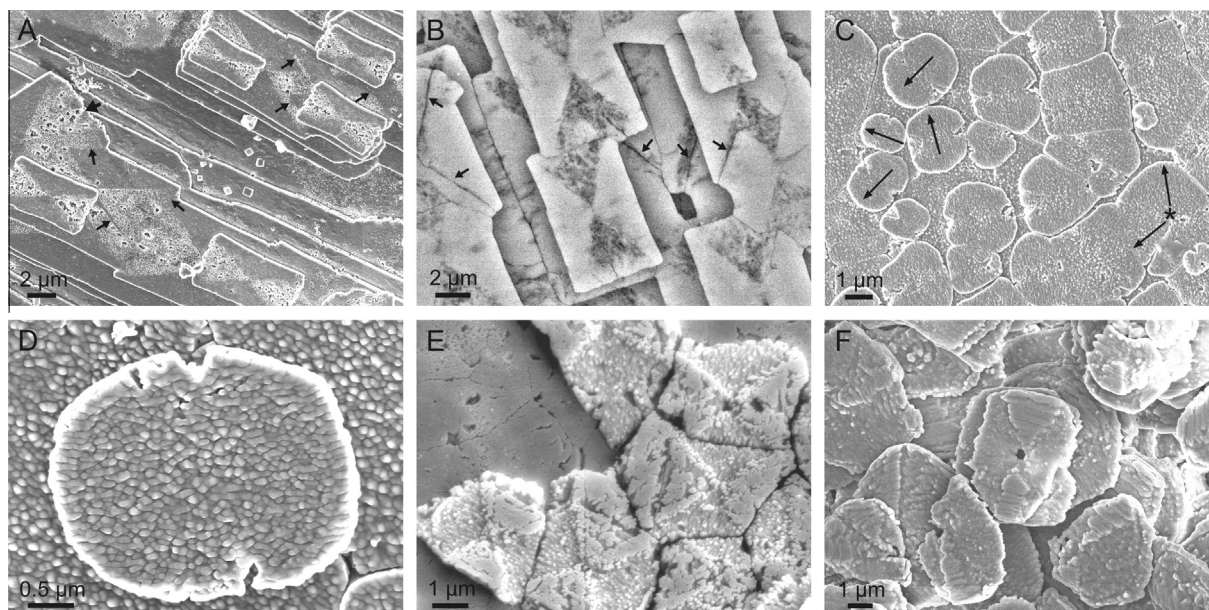


Fig. 2. (A, B) Rectangular nacre tablets of *Pinna nobilis*, treated with Protease (0.2 g/ml, 1 h). Secondary electron (A) and back scattered electron (B) images. Hourglass patterns (although no apparent vermiculations) form upon treatment. Interpenetration boundaries between tablets (arrows) are parallel to the long sides of triangles; they are particularly apparent in (B). (C and D) *Pteria hirundo*, treated with Protease (0.2 g/ml, 1 h). Treatment causes the formation of small triangular notches and well-developed vermiculations. In (C), the orientations of vermiculations in some tablets are marked with arrows; they have a three-rayed distribution, indicative of {110} twinning; the tablet marked with an asterisk has two sectors with vermiculations at 120°. (E) *Mytilus edulis*, treated with sodiumhypochlorite for 30 min and Mutvei's solution for 3 min. Note vermiculations in addition to hourglass features. (F) *Gibbula umbilicalis*, treated with Mutvei's protocol (step 1 for 30 min, step 2 for 10 min, step 3 for five days). Tablets are monocrystalline. This is the only case of a gastropod in which hourglass patterns (in high relief) were discerned.

divided into different sectors, with their vermiculations meeting at angles of $\sim 60^\circ$ or 120° (Fig. 1A). Nautilus (Fig. 1B) and bivalve tablets (Fig. 1C–E) were mostly undivided into sectors and only rarely consisted of two sectors at the most, with vermiculations at $\sim 120^\circ$.

In etched samples, vermiculations could be either strictly parallel or slightly inclined with respect to the surface of the tablet (Fig. 1E). In the latter case, the angles of inclination could not be estimated quantitatively.

Some of the untreated and slightly bleached (Fig. 1F and G) samples had more or less conspicuous surface relief consisting of aligned globular nanogranules (20–120 nm in diameter) running along the entire tablet diameter. The alignments showed exactly the same pattern of irregularities and sizes as the vermiculations observed in treated samples. In some instances, the nanogranules found at the very surface of the tablets grew in isolation and showed neat pseudo-hexagonal outlines; they can thus be qualified as nanocrystals (Fig. 1H and I). These nano-pseudo-hexagons might be larger than the nanogranules (up to 200 nm) and sometimes diverged at $\sim 60^\circ$ or 120° , suggesting that they are nanotwinned units (Fig. 1H, inset, and I).

The samples of *P. nobilis* and *Pt. hirundo* treated with protease displayed typical hourglass patterns in low relief. *P. nobilis* tablets have an unusual rectangular shape (shown by Wise, 1970; Wada, 1972) and the triangular areas were distributed along the maximum dimensions of the tablets with a corroded aspect (Fig. 2A and B). In *Pt. hirundo* these areas aligned with the short axis of the oval tablets, consisting of incipiently developed triangular notches (Fig. 2C and D). In *P. nobilis*, when two tablets in the same orientation met and intersected, the resulting boundary was invariably parallel to the sides of the triangles (Fig. 2A and B). In addition to dissolution triangles, the sample of *Pt. hirundo* showed a surface relief of vermiculations, with their overall elongation perpendicular to the axis joining the two triangular sectors (Fig. 2C and D). The similarly treated sample of *A. divaricata* only showed vermiculations of the kind found in etched samples. Similar

triangular hourglass sectors were visible in etched samples of *M. edulis* (Fig. 2E) and *G. umbilicalis* (Fig. 2F), differing in that the acute triangles developed in high relief due to preferential dissolution of the calcium carbonate instead of the organic fraction. In both cases, the treatment also produced vermiculations which, as in the protease-treated samples, ran perpendicular to the axis joining the acute triangles (Fig. 2E and F). It bears noting that triangular sectors were not found in the bivalves *P. viridis*, *A. divaricata*, and *A. cygnea*, in the gastropods *B. rugosa* and *G. cineraria*, and in the cephalopod *N. pompilus*. Mutvei (1977) reported them also in the bivalve *Nucula sulcata*.

3.2. SEM–EBSD

The results for tablets showing vermiculations, regardless of whether they were etched (*A. divaricata*, *N. nitidosa*), treated with protease (*Pt. hirundo*) or simply bleached (*P. margaritifera*), and regardless of whether or not they displayed triangular patterns at the same time, were all consistent. The 001 maxima of the associated pole figures were more or less centered on the diagrams and the 100 maxima were aligned with the vermiculations, or with the alignments of nanogranules (Fig. 3A). Some minor 100 maxima also appeared at $\sim 60^\circ$ from the main maxima. This implies that the *c*-axis was approximately perpendicular or at a high angle to the tablets and that the *a*-axis was parallel to the vermiculations. The 100 small maxima at 60° of the main maximum or maxima are indicative of some small crystals being twinned on {110}.

The map on the protease-treated sample of *P. nobilis* is, by far, the one which gave the best-quality results (Fig. 3B). Despite the lack of vermiculations, the triangular sectors were clearly aligned with the 010 maxima, i.e., the *b*-axis of aragonite. In addition to the main maxima (clustered within the NE and SW quadrants in Fig. 3B), there were two diffuse 010 maxima (NW quadrant), all three clusters being at $\sim 60^\circ$ to each other. One of these corresponds to dots in dark blue which appeared scattered onto the

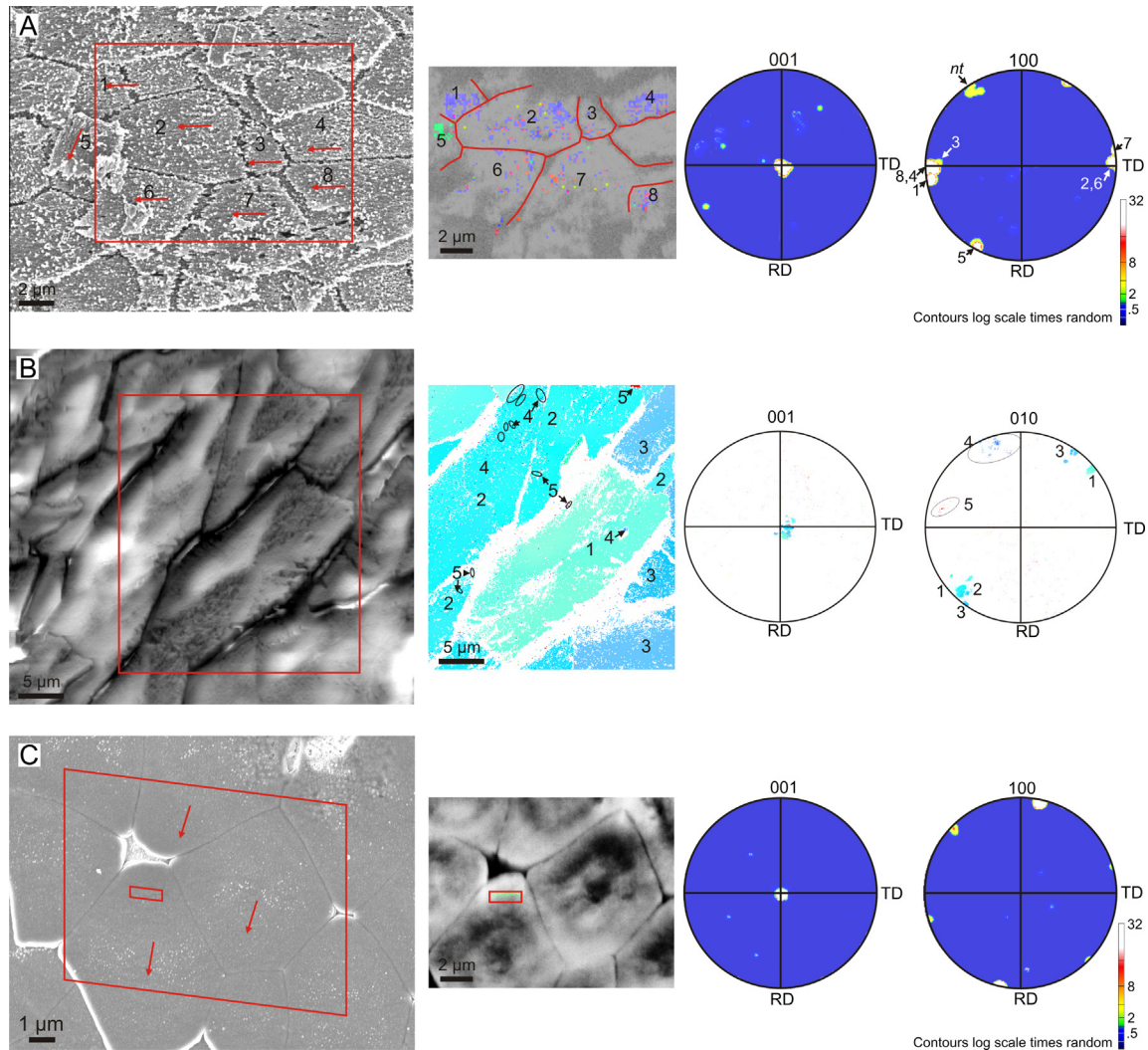


Fig. 3. EBSD maps of (A) *Acila divaricata*, treated with Mutvei's protocol (step 1 for 4 min, step 2 for 2 min), (B) *Pinna nobilis*, treated with protease (0.2 g/ml, 1 h), and (C) *Pinctada margaritifera*, bleached for 10 min. In all cases, the left image is the secondary electron image (with indication of the mapped area, red quadrangle, and orientation of the vermiculations, red arrows), the center image is the orientation map and the right diagrams are the 001 and 100 (A, C) or 010 (B) pole figures of aragonite. Numbers in (A) and (B) correspond to particular crystal domains or nanodomains. In all cases, the 001 maximum is at or close to the center of the diagram (i.e., the *c*-axis is perpendicular to the tablet surfaces). The maximum spread of 001 maxima for individual tablets is 6° (A), 12° (B) and 2° (C); the total spread for 001 maxima is 22° (A) and 25° (B). In (A) and (C), the distribution of 100 pole maxima implies that the *a*-axes of aragonite crystals are parallel to the vermiculations. In (A), an additional 100 small maximum (labelled *nt*) at ~60° to the other maxima indicates the existence of twinned nanocrystals. In (B), the *b*-axis is aligned with the triangular corrosion sectors; some scattered analyses (labeled 4 and 5 in the orientation map) have their 010 maxima at ~60° to the main maxima (1, 2 and 3) and can again be interpreted as nanocrystals twinned with the main tablets. RD, rolling direction; TD, transverse direction.

nacre tablets. The other maximum (made of red dots) was provided by a small tablet (top edge of the orientation map in Fig. 3B, labeled 5) together with additional scattered dots (Fig. 3B). Scattered dots in both dark blue and red are indicative of nanocrystals twinned on {110} with the tablets onto which they settled. Similar results were found on a bleached sample of *P. margaritifera* (Fig. 3C), in which the nanogranules were aligned with the *a*-axis and the triangular sectors made by nanogranules in high relief (a close-up view of those nanogranules in this same sample is shown in Fig. 11) were aligned with the *b*-axis. Note also two tiny additional 100 maxima at ~60° to the main maximum (aligned NNE-SSW), which imply that some nanogranules (independent dots not shown, but contained in the minor maxima) are related with the rest of the tablet (main maximum) by a {110} twinning.

3.3. AFM

The observation of tablets of the observed species has shown that the surfaces of tablets are in all cases made of round granules

with diameters similar to those observed with SEM (~20–120 nm) (Fig. 4). These units are surrounded by a pellicle (Fig. 4F, G, J and K), which in phase mode contrasts sharply with the granules (Fig. 4E, H and L). The pellicles had different degrees of preservation depending on the original state of the samples and on the treatments, from being almost continuous around the granules (e.g., Fig. 4K), to be reduced to a narrow rim along the depressed edges between and within grains (Fig. 4F and G). In some tablets the granules showed no preferential alignment, whereas in others they coalesced, forming alignments of variable width (between 40 and 120 nm) (Fig. 4). When the pellicles were poorly developed, they surrounded the aligned sets of granules (Fig. 4C, D, G and H). Etching revealed tablet elongation along the *a*-axis in the septal nacre of *N. pompilius* (Fig. 4A–F), while elongation along the same crystallographic axis was obtained via simultaneous analysis with FESEM-EBSD in the nacre of *Pt. hirundo* (Fig. 4G–L). For this reason, we know that in both cases the alignments of nanogranules detected with AFM are parallel to the crystallographic *a*-axis of the tablet.

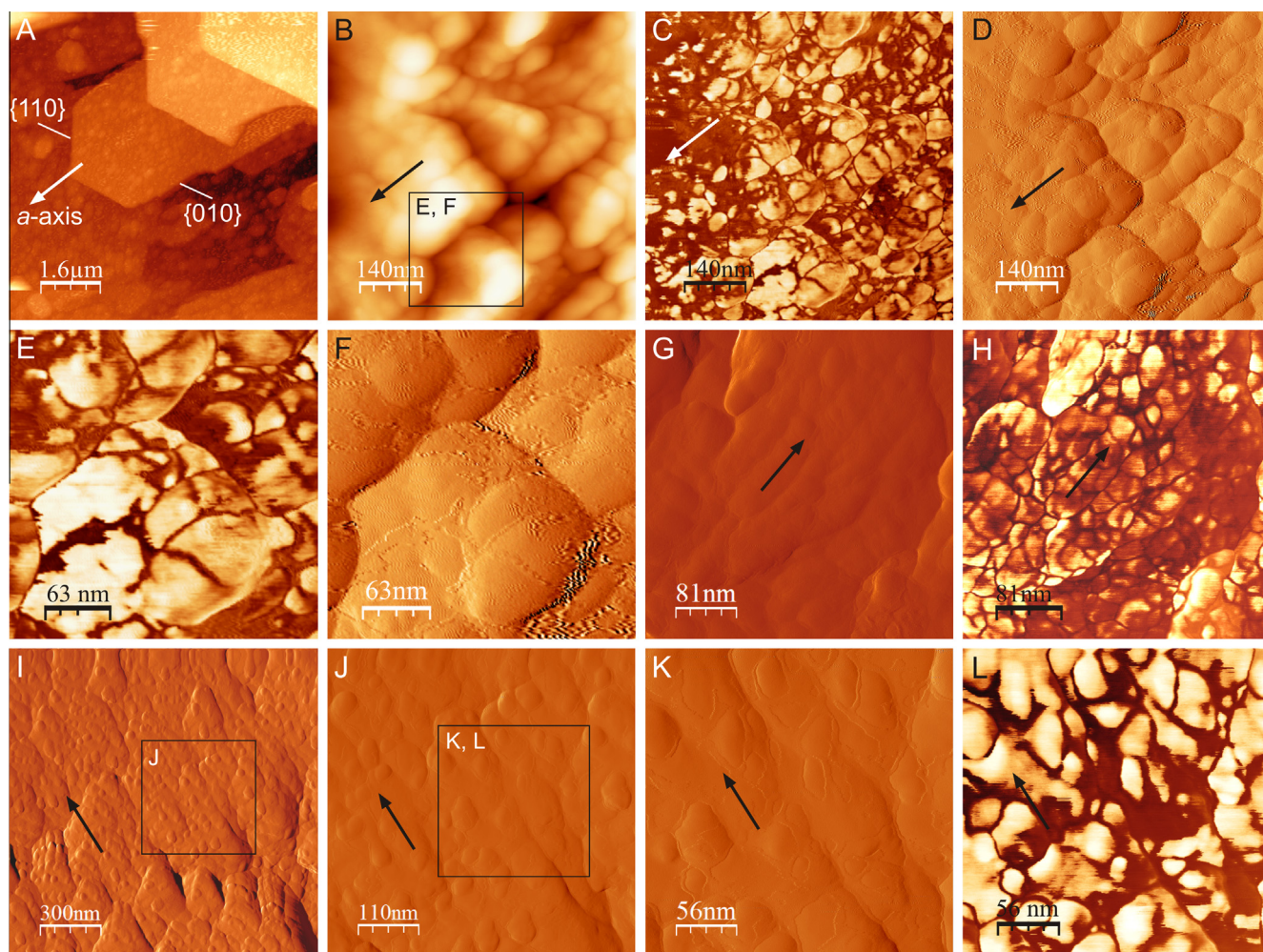


Fig. 4. AFM views of nacre. (A–E) Septal nacre of *Nautilus pompilius* (untreated). (A) Height image of three superposed tablets, with some faces indexed. (B–D) Height (B), phase (C) and amplitude (D) images of a close-up of (A). Note alignment of nanogranules in parallel to the *a*-axis of the tablet (arrows). (E and F) Phase (E) and amplitude (F) images of a magnified region of B (framed in B) showing the organic pellicles. (G–L) *Pteria hirundo*, treated with protease (0.2 g/ml, 1 h). (G, H) Amplitude (G) and phase image (H) of an area in which organic membranes are reduced to the boundaries between nanogranules, which appear fused and aligned (arrows). The distribution of organic membranes can be better appreciated in the phase image. (I–L) Amplitude (I–K) and phase (L) images showing progressive magnifications (frames) of an area in which nanogranules are aligned (arrows). Note relatively good preservation of organic nanomembranes in (K) and (L).

4. Discussion

Our FESEM and AFM observations showed that nacre tablets have a granular substructure, with granules ranging in size from 20 to 120 nm. Under FESEM, they have a globular aspect (Fig. 1E and F), although those located at the tablet surface sometimes tend to develop crystalline outlines (Fig. 1H and I). Similar nanocrystallites were observed on the surfaces of tablets by Metzler et al., 2008; Mutvei and Dunca, 2010) and were observed in sectioned mature nacre with TEM (Checa et al., 2011, figures 2 and 3), which excludes that they are artefacts arising during preparation (e.g., immersion in hypochlorite). AFM observations allow us to recognize that, in addition, the amalgamated granules are in turn surrounded by pellicles (Fig. 4E–H and J–L). This granular substructure was revealed for the first time by Dauphin (2001) in the nacre of *Nautilus*. Her AFM results were later amply confirmed with the same technique in the nacre of bivalves and gastropods (Li et al., 2004, 2006; Bruet et al., 2005; Rousseau et al., 2005; Wolf et al., 2012). Dauphin (2008) found this to be a general property of calcitic and aragonitic materials secreted by mollusks, as recognized later in a variety of other invertebrate animals (sponges, Sethmann et al., 2006; corals, Przeniosło et al., 2008; and

echinoderms, Seto et al., 2012) and even in fish otoliths (Dauphin and Dufour, 2008).

The great contrast in AFM tapping mode (phase imaging) between the pellicles and calcium carbonate granules (Fig. 4C, E, H and L) has led some authors to hypothesize that the former are organic in nature (e.g., Dauphin, 2001, 2006; Bruet et al., 2005; Rousseau et al., 2005; Li et al., 2006; Baronnet et al., 2008). Li et al. (2006) even showed how rotation of nanoparticles was favoured by the intervening polymer biofilms when nacre was subjected to tension. Based on former TEM data for nacre by Nassif et al. (2005), Seto et al. (2012) alternatively proposed that similar pellicles in the sea urchin test might consist of ACC. Our own bleaching experiments (unpublished observations) conducted with AFM are consistent with the organic nature of pellicles.

In many cases, the nanogranules tend to be preferentially aligned, thus forming vermiculations which are several μm in length (Fig. 1F and G). Our EBSD data (Fig. 3A and C) imply that the vermiculations observed in the treated samples (Fig. 1A–D) consistently occur along the *a*-axis of aragonite. This conclusion was previously reached by Mutvei (1970), although here we provide direct crystallographic evidence. Once the orientation of the *a*-axis is known, the crystal faces of the nanogranules can

tentatively be indexed (Fig. 1H). Given the coincidence in size, morphology, and crystallographic orientation, it is evident that the vermiculations observed in slightly bleached or untreated samples are the precursors of those observed in etched or protease-treated samples.

EBSD pole figures (Fig. 3) show that in our samples the c -axis is perpendicular or at a big angle to the surfaces of the tablet, although some deviation of the tablet surfaces with respect to the stage surface was expected. When several tablets are measured (Fig. 3A and B) the spread increases (to $>20^\circ$ in Fig. 3A and B), which implies that there are some differences in the orientation of the c -axes of neighboring tablets. Similar EBSD-based results have been obtained in the sectioned nacles of some bivalves by Dalbeck et al. (2006), England et al. (2007), Freer et al. (2010) and Griesshaber et al. (in press). Even higher spreads have been recorded with the PIC technique by the Gilbert group (Metzler et al., 2007; Gilbert et al., 2008; Olson et al., 2012, in press) in bivalves and gastropods, this being particularly high at the transition with the external shell and gradually diminishing away from this limit.

Based on our observations, we propose that nacre tablets consist of amalgamated vermiculations, i.e., fused calcium carbonate granules, which are aligned approximately parallel to the a -axis of the tablet. When the fused units grow isolated on the surface of the tablet, they are loosely packed and tend to develop crystalline shapes, because they grow within the proteinaceous material lining the interlamellar layer on both sides. These are the so-called hillocks or nanoasperities observed on the surfaces of nacre tablets (see Checa et al., 2011, figures 2 and 3) and correspond to the coarse granular layer of Mutvei and Dunca (2008, 2010). Vermiculations are bounded and separated from each other by nanometric organic pellicles, of the kind visualized with AFM (Fig. 4), although this may not be the only organic fraction involved. This substructure is most probably general to biogenic aragonite formed by mollusks, since similar etching lineations along the a -axis have also been reported in foliated and prismatic aragonite (Checa et al., 2009). These authors explained these features as the result of organic molecules being expelled from more mineralized zones along the a -axis by the crystallization pressure. This happens because, in the aragonite structure, there are chains of strong bonds along the a -axis, where the distance between the Ca atoms and the CO_3 groups is the shortest. The expelled organic molecules can easily be incorporated along the other crystallographic directions, where either the Ca– CO_3 distances are larger (b -axis) or

the stacked CO_3^{2-} groups are bonded by weak Van der Waals forces (c -axis) (Nelyubina and Lyssenko, 2012, and references therein). Our observations enable us to refine this model. Present-day models imply that biocrystals are formed from an amorphous calcium carbonate (ACC) precursor due to secondary nucleation (Politi et al., 2008; see also Weiner and Addadi, 2011; Gong et al., 2012, and Cartwright et al., 2012). In mollusks, good evidence has been presented by Nassif et al. (2005), who reported the existence of an ACC layer between 3 and 5 nm around nacre tablets of the abalone *Haliotis laevis*, and by Baronnet et al. (2008), who showed how an ACC cortex of ~ 40 – 60 nm carpets the growth surface of the calcitic prisms of the pearl oyster *P. margaritifera*. In line with the observations of Nudelman et al. (2007) (who observed similar granules attaching to the surface of the calcitic prisms of *Atrina rigida*) and of Baronnet et al. (2008) (who, by TEM, identified grains comparable to the granules seen under AFM crystallizing at the growth front of prisms from the ACC layer), we can consider the granules making up the vermiculations to be crystallization units (although this is not critical for our explanation). This idea is consistent with the model of Weiner and Addadi (2011, figure 3) for the crystallization of the sea urchin spicule. During growth, the connections between granules in the direction of the a -axis will go uninterrupted because organic molecules (probably exsolved from the ACC by the crystallization force) cannot easily enter the crystal lattice in this direction, but would be absorbed preferentially at the boundaries between granules corresponding to adjacent vermiculations, which is on the $\{010\}$ faces (perpendicular to the b -axis) (Fig. 5). Vermiculations have not been detected in some of the species (e.g., *P. nobilis*, Fig. 2A and B, or in the central part of the tablets of *Pt. hirundo*, Fig. 2C and D), which may be due to either defective treatment or (general or local) deficiency in the absorbable organic fraction.

SEM–EBSD data demonstrate that tablets displaying etching or bleaching triangles (Fig. 3), are single crystals, with the triangles being aligned with the a -axis if they develop upon acidic treatment (Fig. 2E and F), or with the b -axis if the triangles become excavated upon treatment with bleach or protease (Figs. 2A–D and 3B). The apical angle is $\sim 60^\circ$, which implies that the long sides of triangles correspond to traces of $\{110\}$ faces of aragonite. In *P. nobilis*, when two rectangular tablets collide and begin to interpenetrate, the boundaries thus formed are also parallel to the $\{110\}$ faces (Fig. 2A and B). This happens because the side relations of the rectangular tablets of this species agree to the a/b cell lattice relation of

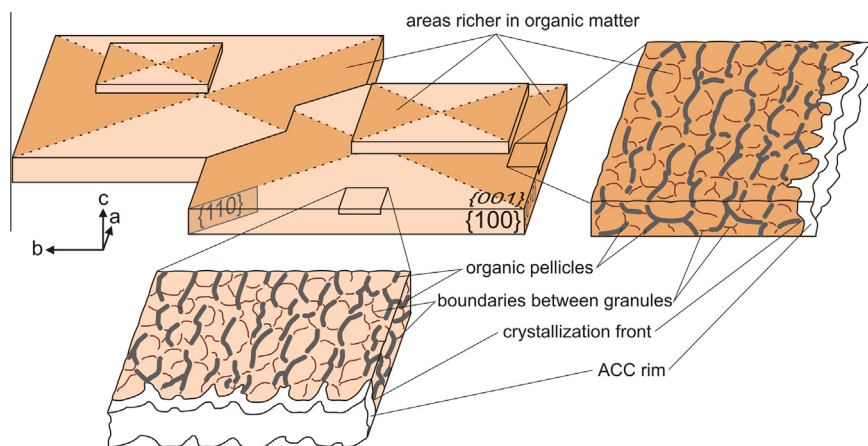


Fig. 5. Model for the internal structure of ideal nacre tablets. They are composed of four growth sectors, with the sectors corresponding to the growth of $\{010\}$ faces being richer in organic matter. Internally, the material is composed of calcium carbonate granules aligned in parallel to the crystallographic a -axis of aragonite (vermiculations). The organic pellicles surrounding the granules distribute preferentially around the lateral boundaries of the vermiculations. The sketch reproduces the case of the rectangular tablets of *Pinna nobilis*, and is based on the hypothesis that aragonite crystallizes from an amorphous calcium carbonate (ACC) precursor, with the granules being the crystallization units.

aragonite $4.959/7.968 = 0.622$. The fact that the triangular sectors remain in high relief upon etching (Fig. 2E and F), while they dissolve preferentially with protease (Fig. 2A–D), clearly implies that these areas are richer in organic matter than is the rest of the tablet. Since these triangles correspond to the advance of the {010} faces during the growth of the nacre crystal, the immediate implication is that there is preferential adsorption of organic molecules along the {010} faces. Since none of the two mentioned sets of faces display significant differences in charge density, the only reasons we can invoke are similar to the ones above to explain the vermiculations, i.e., differences in the length of the bonds along the *a*- and *b*-axes. The lack of etching or dissolution triangles in some of the treated species (see above) may imply that the absorbable proteinaceous component may be lacking.

The processes of preferential absorption of organic molecules along the *b*-axes, as compared to the more reduced absorption along the *a*-axes, commented on above to explain the observed vermiculations, could happen anywhere around the tablet, with the difference being that the amount of organic matter to be redistributed around growing nanogranules would be greater within the growth sectors of {010} faces than within the sectors of the {100} faces (Fig. 5). In this work, we focus on the nano-membranes examined with AFM, although this may not be the only organic component within the tablets. Younis et al. (2012) have imaged occluded macromolecules within the nacre of the mytilid *Perna* with TEM tomography, which are scattered within the crystals and have much larger dimensions than do the organic membranes observed with AFM. Similar organic components have been detected in the prismatic calcite of the bivalves *Pinctada* and *Atrina* (Okumura et al., 2010, 2011; Li et al., 2011). How the different intracrystalline organic components are absorbed is a matter of future study. Younis et al. (2012), Li et al. (2011) and Gilow et al. (2011) showed that the organic macromolecules are preferentially absorbed on the {001} planes in nacre and prismatic calcite due to preferential binding of the negatively charged residues of the acidic proteins to the positively charged {001} calcium planes. This might explain the horizontal microstratification sometimes shown by nacre tablets (Fig. 1B; see also Mutvei and Dunca, 2010).

Our EBSD data indicate the existence of nano-crystals twinned on {110} which appear scattered both on the surface (*N. pompilius*, Fig. 1H; *P. margaritifera*, Fig. 1I) and within the interior of tablets (etched tablets of *Nucula*, Fig. 3A, and protease-treated tablets of *Pinna*, Fig. 3B, as well as sectioned tablets of *Neotrigonia* and *Acila*, unpublished data). Nanocrystals of the external surface of tablets with the aspect of being twinned appear in the bleached nacre of *N. pompilius* (Fig. 1H) and *P. margaritifera* (Fig. 1I) under SEM. Nacre tablets and biocrystals in general are made of crystallographically oriented nanoparticles. Li and Huang (2009), Huang and Li (2012) and Zhang and Li (2012) identified nanoparticles via TEM and observed that, despite the fact that tablets of nacre diffract as single crystals, the constituent nanoparticles (which they implied are aggregation units) showed noticeable degrees of mutual misorientation (pseudo-single-crystal effect). The oriented arrangement could be transformed into a disoriented aggregate by either heat treatment (without phase change) or deformation (Huang and Li, 2012). Any hypothesis on the mode of aggregation and growth of biocrystals (e.g., from an amorphous precursor; see above), has to take into account the new degree of freedom that the existence of the recognized internal nanotwins implies.

Our study shows that the growth dynamics of nacre tablets (and bioaragonite in general) is much more complex than previously supposed, and that it results from the interaction at two different and mutually related levels: tablets and their constituent nanogranules (the monocrystal-polycrystal duality of Li and Huang, 2009; Huang and Li, 2012).

Acknowledgments

Antonio Sánchez-Navas (Dept. Mineralogy and Petrology, Univ. Granada) provided essential advice on the crystallography of nacre. A.G.C. A.J.O.-M., C.M.P. and E.M.-S. received funding from projects CGL2010-20748-CO2-01 of the Spanish Ministerio de Ciencia e Innovación and RNM6433 of the Andalusian Consejería de Innovación Ciencia y Tecnología, as well as from the Research Group RNM363 (latter institution) and the European COST Action TD0903 (EU). A.G.C. and C.M.P. also acknowledge the Centro de Instrumentación Científica (Univ. Granada) and the Centro Nacional de Microscopía Electrónica (Univ. Complutense Madrid), respectively, for the use of the equipment. Comments from two anonymous reviewers helped to improve the manuscript.

References

- Akai, J., Kobayashi, I., 1993. Microtwinning in the aragonitic shell layers of molluscs observed by TEM. In: Kobayashi, I., Mutvei, H., Sahni, A. (Eds.), *Structure, formation and evolution of fossil hard tissues*. Tokai University Press, Tokyo, pp. 47–54.
- Baronnet, A., Cuif, J., Dauphin, Y., Farre, B., Nouet, J., 2008. Crystallization of biogenic Ca-carbonate within organo-mineral micro-domains. Structure of the calcite prisms of the Pelecypod *Pinctada margaritifera* (Mollusca) at the submicron to nanometre ranges. *Mineral. Mag.* 72, 617–626.
- Bruet, B.J.F., Qi, H.J., Boyce, M.C., Panas, R., Tai, K., et al., 2005. Nanoscale morphology and indentation of individual nacre tablets from the gastropod mollusc *Trochus niloticus*. *J. Mater. Res.* 20, 2400–2419.
- Cartwright, J.H.E., Checa, A.G., Gale, J.D., Gebauer, D., Sainz-Díaz, C.I., 2012. Calcium carbonate polymorphism and its role in biomineralization: How many amorphous calcium carbonates are there? *Angew. Chem. Int. Ed.* 2012 (51), 2–13.
- Checa, A.G., Rodríguez-Navarro, A.B., 2005. Self-organisation of nacre in the shells of Pterioda (Bivalvia: Mollusca). *Biomaterials* 26, 1071–1079.
- Checa, A.G., Sánchez-Navas, A., Rodríguez-Navarro, A., 2009. Crystal growth in the foliated aragonite of monoplacophorans (Mollusca). *Cryst. Growth Des.* 9, 4574–4580.
- Checa, A.G., Cartwright, J.H.E., Willinger, M.-G., 2011. Mineral bridges in nacre. *J. Struct. Biol.* 176, 330–339.
- Dalbeck, P., England, J., Cusack, M., Lee, M.R., Fallick, A.E., 2006. Crystallography and chemistry of the calcium carbonate polymorph switch in *M. edulis* shells. *Eur. J. Mineral.* 18, 601–609.
- Dauphin, Y., 2001. Nanostructures de la nacre des tests de céphalopodes actuels. *Paléont. Z.* 75, 113–122.
- Dauphin, Y., 2006. Structure and composition of the septal nacreous layer of *Nautilus macromphalus* L. (Mollusca, Cephalopoda). *Zoology* 109, 85–95.
- Dauphin, Y., 2008. The nanostructural unity of mollusk shells. *Mineral. Mag.* 72, 243–246.
- Dauphin, Y., Dufour, E., 2008. Nanostructures of the aragonitic otolith of cod (*Gadus morhua*). *Micron* 39, 891–896.
- England, J., Cusack, M., Dalbeck, P., Pérez-Huerta, A., 2007. Comparison of the crystallographic structure of semi nacre and nacre by electron backscatter diffraction. *Cryst. Growth Des.* 7, 307–310.
- Freer, A., Greenwood, D., Chung, P., Claire, J.L., Pannell, C.L., Cusack, M., 2010. Aragonite prism-nacre interface in freshwater mussels *Anodonta anatina* (Linnaeus, 1758) and *Anodonta cygnea* (L. 1758). *Cryst. Growth Des.* 10, 344–347.
- Gilbert, P.U.P.A., 2012. Polarization-dependent Imaging Contrast (PIC) mapping reveals nanocrystal orientation patterns in carbonate biominerals. *J. Electron Spectrosc. Related Phenom.* 185, 395–405.
- Gilbert, P.U.P.A., Metzler, R.A., Zhou, D., Scholl, A., Doran, A., Young, A., Kunz, M., Tamura, N., Coppersmith, S.N., 2008. Gradual ordering in red abalone nacre. *J. Amer. Chem. Soc.* 130, 17519–17527.
- Gilow, C., Zolotoyabko, E., Paris, O., Peter Fratzl, P., Aichmayer, B., 2011. Nanostructure of biogenic calcite crystals: A view by small-angle X-ray scattering. *Cryst. Growth Des.* 11, 2054–2058.
- Gong, Y.U.T., Killian, C.E., Olson, I.C., Appathurai, N.P., Amasino, A.L., Martin, M.C., Holt, L.J., Wilt, F.H., Gilbert, P.U.P.A., 2012. Phase transitions in biogenic amorphous calcium carbonate. *Proc. Natl. Acad. Sci. USA* 109, 6088–6093.
- Grégoire, C., 1962. On submicroscopic structure of *Nautilus* shell. *Bull. Inst. Roy. Sci. Nat. Belgique* 38, 1–71.
- Gries, K., Kröger, R., Kübel, C., Schowalter, M., Fritz, M., Rosenauer, A., 2009. Correlation of the orientation of stacked aragonite platelets in nacre and their connection via mineral bridges. *Ultramicroscopy* 109, 230–236.
- Griesshaber, E., Schmahl, W.W., Ubhi, H.S., Huber, J., Nindiyasari, F., Maier, B., Ziegler, A., in press. Homoepitaxial meso- and microscale crystal co-orientation and organic matrix network structure in *Mytilus edulis* nacre and calcite. *Acta Biomater.* (available online 27 July 2013).
- Horcas, I., Fernández, R., Gómez-Rodríguez, J.M., Colchero, J., Gómez-Herrero, J., et al., 2009. WSXM: A software for scanning probe microscopy and a tool for Nanotechnology. *Rev. Sci. Instrum.* 78, 013705.

- Huang, Z.W., Li, X.D., 2012. Order-disorder transition of aragonite nanoparticles in nacre. *Phys. Rev. Lett.* 109, 025501.
- Li, X.D., Huang, Z.W., 2009. Unveiling the formation mechanism of pseudo-single crystal aragonite platelets in nacre. *Phys. Rev. Lett.* 102, 075502.
- Li, X.D., Chang, W.C., Chao, Y.J., Wang, R.Z., Chang, M., 2004. Nanoscale structural and mechanical characterization of a natural nanocomposite material - the shell of red abalone. *Nano Lett.* 4, 613–617.
- Li, X.D., Zhu, Z.-H., Wang, R.Z., 2006. In situ observation of nanograin rotation and deformation in nacre. *Nano Lett.* 6, 2301–2304.
- Li, H., Xin, H.L., Kunitake, M.E., Keene, E.C., Muller, D.A., et al., 2011. Calcite prisms from mollusk shells (*Atrina rigida*): Swisscheese-like organic-inorganic single-crystal composites. *Adv. Funct. Mater.* 21, 2028–2034.
- Metzler, R.A., Abrecht, M., Olabisi, R.M., Ariosa, D., Johnson, C.J., Frazer, B.H., Coppersmith, S.N., Gilbert, P.U.P.A., 2007. Architecture of columnar nacre, and implications for its formation mechanism. *Phys. Rev. Lett.* 98, 268102.
- Metzler, R.A., Zhou, D., Abrecht, M., Chiou, J.-W., Guo, J., Ariosa, D., Coppersmith, S.N., Gilbert, P.U.P.A., 2008. Polarization-dependent imaging contrast in abalone shells. *Phys. Rev. B* 77, 064110.
- Mutvei, H., 1969. On the micro- and ultrastructures of the conchiolin in the nacreous layer of some recent and fossil molluscs. *Stockholm Contr. Geol.* 22, 1–17.
- Mutvei, H., 1970. Ultrastructure of the mineral and organic components of molluscan nacreous layers. *Biomaterialization* 2, 49–72.
- Mutvei, H., 1972a. Ultrastructural relationships between the prismatic and nacreous layers in *Nautilus* (Cephalopoda). *Biomaterialization* 4, 81–86.
- Mutvei, H., 1972b. Formation of nacreous and prismatic layers in *Mytilus edulis* L. (Lamellibranchiata). *Biomaterialization* 6, 96–100.
- Mutvei, H., 1977. The nacreous layer in *Mytilus*, *Nucula* and *Unio* (Bivalvia). *Calcif. Tissue Res.* 24, 11–18.
- Mutvei, H., 1978. Ultrastructural characteristics of the nacre in some gastropods. *Zool. Scripta* 7, 287–296.
- Mutvei, H., 1979. On the internal structure of the nacreous tablets in molluscan shells. *Scanning Electron Microsc. II* 1979, 457–462.
- Mutvei, H., 1980. The nacreous layer in molluscan shells. In: Omori, M., Watabe, N. (Eds.), *The Mechanisms of Biomineralization in Animals and Plants*. Tokai University Press, Tokyo, pp. 49–56.
- Mutvei, H. 1984. Ultrastructural research on molluscan nacre. In: *Proceedings of the 27th International Geological Congress Moscow, Russia*. VNU Science Press BV, Utrecht, The Netherlands, pp. 111–124.
- Mutvei, H., 1991. Using plasma-etching and proteolytic enzymes in studies of molluscan shell ultrastructure. In: Suga, S., Nakahara, H. (Eds.), *Mechanisms and Phylogeny of Mineralization in Biological Systems*. Springer, Tokyo, pp. 157–160.
- Mutvei, H., Dunca, E., 2008. Structural relationship between interlamellar organic sheets and nacreous tablets in gastropods and cephalopod *Nautilus*. *Paläontol. Z.* 82, 85–94.
- Mutvei, H., Dunca, E., 2010. Crystalline structure, orientation and nucleation of the nacreous tablets in the cephalopod *Nautilus*. *Paläontol. Z.* 84, 457–465.
- Nassif, N., Pinna, N., Gehrke, G., Antonietti, M., Jäger, C., et al., 2005. Amorphous layer around aragonite platelets in nacre. *Proc. Natl. Acad. Sci. USA* 102, 12653–12655.
- Nelyubina, Y.V., Lyssenko, K.A., 2012. From “loose” to “dense” crystalline phases of calcium carbonate through “repulsive” interactions: An experimental charge-density study. *Chem. Eur. J.* 18, 12633–12636.
- Nouet, J., Baronnet, A., Howard, L., 2012. Crystallization in organo-mineral microdomains in the crossed-lamellar layer of *Nerita undata* (Gastropoda, Neritopsina). *Micron* 43, 456–462.
- Nudelman, F., Chen, H.H., Goldberg, H.A., Weiner, S., Addadi, L., 2007. Lessons from biomineralization: comparing the growth strategies of mollusc shell prismatic and nacreous layers in *Atrina rigida*. *Faraday Discuss.* 136, 9–25.
- Okumura, T., Suzuki, M., Nagasawa, H., Kogure, T., 2010. Characteristics of biogenic calcite in the prismatic layer of a pearl oyster, *Pinctada fucata*. *Micron* 41, 821–826.
- Okumura, T., Suzuki, M., Nagasawa, H., Kogure, T., 2011. Microstructural variation of biogenic calcite with intracrystalline organic macromolecules. *Cryst. Growth Des.* 12, 224–230.
- Olson, I.C., Kozdon, R., Valley, J.W., Gilbert, P.U.P.A., 2012. Mollusk shell nacre ultrastructure correlates with environmental temperature and pressure. *J. Amer. Chem. Soc.* 134, 7351–7358.
- Olson, I.C., Metzler, R.A., Tamura, N., Kunz, M., Killian, C.E., Gilbert, P.U.P.A. in press. Crystal lattice tilting in prismatic calcite. *J. Struct. Biol.* (available online 24 June 2013).
- Politi, Y., Metzler, R.A., Abrecht, M., Gilbert, B., Wilt, F.H., et al., 2008. Transformation mechanism of amorphous calcium carbonate into calcite in the sea urchin larval spicule. *Proc. Natl. Acad. Sci. USA* 105, 17362–17366.
- Przenioslo, R., Stolarski, J., Mazur, M., Brunelli, M., 2008. Hierarchically structured scleractinian coral biocrystals. *J. Struct. Biol.* 161, 74–82.
- Rousseau, M., Lopez, E., Stempfflé, P., Brendlé, M., Franke, L., et al., 2005. Multiscale structure of sheet nacre. *Biomaterials* 26, 6254–6262.
- Schmidt, W.J., 1922. Über den Aufbau der Schale von *Nucula*. *Archiv Mikroskop. Anat.* 96, 171–181.
- Schmidt, W.J., 1923. Bau und bildung der Perlmuttermasse. *Zool. Jahrb. Zool. Abt.* 96, 1–148.
- Schmidt, W.J., 1924. Die Bausteine des Tierkörpers in polarisiertem Lichte. Verlag F. Cohen, Bonn.
- Schöne, B.R., Dunca, E., Fiebig, J., Pfeiffer, M., 2005. Mutvei's solution: an ideal agent for resolving microgrowth structures in biogenic carbonates. *Palaeogeogr. Palaeoclimatol. Palaeoecol.* 228, 149–166.
- Sethmann, I., Hinrichs, R., Wöhrheide, G., Putnis, A., 2006. Nano-cluster composite structure of calcitic sponge spicules – A case study of basic characteristics of biominerals. *J. Inorg. Biochem.* 100, 88–96.
- Seto, J., Ma, Y., Davis, S.A., Meldrum, F., Gourrier, A., et al., 2012. Structure-property relationships of a biological mesocrystal in the adult sea urchin spine. *Proc. Natl. Acad. Sci. USA* 109, 3699–3704.
- Wada, K., 1961. Crystal growth of molluscan shells. *Bull. Natl. Pearl Res. Lab.* 7, 703–828.
- Wada, K., 1972. Nucleation and growth of aragonite crystals in the nacre of some bivalve molluscs. *Biomaterialization* 6, 141–159.
- Weiner, S., Addadi, L., 2011. Crystallization pathways in biomineralization. *Annu. Rev. Mater. Res.* 41, 21–40.
- Wise, S.W., 1970. Microarchitecture and mode of formation of nacre (mother of pearl) in pelecypods, gastropods and cephalopods. *Eclogae geol. Helv.* 63, 775–797.
- Wolf, S.E., Lieberwirth, I., Natalio, F., Bardeau, J.-F., Delorme, N., Emmerling, F., Barrea, R., Kappl, M., Marin, F., 2012. Merging models of biomineralisation with concepts of nonclassical crystallisation: is a liquid amorphous precursor involved in the formation of the prismatic layer of the Mediterranean Fan Mussel *Pinna nobilis*? *Faraday Discuss.* 159, 433–448.
- Younis, S., Kauffmann, Y., Bloch, L., Zolotoyabko, E., 2012. Inhomogeneity of nacre lamellae on the nanometer length scale. *Cryst. Growth Des.* 19, 4574–4579.
- Zhang, G.S., Li, X.D., 2012. Uncovering aragonite nanoparticle self-assembly in nacre – A natural armor. *Cryst. Growth Des.* 12, 4306–4310.

The transport system of nacre components through the surface membrane of gastropods

Elena Macías-Sánchez^{1,a}, Antonio G. Checa^{1,b*} and Marc G. Willinger^{2,c}

¹Department of Stratigraphy and Palaeontology, Faculty of Sciences, Granada, Spain

²Electron Microscopy Group, Department of Inorganic Chemistry, Fritz Haber Institute, Max-Planck Society, Berlin, Germany

^aemacias@ugr.es, ^bacheca@ugr.es, ^cwillinger@fhi-berlin.mpg.de

* Corresponding author

Keywords: biomineralization, molluscs, vesicles, calcium

Abstract

The surface membrane is a lamellar structure exclusive of gastropods that is formed during the shell secretion. It protects the surface of the growing nacre and it is located between the mantle epithelium and the mineralization compartment. At the mantle side of the surface membrane numerous vesicles provide material, and at the nacre side, the interlamellar membranes detach from the whole structure. Components of nacre (glycoproteins, polysaccharides and calcium carbonate) cross the structure to reach the mineralization compartment, but the mechanism by which this occurs is still unknown. In this paper we have investigated the ultrastructure of the surface membrane and the associated vesicle layer by means of Transmission Electron Microscopy. Electron Energy Loss Spectroscopy and Energy-dispersive X-ray Spectroscopy were used for elemental analysis. The analyses revealed the concentration of calcium in the studied structures: vesicles, surface membrane, and interlamellar membranes. We discuss the possible linkage of calcium to the organic matrix.

1. Introduction

Nacre is a biomineral with a characteristic “brick and mortar” arrangement, which forms the internal layers of the shells of many molluscs. It is produced by the mantle, the epithelium which lines the shell internally. The mantle epithelium secretes parallel membranes (the interlamellar membranes, ILMs) which are mainly composed of glycoproteins and polysaccharides [1,2] between which the aragonite crystals grow. Constituting only 5 % of the dry weight, the organic material confers a resistance to fracture significantly superior to its inorganic counterpart [3]. Bevelander & Nakahara [4,5] were the first to highlight the importance of these organic sheets in the formation of the molluscan structures.

In bivalves, ILMs are secreted in a confined liquid-filled space (~100-200 nm), known as the extrapallial space, and nacre grows in a step-like manner [4,6]. However, in gastropods nacre tablets are stacked in towers [7], forming pyramids. In the seventies, the acceptance of the hypothesis for the previous formation of lamellar sheets was problematic [8,9] mostly due to the possible disturbance of the organic structure caused by mantle movement. With the aid of Transmission Electron Microscopy (TEM) it was possible to observe the wall-like organic structures [10]. The ILMs derive from a dense surface sheet (the surface membrane, SM) that covers the surface of the nacre mineralization compartment [10]. The side of the SM adjacent to the mantle epithelium is composed of a dense organic material at its outermost area and by a compressed arrangement of membranes at the innermost region [10]. The SM may provide a resistant wall to disturbances caused by mantle movement [11,12]. At the nacre side of the SM, fresh ILMs progressively detach

from it [12,13] and position with a typical spacing of about 500 nm [6]. ILMs separate progressively from the SM in a zipper-like manner [13].

Since the first description by Nakahara, the SM passed unnoticed until Cartwright & Checa [13] realized that it is widespread in nacre-secreting gastropods. Checa *et al.* [12] highlighted the existence of vesicles adhered to the SM at the mantle side. They are round bodies with different morphologies, from spherical to strongly compressed, which seem to fuse with the SM. Their walls are electron-dense and have a mean thickness of 10-15 nm. In this way, the SM seems to be formed by the addition of organic vesicles to its mantle-side surface, which gradually integrate into the whole structure.

The SM maintains a constant thickness due to the strict balance between components acquired via vesicle addition and those lost due to the formation of the ILMs [12]. Therefore, it is in a dynamic equilibrium. At the same time, with the incorporation of material and its concomitant loss, the SM moves in an apertural direction, by keeping pace with the animal's growth rate.

We have studied the SM and its vesicle layer in *Phorcus turbinatus* (Trochidae, Vetigastropoda). The growth of the nacreous layer takes place close to the margin at the shell aperture [14,15]. It is preceded by a fibrous prismatic layer and followed and covered internally by an aragonitic structure of nacreous aspect (Fig. 1).

We hypothesize that vesicles act as a transport system of the components of nacre to the biomineralization compartment. Our aim is to identify the constituents of those vesicles (proteins, chitin, calcium carbonate, etc.) and characterize, as far as possible, the form or phase in which they travel (monomers or polymers in the case of chitin, and the type of polymorph/polyamorph/ions in the case of calcium carbonate).

2. Methods

Sample preparation

Different preparative protocols were used. Glutaraldehyde fixation followed by osmium tetroxide provides an excellent quality of tissue preservation for the observation of the ultrastructure under the TEM [16]. Nevertheless, it is carried out in an aqueous media, which might wash out the ion content of the sample. Consequently we avoided it for elemental analysis. Testing the content of soft elements in subcellular compartments is challenging due to the difficulty in maintaining the original element distribution. Important advances have been made in cryo-microscopy in the last decade, mostly focusing on cell cultures and single particles. Techniques used here are still in the experimental stages, since they result from adaptations of cryo-techniques not normally used on mineralized samples.

Chemical fixation

Specimens of *Phorcus turbinatus* were collected in Benalmádena (Málaga, SE Spain). Immediately after capture, they were fixed in cacodylate-buffered glutaraldehyde 2.5%. Fragments of the SM area were fractured under the binocular microscope, postfixed in osmium tetroxide, and embedded in embedding resin EMbed 812 (EMS).

Quick-freeze and freeze-drying

Juvenile specimens of *Phorcus turbinatus* were collected in La Herradura (Granada, SE Spain). The specimens were frozen in liquid nitrogen following collection and maintained in N₂ until they were freeze-dried. Quick-freezing immobilizes all molecules in a cell within milliseconds. It is possible to achieve up to 2-20 µm of good freezing depth. Beyond that, ice crystals form and destroy the tissue. For freeze-drying, the initial temperature (-170°C) was raised slowly at an

average pressure of 75 millitorr (Flexi-Dry MP) and at the end of the drying cycle (2 days), when room temperature was reached, the specimens were removed and stored at 4°C.

Fragments from the SM area were cut under the binocular microscope, postfixed in 1% osmium tetroxide at 4°C, dehydrated through a series of ethanol solutions and embedded in epoxy resin (EMbed 812). With the aim of comparing the effect of the different fixatives, another set of samples was prepared by avoiding osmium tetroxide postfixation.

Slices were cut (PowerTome Ultramicrotome) at a small angle relative to the surface (less than 10°, Fig. 1 right), thus trying to maximize the area of the cut through the vesicle layer and the SM. The slices were laid in copper grids with lazy carbon to stabilize them under the electron beam. The observations were made at 200 kV in a Philips CM200 and at 300 kV in a FEI Titan.

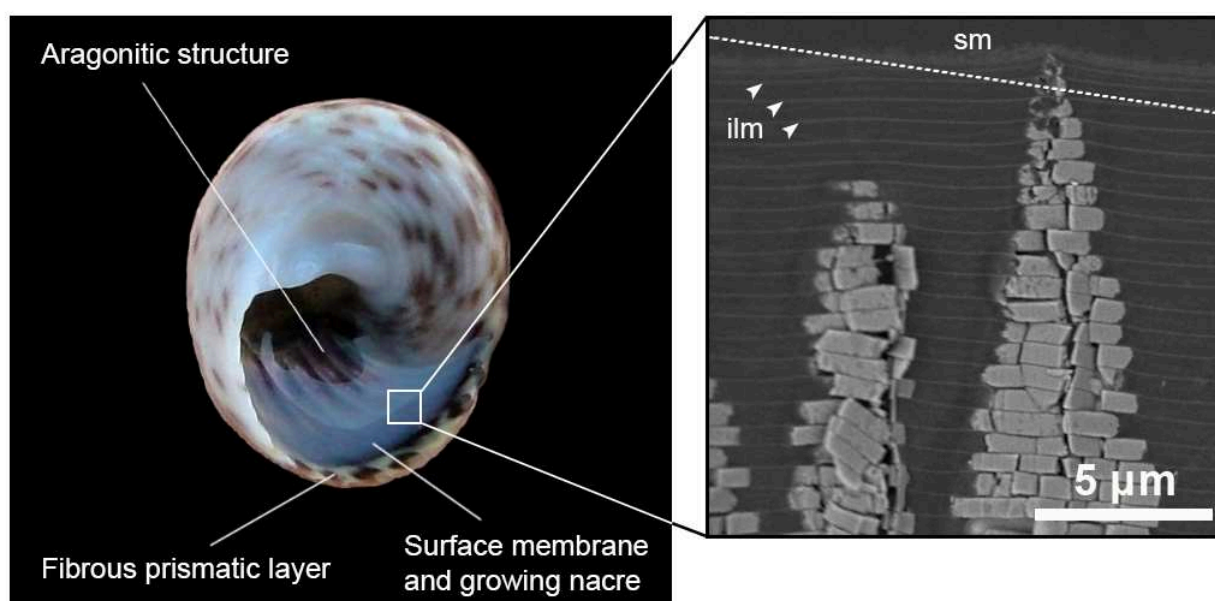


Fig. 1. Left, specimen of *Phorcus turbinatus* indicating the location of the surface membrane and the growing nacre (sampled area) in relation to the other microstructures present at the shell aperture. Right, SEM image of an ultramicrotome slice perpendicular to the shell surface, where it is possible to distinguish the SM (sm), the interlamellar membranes (ilm) and two towers of growing nacre. The dotted line indicates the approximate angle of the ultramicrotome cuts carried out in this study.

Elemental analysis

Once the vesicle layer was localized under the TEM, our aim was to know if there was calcium associated with these vesicles. We used two elemental analysis techniques alternatively; Electron Energy Loss Spectroscopy (EELS) and Energy-dispersive X-ray Spectroscopy (EDS). The former measures the energy lost by the beam electrons when they interact with the sample, which corresponds with the energy needed to remove one electron from the inner-shell of a particular atom. This is characteristic of each element, and allows us to identify it [17]. EELS is a very powerful technique, since it can detect concentrations of an element greater or equal to 1%. It is highly sensitive to relatively low atomic number elements, where the edges are clear and the energy loss is easy to distinguish. Spectral energy resolution in EELS is much higher than in EDS (about 1 eV in EELS as opposed to about 125-150 eV in EDS). But what makes EELS an extraordinary useful tool is its capacity to assess atomic composition, chemical bonding and valence state.

EELS spectra were obtained using a post column energy filter spectrometer (GIF Quantum Energy Filter, Gatan) at 200 kV electron accelerating voltage and collection semi-angle of 20.0 mrad with

dispersion rate of 0.2 eV/channel. Samples were placed in a single tilt holder and the aperture size on the spectrometer used for data acquisition was 2 mm in diameter. The acquisition time was optimized to obtain minimum noise and not to provoke beam damage.

EDS measures the number and energy of the X-rays produced by the ionization of the elements in the sample and these X-rays are characteristic of the element and the type of electron transition. EDS has limitations for determining light elements ($Z < 4$), but there is some degree of overlap with respect to atoms such as Na, Mg, P, S, Cl, K and Ca ($4 < Z < 11$), which can also be detected with EELS. This investigation used an EDS system (EDAX Genesis-4000) coupled with the TEM Philips CM200.

3. Results

Ultrastructure

Samples fixed with glutaraldehyde and postfixed with osmium offered enough contrast to distinguish the vesicle layer under bright field imaging mode (no post stain was used) (Fig. 2a, b), although High-Angle Annular Dark Field (HAADF) - STEM mode offered the best quality (Fig. 3a, b, e). Samples without osmium postfixation did not show enough contrast to detect the vesicles.

The vesicle monolayer contains mostly round vesicles, with an average size ~200 nm (from 50 to 400 nm) (Fig. 2c). A double membrane (10-15 nm) was easily distinguishable (Fig. 2d). Electrodense material seems to fill the interior of the vesicles, attached to the inner membrane (Fig. 2c; Fig. 3b, e).

The SM (~100 nm width) appears like a progressively ordered structure. It has a dense homogeneous structure at the mantle side that organizes progressively into a fibrous arrangement at the nacre side. Towards the interior, the most incipient crystals of the towers appear, and the ILMs seem to detach from the SM (Fig. 3b).

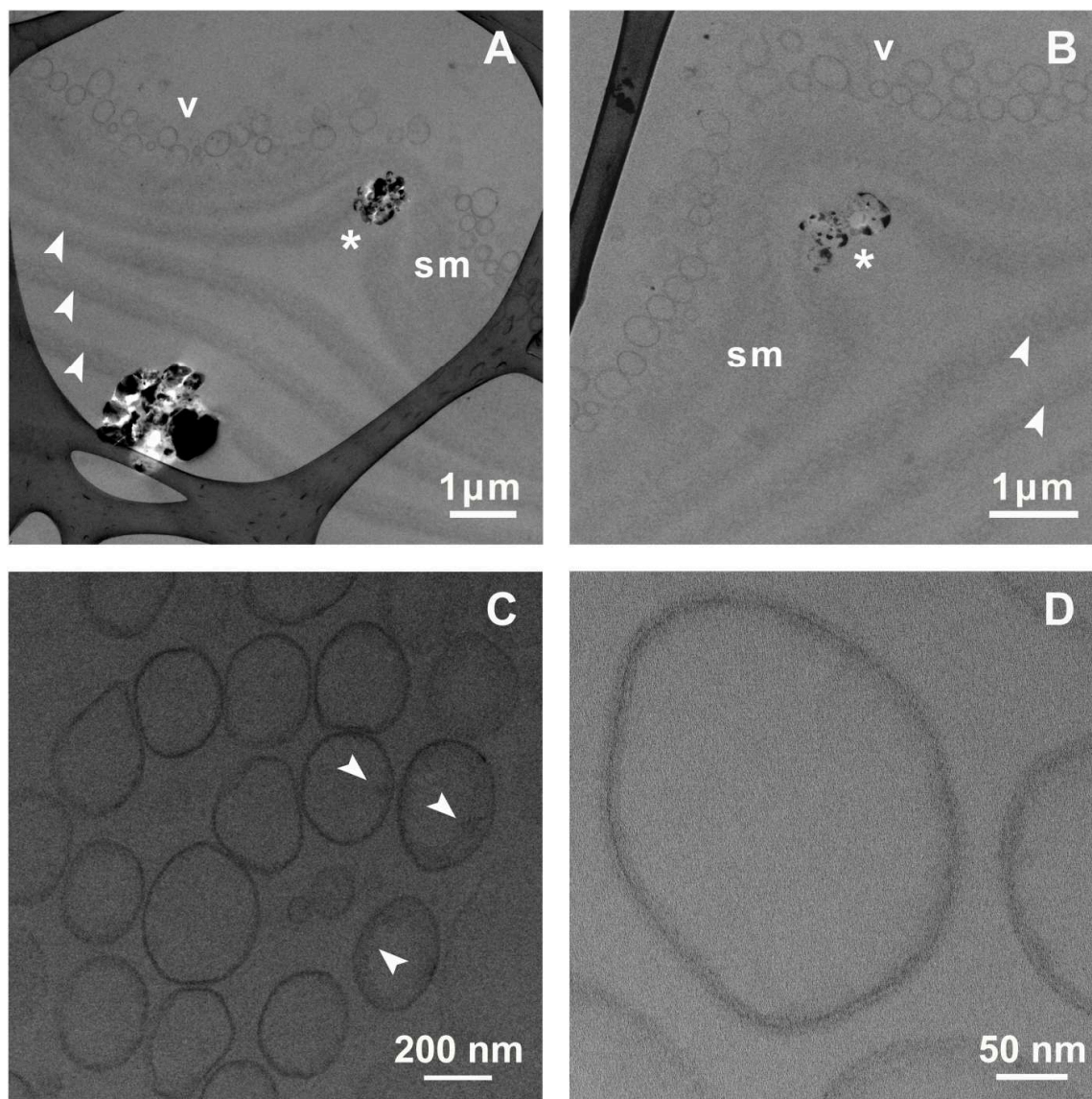


Fig. 2. Bright field TEM images of the vesicle layer. A) and B) vesicle layer (v) covering the surface membrane (sm). The tips of the first towers (marked with asterisks) are partly immersed within the SM (sm), and the interlamellar membranes (arrowheads) detach from it. C) Details of the vesicles showing the material attached to the inner membrane (arrowheads) and D) the double membrane. Samples fixed with glutaraldehyde 2.5% and postfixed with 1% osmium tetroxide.

Elemental analysis

The samples prepared by quick-freeze and freeze-drying preserved the cell structures relatively well. It was possible to localize the areas of interest (SM and vesicle layer), although some movements of the sub-cellular components might have occurred. The maintenance of the ion content was expected to be relatively good, since the sample was in contact with aqueous media only during the dehydration process, after the osmium postfixation. Microanalysis was carried out on the thinnest sections, selected on the basis of their grey hue (~ 50 nm thickness).

Systematic EELS measurements were performed on quick-frozen and freeze-dried samples, with and without OsO_4 as post-fixative. Signal intensity was higher in samples where osmium tetroxide was used. EDS analysis corroborated the data obtained by EELS. The structures studied in the outer side of the mineralization compartment were: the interior and the membrane of the vesicles (v and mv respectively), the SM (sm) and the light areas (la) in the Epoxy resin. In the inner side of the mineralization compartment, the ILMs (ilm), the electrodense material (em) spread between the ILMs and the light areas (la) in the Epoxy resin were analysed. Similar spectra were recorded at

each type of the structure investigated, so we present here (Fig. 3h; Fig. 4b) a representative single raw spectrum of each one. No smoothness was applied.

At the outer side of the mineralization compartment, EELS measurements revealed strong carbon K edges at 285 eV, indicating poorly ordered carbon, owing to the Epoxy resin used. The nitrogen K edge at 400 eV and oxygen K edge at 532 eV were evident in all the measurements. A strong Ca $L_{2,3}$ edge (~ 348 eV) was detected in the SM (sm) and in the interior of the vesicles (v). The membrane of the vesicles reported a minor intensity of the Ca $L_{2,3}$ edge and undetectable calcium signal was obtained from the light outer areas (la) (Fig. 3g, h).

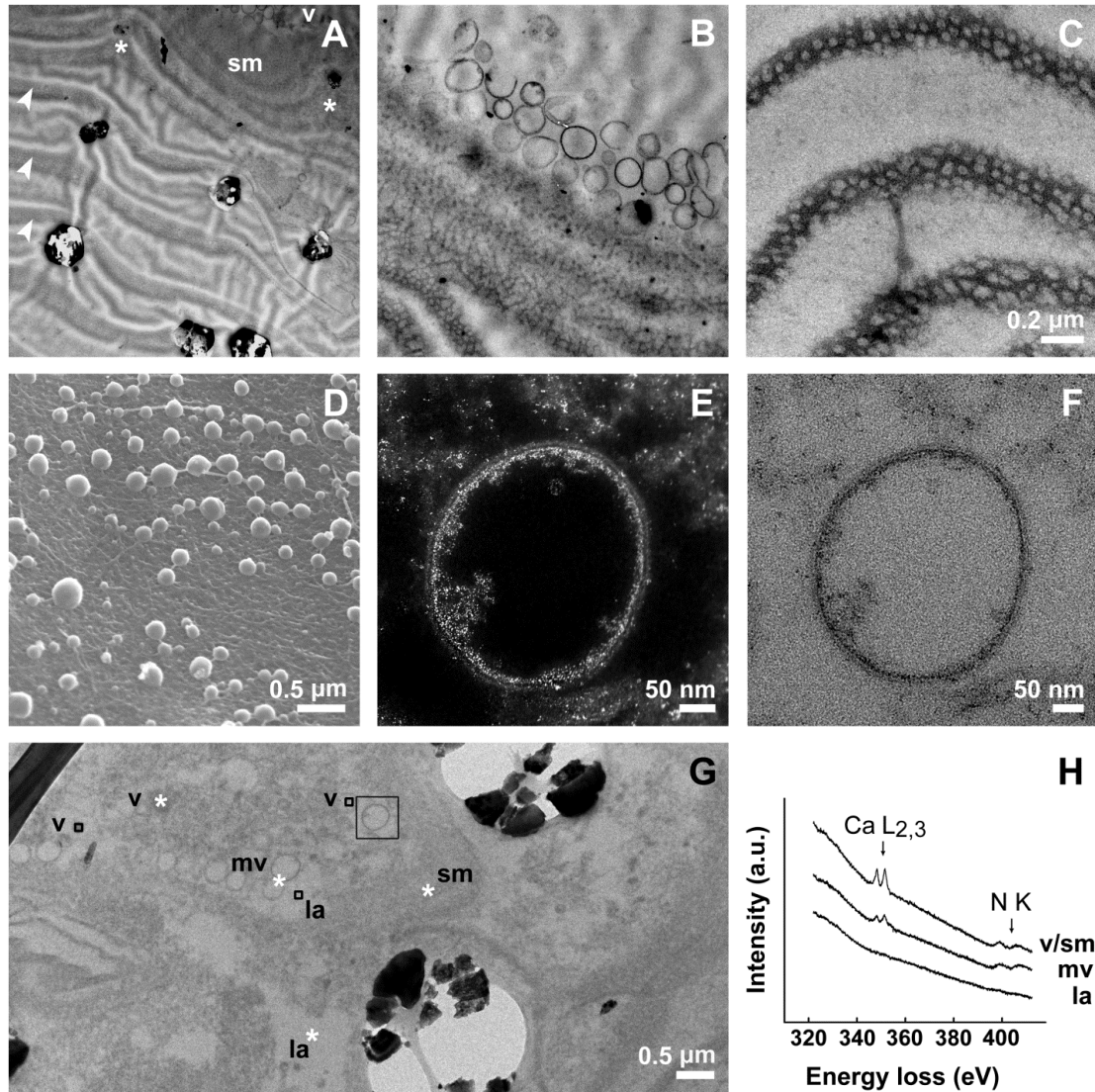


Fig. 3. Surface membrane and vesicle layer of *Phorcus turbinatus*. A) General view in STEM mode including the vesicles (v), the surface membrane (sm), the first towers immersed in the surface membrane (asterisks) and the interlamellar membranes (arrowheads). B) HAADF image of the vesicle layer, the surface membrane and the interlamellar membranes detaching from it. C) Bright field imaging mode of mature interlamellar membranes with the porous aspect typical of gastropods. Section post-stained with lead citrate and uranyl acetate. D) Scanning electron microscopy image of the vesicles covering the exterior of the surface membrane. E) HAADF image of a vesicle showing the material attached to its inner membrane. F) Same vesicle as in E) but in bright field mode. G) Bright field image of the vesicle layer and the surface membrane in an area close to the nacre towers, showing the vesicles (v), the membrane of the vesicles (mv), the surface membrane (sm) and the light areas (la) of the Epoxy resin. One spectrum was recorded in each point labelled. The vesicle shown in E) and F) is marked with a square. H) Core-loss spectra from the areas marked with an asterisk in G), showing Ca $L_{2,3}$ and N K edges. Single raw spectra, no smoothness was applied. Intensity is expressed in arbitrary units (a.u.) for comparison. A) and B) samples fixed with glutaraldehyde 2.5% and postfixated with 1% osmium tetroxide. C), E), F), G) samples quick-frozen and freeze-dried. D) Critical point dried sample.

At the inner side of the mineralization compartment, EELS spectra from the ILMs (ilm) revealed the K edges of carbon (285 eV), nitrogen (400 eV) and oxygen (532 eV), as well as $L_{2,3}$ edge of calcium (348 eV). The spectra obtained from the electrodense material (em) spread in the spaces between the ILMs showed the same peaks, though less intense. In the lighter areas (la) between ILMs, we observed the K edges of carbon, nitrogen and oxygen that correspond to the embedding resin, and a negligible signal of Ca $L_{2,3}$ edge.

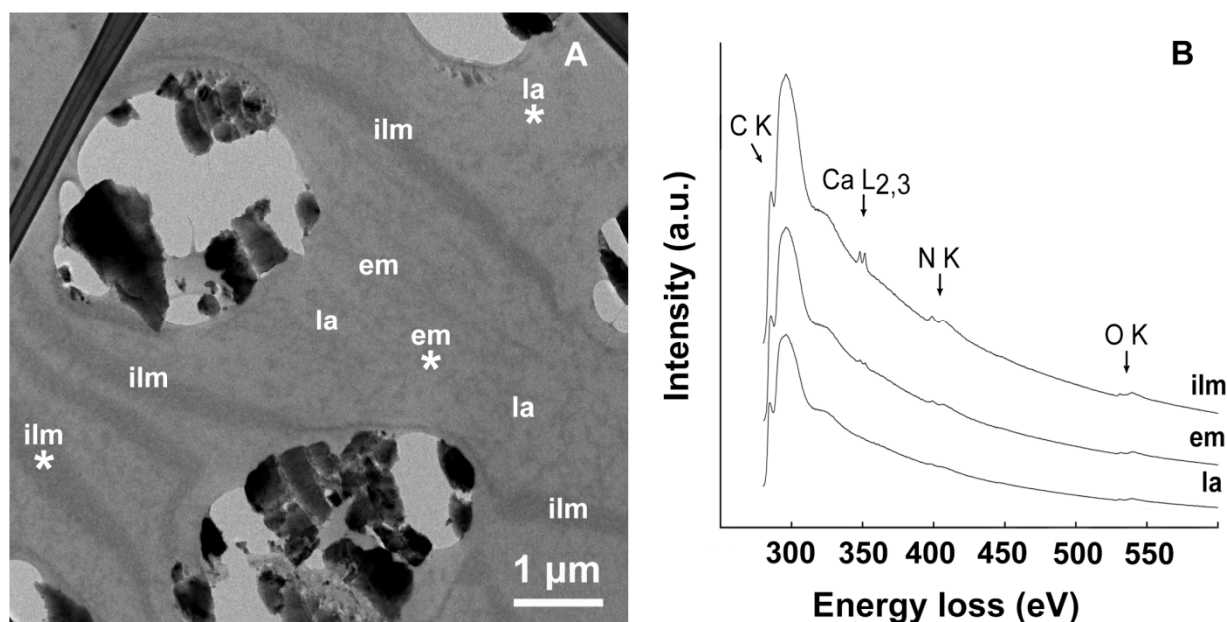


Fig. 4. A) TEM image of the mineralization compartment of a resin embedded section. It is possible to discern the towers of platelets (in diagonal section), the interlamellar membranes (ilm), the electrodense material (em) in between and the light areas (la). One spectrum was recorded in each point labelled. B) Core loss spectra recorded at 200 keV from the areas marked with an asterisk in A (average pixel area 105 nm²), showing C K, Ca $L_{2,3}$, N K and O K edges. Single raw spectra, no smoothness was applied. Intensity is expressed in arbitrary units (a.u.) for comparison. Quick-frozen and freeze-dried sample, postfixed in osmium tetroxide and embedded in EMBED 812.

4. Discussion

Images presented here clearly show double-layered vesicles (Fig. 2d), probably constituted of phospholipids, containing electrodense material. Some of them were filled completely, although others seemed to be partially empty, with the material mostly attached to the inner membrane (Fig. 2c; Fig. 3e, f). The dense amorphous material surrounding the vesicles and covering the SM (Fig. 3b, e) might have been extruded from the vesicles in areas adjacent to the SM.

In cross section, the material that makes up the SM seems to undergo maturation and becomes increasingly better defined and organized into layers with depth (Fig. 3b). At the mantle side, it has a homogeneous soft aspect and, beyond this, fibrillar structures separated by irregular holes become perceivable. The typical porous aspect of gastropod ILMs (Fig. 3c) is fully achieved on the nacre side and in some parts it was possible to see an ILM detaching from the SM.

Elemental analysis revealed the presence of calcium in different areas of the system: the dense material inside and surrounding the vesicles, the SM, the ILMs and the electrodense matrix scattered between the ILMs. Two facts suggest that calcium is in a bound form: 1) no calcium was detected in the chemically fixed samples, since chemical fixation and standard preparation protocols involve several aqueous steps in which ions and small molecules could be mobilized. 2) The

observation that a strong calcium signal was repeatedly detected in the electrodense material, in contrast to an undetectable signal in the lighter areas of the sample. Calcium has a small Z number, so it does not give high contrast in bright field imaging mode. The electrodense material with which it seems to be associated is stained with osmium tetroxide that preferentially binds to double bonds of lipids and some proteins.

It is likely that calcium forms part of the structures (SM, ILMs) bound to the organic matrix. It is well established that ILMs are composed mainly of proteins and polysaccharides [18]. SM composition is not known as yet, but it is easy to speculate that it should be similar to that of the ILMs, since these detach from the SM. Similarly, calcium seems to be in a bound form inside the vesicles. The fact that a significantly stronger calcium signal was retrieved from post fixed samples, suggests that fixation with glutaraldehyde followed by OsO₄ could avoid the loss of part of the material.

We have to keep in mind that forming nacre tablets begin to grow within the SM [12]. They first acquire their full height and subsequently expand laterally; in this way, the tip of the tower is always embedded within the SM [12]. Previous work has highlighted that the nuclei of gastropods tablets are enriched with organic material [11,15]. Accordingly, the organic material that composes the central core of the plates should be absorbed from the SM. In other groups, (*Atrina*, Bivalvia; *Nautilus*, Cephalopoda), the core mainly consists of acidic proteins [19] which seem to be distributed concentrically around the nucleus [20].

Recent findings re-emphasize the important role of negatively charged groups in sequestering free calcium ions and promoting nucleation events [21]. Our findings concerning the concentration of the calcium associated with an organic matrix (SM, ILMs) concur with those of Smeets *et al.* [21]. ILMs are mainly composed of acidic glycoproteins enriched in aspartic and glutamic acid [22], which are negatively charged at cellular pH (pH 7) [23]. The calcium atoms of the SM and ILMs might be bound to the negative groups of the matrix. Future efforts should be directed towards determining the nature of the content of the vesicles and the mechanisms by which calcium binds to these molecules.

Acknowledges

We acknowledge Achim Klein-Hoffmann (Fritz-Haber-Institute) for guidance in sample preparation and Xing Huang (Fritz-Haber-Institute) for his advice in analytical techniques. E.M.-S. received funding from project P10-RNM6433 of the Andalusian Consejería de Innovación Ciencia y Tecnología, as well as from the European COST Action TD0903 (STSM-TD0903-010513-032973 and STSM-TD0903-090114-039009). Comments from two anonymous reviewers helped to improve the manuscript.

References

- [1] S. Weiner, W. Traub, X-ray diffraction study of the insoluble organic matrix of mollusk shells, FEBS Lett. 111 (1980) 311-316.
- [2] S. Weiner, L. Addadi, Acidic macromolecules of mineralized tissues - the controllers of crystal-formation, Trends Biochem. Sci. 16 (1991) 252-256.
- [3] A.P. Jackson, J.F.V. Vincent, R.M. Turner, The mechanical design of nacre, Proc. R. Soc. London Ser B 234 (1984) 415-440.
- [4] G. Bevelander, H. Nakahara, An electron microscope study of the formation of the nacreous layer in the shell of certain bivalve molluscs, Calcif. Tissue Res. 3 (1969) 84-92.

-
- [5] G. Bevelander, H. Nakahara, Compartment and envelope formation in the process of biological mineralization, in: M. Omori, N. Watabe (Eds.), *Mechanism of Biomineralization in Animals and Plants*, Tokai University Press, Tokyo, 1980, pp. 19-27.
- [6] H. Nakahara, Nacre formation in bivalve and gastropod molluscs, in: S. Suga and H. Nakahara (Eds.), *Mechanisms and Phylogeny of Mineralization in Biological Systems*, Springer, Berlin, 1991, pp. 343-350.
- [7] S. Wise Jr., W. Hay, Scanning electron microscopy of molluscan shell ultrastructures II. Observations of growth surfaces, *Trans. Am. Microsc. Soc.* 86 (1968) 419-430.
- [8] H.K. Erben, Über die Bildung und das Wachstum von Perlmutter, *Biomineralization* 4 (1972) 15-46.
- [9] H.K. Erben, On the structure and growth of the nacreous tablets in gastropods, *Biomineralization* 7 (1974) 14-27.
- [10] H. Nakahara, An electron microscope study of the growing surface of nacre in two gastropod species, *Turbo cornutus* and *Tegula pfeifferi*, *Venus* 3 (1979) 205-211.
- [11] H. Nakahara, Calcification of gastropod nacre, in: P. Westbroek, E.W. De Jong (Eds.), *Biomineralization and Biological Metal Accumulation*, Reidel Publishing Company, Dordrecht, 1983, pp. 225-230.
- [12] A.G. Checa, J.H.E. Cartwright, M.G. Willinger, The key role of the surface membrane in why gastropod nacre grows in towers, *Proc. Nat. Acad. Sci. USA* 106 (2009) 38-43.
- [13] J.H.E. Cartwright, A.G. Checa, The dynamics of nacre self-assembly, *J. R. Soc. Interface* 4 (2007) 491-504.
- [14] S. Wise Jr., Microarchitecture and deposition of gastropod nacre, *Science* 167 (1970) 1486-1488.
- [15] H. Mutvei, Ultrastructural characteristics of the nacre in some gastropods, *Zoologica Scripta* 7 (1978) 287-296.
- [16] M.A. Hayat, *Basic Techniques for Transmission Electron Microscopy*, first ed., Academic Press, Orlando, 1986.
- [17] R.F. Egerton, *Electron Energy-Loss Spectroscopy in the Electron Microscope*, third edition, Springer, US, 2011.
- [18] G. Goffinet, Ch. Jeuniaux, Composition de la conchioline du nacre de Nautilus, *Comp. Biochem Physiol* 29 (1969) 277-282.
- [19] M.A. Crenshaw, H. Ristedt, Histochemical and structural study of nautiloid septal nacre, *Biomineralization* 8 (1975) 1-8.
- [20] F. Nudelman, B.A. Gotliv, L. Addadi, S. Weiner, Mollusk shell formation: mapping the distribution of organic matrix components underlying a single aragonitic tablet in nacre, *J. Struct. Biol.* 153 (2006) 176-187.

[21] P.J.M. Smeets, K.R. Cho, R.G.E. Kempen, N.A.J.M. Sommerdijk, J.J. De Yoreo, Calcium carbonate nucleation driven by ion binding in a biomimetic matrix revealed by in situ electron microscopy, *Nature Materials* (2015) Advance online publication, doi: 10.1038/nmat4193

[22] S. Weiner, Aspartic acid-rich proteins: major components of the soluble organic matrix of mollusk shells, *Calcif. Tissue Int.* 29 (1979) 163-167.

[23] D.L. Nelson, M.M. Cox, *Lehninger Principles of Biochemistry*, fourth ed., W.H. Freeman and Company, New York, 2005.